Osaka University Knowledge Archive

Title	Axial charge of the weak nucleon current extracted from the β decays of spin aligned 12B and 12N
Author(s)	Yamaguchi, Takayuki
Citation	大阪大学, 1998, 博士論文
Version Type	VoR
URL	https://doi.org/10.11501/3143747
rights	
Note	

Osaka University Knowledge Archive : OUKA

https://ir.library.osaka-u.ac.jp/

Osaka University

Axial charge of the weak nucleon current extracted from the β decays of spin aligned ^{12}B and ^{12}N

Takayuki YAMAGUCHI

Department of Physics, Graduate School of Science, Osaka University

Abstract

The axial charge matrix element has been precisely determined for the β-decay of the A = 12 isotriplet through the alignment correlation terms in the β ray angular distributions from ^{12}B and ^{12}N in order to examine the mesonic enhancement in the axial charge. The axial charge matrix element in the nuclear β decay has been paid much attention for the study of the mesonic degrees of freedom in the nucleus, since Kubodera, Delorme and Rho predicted that the one pion exchange current enhances the axial charge by as much as 40 % compared with that of the impulse calculation. Actually, in the previous measurements of the alignment correlation terms for ^{12}B and ^{12}N, the mesonic enhancement has been found to be as much as 40 ~ 60 % over the impulse approximation. In heavy nuclei of lead region, however, anomalously large enhancements, which reach as much as 80 %, have been found through the measurements of the first-forbidden transition rates. Such a strong mass dependence of the mesonic enhancement factor may be an evidence of the in-medium renormalization effect of the hadronic masses, according to the chiral perturbation theory. For the complete understanding of the meson exchange current, the mechanism of the mass dependence has to be made clear. The present experiment aims to establish the standing point of the mesonic enhancement, namely, the precise enhancement factor in the light mass region.

For the precise alignment correlation terms, several experimental improvements have been made. The alignments necessary for the measurements are artificially created by converting the polarizations produced through the nuclear reaction by use of the NMR technique, so called spin manipulation technique. For the present study, hyperfine interactions of ^{12}B and ^{12}N implanted in Mg (hcp) crystal which is

the key knowledge for the precise spin manipulation technique have been studied in detail. As a result, for ^{12}B and ^{12}N in Mg, the minor implantation sites have been found in addition to the main site. This second site was found to arise from the micro grains whose c-axis, hence, the electric field gradient is perpendicular to the original c-axis of the bulk crystal. Based on this knowledge, the spin manipulation technique has been improved to be completely free from the effect from the minority site. We accumulated much more counting statistics. Comparing with the previous data, the reliability of the axial charge matrix element has been established. The upper limit of possible systematic uncertainties such as counter responses, alignment derivation, and possible spurious counting asymmetry between the positive and negative alignment cycles has also been carefully reanalyzed in deriving the alignment correlation terms.

As a result, the ratio y of the axial charge to the Gamow-Teller matrix element has been determined to be $y = 4.69 \pm 0.05$ (stat.) ± 0.22 (syst.), which shows 57 % enhancement compared with the impulse value including the core polarization effect that is reliably given theoretically in the $A = 12$ case. The soft-pion exchange contribution in the meson exchange currents is precisely predicted to be 41 %, while that of heavy mesons is found to be negligible. The extra enhancement 16 % in the axial charge is a strong indication of unknown mechanism. It may be explained by the in-medium renormalization effect for the decaying nucleon in the finite nuclear density. In this approach, the mass renormalization is extracted to be 8 ± 4 % in the $A = 12$ system, which is fairly consistent with the mass renormalization effect extracted from the magnetic moments of the doubly closed shell ± 1 nucleon nuclei.

Acknowledgments

The author wishes to extend his thanks to all of those who have helped to make this work successful:

Professor T. Minamisono for his proposing the present experiment, providing earnest guidance during the work, and discussing the thesis.

Associate Professor K. Matsuta for his constant collaboration, discussions, and encouragement.

Research Associate M. Fukuda for his collaboration, discussions, and encouragement.

Research Associate M. Mihara for his discussions, and encouragement.

Professor M. Morita for his studies concerning the theoretical aspects and fruitful discussions.

Associate Professor K. Koshigiri for his studies concerning theoretical aspects, analysis for this experiment, and fruitful discussions.

Professsor Y. Nagashima for his encouragement and reading this thesis.

Professor H. Ohtsubo for his encouragement and reading this thesis.

Professor T. Kishimoto for his encouragement and reading this thesis.

Mr. M. Sakamoto for his technical supports during this experiment and for developing the experimental apparatus.

Mr. T. Sakurai for his technical supports during this experiment.

Mr. K. Onishi for his technical supports for the environment of the computers.

Mr. Higa for his technical supports for the electronics.

Mr. T. Onishi, T. Miyake and M. Sasaki for their discussions and encouragement.

Mr. K. Minamisono, T. Ikeda, Y. Muramoto, T. Sumikama and all students for their

constant collaboration.

The present study was partially supported by Research Fellowships of the Japan Society for the Promotion of Science for Young Scientists.

Contents

	Page
Abstract	ii
Acknowledgments	iv
List of Tables	x
List of Figures	xii
1 Introduction	**1**
1.1 Non-nucleonic degrees of freedom in the nucleus	1
1.2 Axial charge and the β-ray angular distributions of the $A = 12$ system	5
1.3 Axial charge extracted from the first-forbidden transitions	10
1.4 Historical view and the present experiment	15
2 Theoretical background of the nuclear β decay	**20**
2.1 Interaction Hamiltonian	20
2.2 β-ray angular distribution from the oriented nucleus	24
2.3 Meson exchange current in the axial charge	30
2.4 Strong CVC hypothesis	35
2.5 Second class current	41
3 Experimental method and apparatus	**45**
3.1 Overview	45
3.1.1 Principle of the experiment	45
3.1.2 Survey of the experimental method	48
3.1.3 Comment on the experimental technique	50
3.2 Production of the spin polarized ^{12}B and ^{12}N	51
3.2.1 Rotating target system	51

3.2.2 Production of ^{12}B and ^{12}N 56
3.3 Recoil implantation 62
3.3.1 Maintaining the polarization 62
3.3.2 Hyperfine interaction of ^{12}B and ^{12}N in a Mg crystal 63
3.3.3 Reaction chamber and magnet 71
3.3.4 Implantation medium - Recoil stopper - 73
3.4 Spin manipulation technique 74
3.4.1 Principle of spin manipulation 74
3.4.2 Improvements on the present spin manipulation 78
3.4.3 Rf coil and amplifiers 81
3.4.4 Achievement of the spin manipulation 88
3.5 Detection of β rays 90
3.5.1 β ray detector 90
3.5.2 Electronics 93
3.5.2.1 Trigger signals 93
3.5.2.2 Linear signals 93
3.5.3 β-ray energy spectra 98
3.6 Experimental procedure and data acquisition 100
3.6.1 Experimental control and procedure 100
3.6.2 Timing program of the data taking 103
3.6.2.1 Timing program of the Main run 103
3.6.2.2 Timing program of the Test run 104
4 Data analysis 106
4.1 Energy calibration 106
4.1.1 β-ray counter response and spectrum 106

4.1.2 Energy calibration 110
4.2 Determination of polarization and alignment 113
4.2.1 Determination of polarization 113
4.2.2 Determination of alignment 115
4.3 Alignment correlation term 120
4.4 Corrections and errors 123
4.4.1 Solid-angle correction 125
4.4.2 Decay-branch correction 127
4.4.3 Correction for counter response 130
4.4.4 Correction for polarization-correlation term 132
4.4.5 Background correction 133
4.4.6 Others 135
5 Results and discussions 137
5.1 Results 137
5.2 Giant mesonic effect in the axial charge and its implications 147
5.3 Influences of the present results to other symmetry problems 154
5.3.1 Induced tensor term in the axial-vector current 154
5.3.2 Weak magnetism term 158
5.4 Results on other nuclei and future directions 163
6 Conclusion 171
7 Appendixes i
7.1 Preparation of the reaction target i
7.2 Preparation of the stopper iii
7.3 β-NMR method vii
7.3.1 Depolarization vii

7.3.2 Adiabatic Fast Passage viii

7.4 β-NQR method xii

7.5 Calibration of rf fields xv

7.6 Uncertainty from beam fluctuation xvi

7.7 Experimental details of ^{8}Li and ^{20}F xxi

7.7.1 Experimental conditions xxi

7.7.2 Spin manipulation for $I = 2$ nuclei xxii

8 References xxiv

List of Tables

Page

1.1 KDR prediction. 6

1.2 Decay properties of the $A = 12$ system. 8

1.3 Summary of the angular distribution experiments in the $A = 12$ system. 16

2.1 Summary of the spectral shape factor in the β-ray energy spectrum of the $A =$ 12 mirro nuclei. 37

2.2 G-parity of the vector and axial vector current. 42

3.1 Experimental conditions. 57

3.2 Experimental conditions for the spin manipulation. 76

3.3 List of modules used in the rf circuit. 83

3.4 Rf conditions for making spin alignment. 83

3.5 Spin alignments obtained by the spin manipulation. 88

3.6 The modules and parameters used for the detection circuit. 95

4.1 Productions of the calibration β-sources. 110

4.2 The energy independent corrections and errors. 124

4.3 Branching ratio correction. 129

4.4 Response function correction. 131

4.5 Background correction. 134

4.6 The correction factor and errors. 136

5.1 Alignment correlation terms of $A = 12$ system in the present study. 139

5.2 The simple analyses of the alignment correlation terms. 140

5.3 Alignment correlation terms of $A = 12$ system measured at 1985. 142

5.4 Alignment correlation terms of $A = 12$ system measured at 1992. 144

5.5 Full analyses of the alignment correlation terms. 146

5.6 Axial charge matrix elements obtained by the simple analysis. 150

5.7 Extra enhancement in the axial charge obtained by the full analysis. 150

5.8 The enhancement in the axial charge due to the heavy mesons. 150

5.9 Summary of the experiments of the weak magnetism term. 161

7.1 Experimental conditions for ^{8}Li and ^{20}F. xix

List of Figures

Page

1.1 Schematic nucleon-nucleon potential based on meson exchanges. 4

1.2 Decay scheme of the $A = 12$ triplet. 9

1.3 Summary of the enhancements in the axial charge matrix elements obtained from the first-forbidden transitions. 14

2.1 Diagram of the one-body and two-body currents which interact with the weak current. 34

2.2 Comparison of the γ-decay and the weak vector deacy. 40

2.3 Summary of the induced tensor term in the axial-vector current. 44

3.1 Principle for the measurement of the alignment correlation terms. 47

3.2 Schematic view of the experimental setup. 49

3.3 Schematic view of the beamline. 53

3.4 Schematic view of the reaction chamber. 54

3.5 Schematic view of the rotation pickup system. 55

3.6 Kinematics of the recoiled nuclei. 58

3.7 Schematic view of details around the stopper region in the reaction chamber. 59

3.8 β-ray time spectra for the ^{12}B and ^{12}N. 60

3.9 Direction of the polarization produced through the nuclear reaction. 61

3.10 Crystal structure of Mg (hcp). 66

3.11 Energy levels and frequency split caused by the mafnetic and the quadrupole interaction in the stopper. 67

3.12(a) Typical β-NMR spectra of ^{12}B and ^{12}N in Mg. 68

3.12(b) Typical β-NQR spectra of ^{12}B in Mg. 69

3.12(c) Typical β-NQR spectra of ^{12}N in Mg. 70

3.13 Schematic view of the vicinity of the recoil stopper. 72

3.14 Spin manipulation for the creation of spin alignment from spin polarization. 77

3.15 Spin manipulation for the second site. 80

3.16 Schematic view of the stopper and rf coil. 84

3.17 Circuit diagram of the rf control. 85

3.18 Timing sequence and rf signals in the rf control circuit. 86

3.19 LC resonator for rf system. 87

3.20 Polarization-change by the spin manipulation. 89

3.21 β-ray counter telescope. 92

3.22 Circuit diagram for the data taking system. 96

3.23 Stability of the β-ray counter system. 97

3.24 Typical β-ray energy spectra for ^{12}B and ^{12}N. 99

3.25 Diagram of the experimental control. 101

3.26 Schematic diagram and timings for the experimental control signals. 102

3.27 Timing sequence for the present experiment. 105

4.1 Response function of the β-ray counter telescope for the monochromatic β ray. 109

4.2 Typical β-ray energy spectra of ^{12}B, ^{12}N, and calibration sources. 111

4.3 Energy calibration of the β-ray counter telescopes. 112

4.4(a) Result of the spin manipulation of ^{12}B. 118

4.4(b) Result of the spin manipulation of ^{12}N. 119

4.5 Alignment correlation terms as a function of β-ray energy. 122

5.1 Alignment correlation terms (data at 1985). 141

5.2 Alignment correlation terms (data at 1992). 143

5.3 Alignment correlation terms (all data). 145

5.4 Axial charge y in the $A = 12$ system. 151

5.5 Results on the induced tensor term. 157

5.6 Results on the weak magnetism term. 162

5.7 Decay scheme of the $A = 8$ system. 165

5.8 Decay scheme of the $A = 20$ system. 166

5.9 Decay scheme of the $A = 41$ system. 167

5.10 Decay scheme of the $A = 13$ system. 168

5.11 Alignment correlation term of ^{8}Li. 169

5.12 Alignment correlation term of ^{20}F. 170

7.1 Schematic view of target evaporation. ii

7.2 Shape of the stopper. iv

7.3 Schematic view of cutting of Mg crystal by the spark slicer. v

7.4 X-ray diffraction pattern of Mg crystal. vi

7.5 Schematic view of the spin precession under the magnetic field. x

7.6 Adiabatic fast passage technique. xi

7.7 β-NQR method (depolarization). xiii

7.8 β-NQR method (AFP). xiv

7.9 Alignments in the polarization and alignment section. xx

7.10 Spin manipulation in the case of $I = 2$. xxiii

Chapter 1

Introduction

1.1 Non-nucleonic degrees of freedom in the nucleus

The nuclear shell model has greatly succeeded in the describing the nuclear properties for overall nuclei, summing up the properties of individual nucleons bound in the effective potential. This is called the impulse approximation. For example, the magnetic moments probe the motions of the nucleons in the nucleus, and the quadrupole moments probe the nucleon density distributions.

However, the nucleons in the nucleus strongly interact with each other through the exchange of various mesons, and various isobaric states such as Δ particles are virtually excited in the nucleus. Although these non-nucleonic aspects of the nucleus are difficult to detect, because the main part of their contributions can be replaced by the effective interaction between nucleons, they should be taken into account for deeper understanding of the nuclear structure beyond the nucleon-only-picture. Actually, EMC experiment, for example, disclosed the differences of the quark distribution in the nucleon for various nuclei from that for the free nucleon [AR94]. These non-nucleonic degrees of freedom in the nucleus are challenging problems in nuclear physics, which have to be made clear both experimentally and theoretically for our better understanding of the nuclear phenomena.

Among these non-nucleonic aspects, the exchange of mesons has very important

roles. In particular, π meson has a special role in the nucleus, i.e., the pion is a source of the nuclear force which makes nucleons bind to form the nucleus, as in the Yukawa's meson theory since 1935. Nowadays, the nucleon-nucleon potential is understood based on the exchange of mesons of various types; the lightest pion gives a long-range attractive force, so do scaler mesons in the middle, and vector mesons give a short-range repulsive one, as shown in Figure 1.1, although, ultimately, the meson-based nuclear force should be described in terms of the force between quarks and gluons. Despite this important role, the direct evidence of the meson exchange is very difficult to find in nuclear phenomena.

Historically, the mesonic effect in the nucleus had been found in the thermal neutron capture by protons. The cross section of this reaction was 10 % smaller than the impulse calculation in which the wave functions of the two-body system are reliably given. The residual 10 % was accounted for by the meson exchange effect [RI72]. This effect was also found in the photo- and electro-disintegration of deuteron [HO73], and the magnetic moments of ^{3}H and ^{3}He [CH71]. These observables all could not be well reproduced by the impulse calculations only, and the deviations between experimental results and the impulse calculations were not accounted for until the meson exchange currents were introduced.

Among various mesons, pions have the dominant contribution to low energy nuclear properties, according to the soft-pion theorem which is a consequence of general consideration of the chiral symmetry. This is basically the symmetry between the left handed world and the right handed world. The nucleon as a many-body system is symmetric under the chiral transformation. The ground state of a nucleus is highly degenerate under the chiral transformation. This leads to the fact that a nucleus should contain a number of virtual massless pions as Goldstone Bosons which appear as a consequence of the spontaneous symmetry breaking of

chiral symmetry. Thus, pions in the nucleus are considered not only as one of mesons as a source of the nuclear force, but also as the Goldstone mode from the spontaneous symmetry breaking of chiral symmetry. Various models of the pion structure such as chiral bag model and MIT bag model are proposed so as to incorporate with the chiral symmetry which leads to the argument of the origin of the quark masses.

In the recent studies, the photo- and electro-disintegration of deuteron in the high momentum transfer region have been satisfactorily understood through the pion exchange only. The short-range correlation of heavy mesons looks less important. This can be understood in terms of the chiral filter mechanism described above [RH81]. It also states that the chirality filters out the heavy mesons and the pions survive in the nucleus.

Thus, meson exchange effect, in particular pion response in the nucleus is very important for the knowledge of the non-nucleonic degrees of freedom in the nucleus, i.e. for deeper understanding of nuclear structure, as well as for chiral-symmetry argument which is a key issue for both the nuclear force and the dynamics of quarks and gluons. In the present experiment, we study the meson exchange effect in the axial charge extracted from the nuclear β decay.

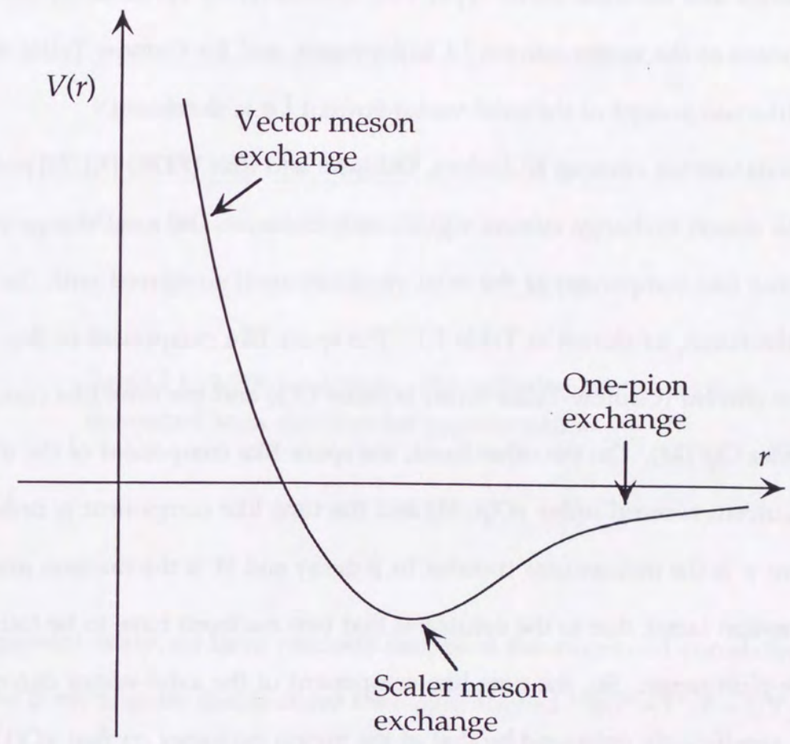

Figure 1.1 Schematic nucleon-nucleon potential based on meson exchanges. In the short-range vector mesons give the repulsive force, and in the middle scaler mesons give the attractive one. In the long-range pions give the attractive force which mainly contributes to the low energy phenomena.

1.2 Axial charge and the β-ray angular distributions of the $A = 12$ system

In the present study, the meson exchange effect has been studied through the nuclear β decay. The nuclear β decay is described in terms of the current-current interaction with the vector and the axial-vector type, V-A. Ordinary, for Fermi decay the time like component of the vector current $\int 1$ is dominant, and for Gamow-Teller decay the space like component of the axial-vector current $\int \sigma$ is dominant.

In the axial-vector current, Kubodera, Delorme and Rho (KDR) [KU78] pointed out that the meson exchange current significantly enhances the axial charge matrix element (time like component of the axial vector current) compared with the impulse calculation, as shown in Table 1.1. The space like component of the axial-vector current (Gamow-Teller term) is order $O(1)$ and the time like component is recoil order $O(p/M)$. On the other hand, the space like component of the meson exchange current is recoil order $\kappa O(p/M)$ and the time like component is order $\kappa O(1)$. Here, p is the momentum transfer in β decay and M is the nucleon mass, and κ is suppression factor due to the constraint that two nucleons have to be found within one-pion range. So, the time like component of the axial-vector current $O(p/M)$ is significantly enhanced by that of the meson exchange current $\kappa O(1)$. The magnitude of the enhancement in the axial charge was estimated to be approximately 40 % from the soft-pion theorem.

For most cases, however, it is difficult to separate out the axial charge from the main Gamow-Teller term. But two types of experiments are available to extract the axial charge. One is measurements of the angular distribution from spin-oriented β-emitting nuclei and angular correlations between β and the following γ- or α-ray radiation. The other is the measurement of the decay rate of the first-forbidden transition. These two types of experiments provide us with very unique chances to

study the mesonic degrees of freedom in the nucleus in low energy region.

		space like	time like
V_λ	IA	$O(p/M)$	$O(1)$
	EC	$\kappa O(1)$	$\kappa O(p/M)$
A_λ	IA	$O(1)$	$O(p/M)$
	EC	$\kappa O(p/M)$	$\kappa O(1)$

Table 1.1 KDR prediction. The soft-pion contribution is compared with the impulse approximation.

In the present study, we have precisely measured the alignment correlation terms in the β-ray angular distributions from spin aligned $^{12}B(I^\pi = 1^+, T = 1, T_Z = 1, T_{1/2} = 20$ ms) and $^{12}N(I^\pi = 1^+, T = 1, T_Z = -1, T_{1/2} = 11$ ms) implanted in Mg, by means of the modified spin manipulation technique in the β-NMR method, which artificially create the spin alignments necessary for the measurement. The decay schemes and properties are shown in Figure 1.2 and Table 1.2, respectively. The alignment correlation term in the β-ray angular distribution from aligned nucleus is one of the most reliable probes to extract the axial charge matrix element. The sum of the alignment correlation coefficients of mirror decays singles out the ratio y of the axial charge to the Gamow-Teller matrix element purely experimentally, namely completely free from the theoretical calculation of other matrix elements.

Generally, the axial charge is theoretically given by the sum of contributions from the impulse current, the meson exchange current and the core polarization effect, i.e.,

$$y = y_{IA} + y_{MEC} + y_{CP}. \tag{1.1}$$

Here, the contribution of the impulse current y_{IA} is dominant, and is less sensitive to the details of the nuclear models because it is the ratio relative to the Gamow-Teller term. The core polarization effect significantly affects the axial charge together with the meson exchange current, that has been studied by Koshigiri et al. in detail [KO81][KO89]. For the A = 12 system, the core polarization effect was determined so as to incorporate with the experimental result of the magnetic form factor in the electron inelastic scattering on ^{12}C [SA79]. So, the mesonic enhancement in the axial charge can be precisely compared with the theoretical calculation. Thus, the present experiment is the unique chance to discuss the mesonic degrees of freedom in the nucleus in detail.

Recently, a mass dependence of the mesonic enhancement has been found in the axial charges extracted from the analyses of the first-forbidden transitions. A review of the results of the first-forbidden transitions are described in the next section. Since the axial charge is mainly determined by the contribution from the decaying nucleon near the nuclear surface, the mesonic enhancement in the axial charge is expected to slightly depend on the mass number A reflecting the density which the decaying nucleon feels. In order to understand the mass dependence of the enhancement in the axial charges, it is necessary to determine axial charges systematically in wide mass region. The present experiment aims to establish the standing point of the mesonic enhancement, namely, the precise enhancement factor in the light mass

region. We focus on the mirror pair ^{12}B and ^{12}N in the mass A = 12 system in the light region, which will be a key point to derive a density dependence of the enhancements in the axial charges, since it will give us the knowledge for the nucleon at the almost thinnest density of about 0.04 nucleons/fm^3. In order to find such a density dependence of the enhancement in axial charges, measurements of the alignment correlation terms of other systems are now in progress. The measurements are ongoing for ^{8}Li and ^{8}B mirror pair in the A = 8 system, ^{20}F and ^{20}Na pair in A = 20, and ^{41}Sc in A = 41. The results on the preliminary experiments are briefly reported in the section 5.4.

		^{12}B	^{12}N
I^{π}		1^+	1^+
(T, T_Z)		(1, -1)	(1, +1)
$T_{1/2}$		20.41(6) ms	10.97(4) ms
Energy level (MeV)		Branching ratio	
Ground state		97.14 ± 0.30 %	94.55 ± 0.60 %
First excited state	4.439 MeV	1.28 ± 0.04 %	1.90 ± 0.03 %
Second excited state	7.654 MeV	1.5 ± 0.3 %	2.7 ± 0.4 %
Third excited state	10.3 MeV	0.08 ± 0.02 %	0.46 ± 0.15 %
Fourth excited state	12.710 MeV	-	0.29 ± 0.13 %

Table 1.2 Decay properties of the A = 12 system.

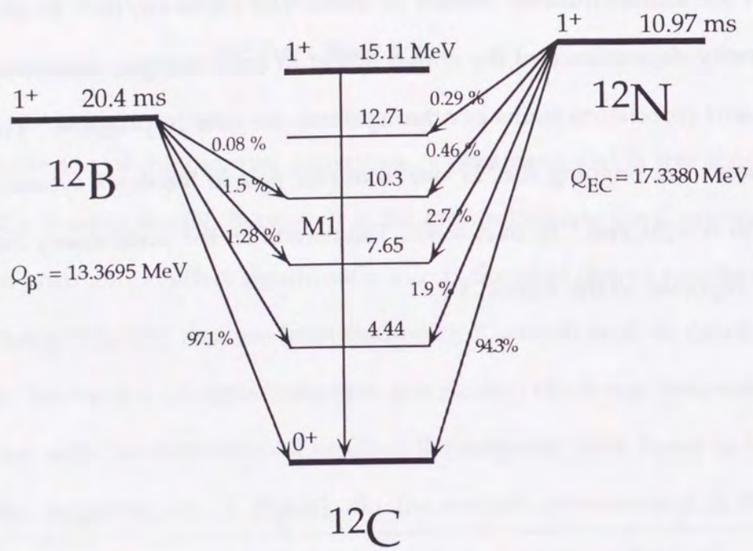

Figure 1.2 Decay scheme of the $A = 12$ triplet. ^{12}B(ground), ^{12}C(15.11 MeV), and ^{12}N(ground) form members of the isotriplet.

1.3 Axial charge extracted form the first-forbidden transitions

The axial charge matrix element is also extracted from the decay rate of the first-forbidden transition. On this subject, recently, Warburton et al. [WA91][WA94a] analyzed the first-forbidden β-decay rates of the nuclei in the lead region and showed that their axial charge matrix elements were systematically enhanced by 80 % compared with the impulse values. This enhancement in the axial charges is two times larger than that expected from the KDR prediction, and is not completely accounted for by any theoretical calculations. Even in the light nuclei, for instance, the β-decay rate of $^{16}N(0^-) \rightarrow {}^{16}O(0^+)$ transition showed 60 % enhancement in the axial charge [PA75][GA83][MI83][HA85][FU95][MI96a], which could not be completely explained by the introduction of the exchange currents, too. Although these studies of first-forbidden transitions rather depend on theoretical evaluations of other forbidden matrix elements to extract the axial charge matrix element, the enhancements in the axial charge matrix elements seem to be systematically larger than that expected for the soft-pion theorem. The similar results are seen in other systems, A = 18, 40, 50, 96, 132, etc., as shown in Figure 1.3 [WA82][AD83][WA88][MA90][WA92]. To account for these large enhancements, following possibilities were proposed from the theoretical point of view.

1. Heavy-meson exchange currents.
2. Weakening of the tensor force in the effective interaction.
3. Renormalization of the nucleon mass and the pion decay constant in the nuclear medium.

The heavy-meson exchange currents were calculated to examine whether they

have an additional contribution to the axial charges by Kirchbach et al. [KI92] who derived the short-range exchange current operators from the realistic nucleon-nucleon interaction, Bonn potential. They got fairly good agreement with experimental data in the framework of the Fermi gas model. On the other hand, the shell model calculations by Towner et al. [TO92] were strongly dependent on the cut-off parameters of the short-range correlation function which is necessary to take into account the repulsive force in the short-range between two nucleons. In addition, there seemed to be some shell dependence in the derivation. They gave reasonable enhancements in some cases, but could not for other cases. Thus, the effect of heavy meson seems to be not established yet in the present stage. As for the mass A = 12 system, the heavy-meson contribution has been studied quantitatively by Koshigiri et al. by employing Bonn potential [KO95a]. The resultant mesonic enhancement in the axial charge calculated by this theory was unchanged from the soft-pion prediction.

The strength of the tensor force in the effective interaction has to be considered [WA94b]. The core polarization effect affects the axial charge together with the meson exchange current, and is quite sensitive to the strength of the tensor force. Since the core polarization effect usually reduces the axial charge, weakening of the tensor force leads to the enhancement in the axial charge. However, quantitative discussion to all mass number is still in progress. Regarding the mass A = 12 system, the electron inelastic scattering on ^{12}C has been studied to show how much core polarization effect can be quantitatively included in this system [SA79]. The theoretical ambiguity from the core polarization effect is excluded in the A = 12 case.

Meanwhile, Kubodera, Rho and their coworkers introduced a new mechanism to explain large enhancements. The anomalously large enhancements are accounted for through the in-medium renormalization effect in the framework of the chiral

perturbation theory [KU91]. They derived about 20 % renormalization of the hadron effective masses for the nuclear matter density in order to reproduce the enhancement in the axial charge in the lead region. This approach looks promising, since the renormalization of approximately 10 % was found from the anomalously orbital g-factors of nuclear magnetic moments in heavy nuclei [YA85]. This theory remains to be investigated experimentally. Regarding the mass A = 12 system, this is a very favorable case to examine the in-medium effect in the axial charge, i.e. the baryon scaling, since two possibilities of the heavy-meson effect and the tensor interaction in the system have been well studied.

Thus, the alignment correlation terms in the β-ray angular distributions of the A = 12 system are one of the best candidates to discuss the mesonic enhancement in the axial charge. To make clear the anomalously large enhancements and to examine their mass dependence experimentally, the present experiment gives more reliable axial charge than the studies of the first-forbidden transitions in the following senses.

1. The axial charge matrix element is experimentally extracted from the alignment correlation terms, which is free from the theoretical calculation of any other matrix element.
2. The experimental method is less sensitive to the systematic errors which are canceled in the first order due to the relative measurement for the alignment correlation term.
3. There are few uncertainties in the theoretical calculation of the axial charge. The impulse term is reliably given due to the ratio relative to the main Gamow-Teller term, and the core polarization effect is given so as to incorporate with the experiment of electron scattering on ^{12}C. So, the meson exchange effect

in the axial charge is reliably compared with the experimental result. If the chiral filter mechanism was assumed, the in-medium effect is examined, since the mesonic enhancement is reliably given by the soft-pion theorem.

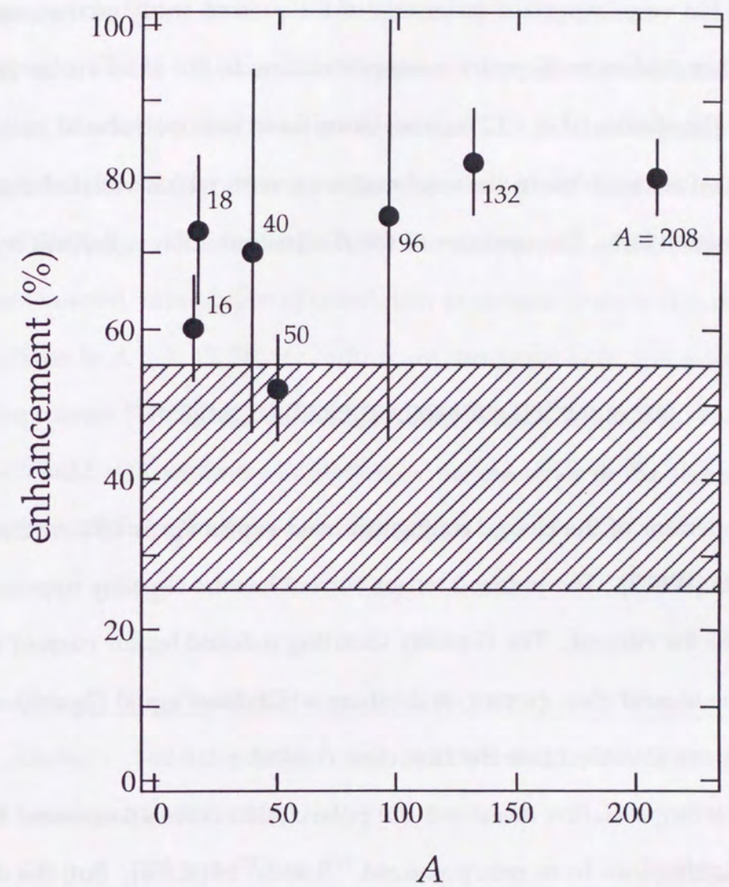

Figure 1.3 Summary of the enhancements in the axial charge matrix elements obtained from the first-forbidden transitions. The vertical axis shows the enhancements in the axial charges relative to the impulse calculations. The hatched area shows the enhancement predicted by KDR. Systematically large enhancements are found in overall nuclei, although the axial charges were dependent on the theoretical calculations of other forbidden matrix elements in the derivation.

1.4 Historical view and the present experiment

We mention on the very important influences of the present study of the axial charge to the other studies on G-parity conservation law in the axial-vector current.

Historically, the studies of $A = 12$ mirror decays have been performed in order to search the induced tensor term in the axial-vector current, which violated the G-parity conversation law. The operator of the G-transformation is defined by Weinberg as

$$G = C \exp(i\pi T_y), \tag{1.2}$$

where C is the operator of the charge conjugation and $\exp(i\pi T_y)$ is 180° rotation around iso-y axis [WE58]. The induced tensor current has the G-parity opposite from the main axial-vector current. The G-parity violating induced tensor current is classified into the second class current, and others which have equal G-parities to their main terms are classified into the first class current.

In 1975, Sugimoto et al. first measured the polarization correlation terms in the β-ray angular distributions from spin polarized ^{12}B and ^{12}N [SU75]. But, the definite conclusion could not be obtained on the existence of the induced tensor term, because the polarization correlation term was very much affected by the annoying systematic uncertainties such as the energy-dependent β-ray scattering effect in the large leading term which comes from the parity violation. Since then, the alignment correlation terms have been measured extensively by Osaka, Louvain, and ETH group, in order to search for the second class current [SU78][MA79][BR78a][LE78][BR78b][MI86][MI93]. It should be noted that these measurements had much relied on the hyperfine interactions of ^{12}B and ^{12}N in Mg

crystal accumulated by Osaka group, since without the knowledges of the hyperfine interactions we could not create artificially their spin alignments. The results up to now are listed in Table 1.3 where the alignment correlation coefficients $\alpha_{\mp}$ are given, the definition of which is described in the section 2.2. All data together with ft-value asymmetry are consistent with non existence of the second class current to the precision of $2Mf_T/f_A = -0.21 \pm 0.63$ [MA79]. For the purpose of the search for the second class current, other types of correlation experiments were also done; β-α and β-γ correlations in $A = 8, 19, 20$, etc., which are consistent with non existence of the second class current [TR75][MC80][BR95][CA75][TR78][DU78][RO88]. The present experiment could also set a new limitation on the existence of the second class current with much improved precision [MI98b].

Group	α_- (%/MeV)	α_+ (%/MeV)	ref.
Osaka	+0.025 ± 0.034	(-)0.277 ± 0.052	[SU78]
Louvain	-0.007 ± 0.020		[LE78]
ETH	+0.024 ± 0.044		[BR78a]
ETH	0.01 ± 0.03	(-)0.273 ± 0.039	[BR78b]
Osaka	+0.006 ± 0.018	-0.273 ± 0.041	[MA79]
Osaka85	+0.0046 ± 0.0053	-0.2795 ± 0.010	[MI86]
Osaka92	-0.0174 ± 0.0059	-0.2774 ± 0.0086	[MI93]

Table 1.3 Summary of the angular distribution experiments in the $A = 12$ system. The alignment correlation coefficients $\alpha_{\mp}$ are listed. The definition of them are described in the section 2.2.

Regarding the axial charge, the mesonic enhancement in the axial charge was not found in the pioneering works in the early 1970's, within the rather large experimental error. However, it was found by the theory group of Osaka that the core polarization effect significantly contributes to the axial charge [KO81]. By this, the experimental result was found to be consistent with the theory, since the core polarization effect reduces the axial charge and is counterbalanced with the mesonic enhancement. In 1985, the experimental technique was very much improved, so that the precision of the alignment correlation terms were much refined [MI86]. In this experiment, the enhancement in the axial charge was relatively larger than that expected for the KDR prediction. In 1992, the spin manipulation technique was further refined due to the improved knowledges of the hyperfine interactions of ^{12}B and ^{12}N implanted in Mg crystal [MI93a]. However, in the previous results of the axial charge, there was rather large fluctuation because of rather poor experimental errors in the data. In particular, the results for ^{12}B measured at 1985 and 1992 was inconsistent with each other, although the alignment correlation term of ^{12}B was very small, less than 1 %. Thus, it was necessary to refine the experimental technique in order to obtain a definite conclusion on the enhancement in the axial charge. This is also a crucial point to derive a mass dependence of the enhancement in axial charges.

For the complete improvement of the experimental technique, we have thoroughly studied again the hyperfine interactions of the mass A = 12 system in a Mg crystal. The knowledges of the hyperfine interactions of ^{12}B and ^{12}N in a Mg crystal have an important role in the present experiment. When measuring β-ray energy spectra from the aligned nuclei, high reliability and precision are required for the spin alignment, since the spin alignment is converted from the spin polarization produced through the nuclear reactions. The spin manipulation technique utilizes

the quadrupole interaction of ^{12}B and ^{12}N implanted in a Mg crystal (hexagonal closed packing) superimposed on their magnetic interactions with the externally applied strong magnetic field. Since the electric field gradient (EFG) is unique for the majority of ^{12}B and ^{12}N, the resonance frequency is split into $2I$ frequencies, I being the nuclear spin. Each resonance corresponds to the transition between neighboring two magnetic substates. A selective application of rf fields makes the spin manipulation possible to provide almost pure alignment of both signs without polarization.

In the recent β-NMR studies, it has been found that ^{12}B and ^{12}N are implanted in two kinds of implantation sites in a Mg crystal, i.e., two pairs of the resonances have been observed in the β-NMR spectrum. In the main site (fraction ~ 85 %), the EFG is parallel to the crystalline c-axis. In the second site, the EFG is perpendicular to the c-axis, with the same magnitude as that of the main component. This fact makes the spin manipulation complicated and less reliable unless the spin ensemble of the second site is manipulated properly. In the previous studies, this second component was not manipulated properly and, as a result, the experiment suffered from rather large systematic errors and uncertainties. The present study disclosed the origin of the second location. According to the studies by Kitagawa et al. [KI90][YA96], the second location arises from defects of some kinds in treatment of the sample or in synthesizing the crystal itself. In the present study, the spin manipulation technique was modified to remove the effect from the disturbing second location. Namely, the polarization of the second component was always destroyed, and that of the main component was only converted to the alignment to measure the alignment correlation terns. Thus, we rejected the systematic errors in deriving the alignment values.

Besides this improvement, we have accumulated much more counting statistics

in determining the precise alignment correlation terms, and reduced the possible systematic errors experimentally and theoretically.

In chapter 2, the theoretical background of the present study is briefly reviewed. The details on the experiment are described in chapter 3. The data analysis is described in chapter 4. The results and discussions are described in chapter 5.

Chapter 2

Theoretical background of the nuclear β decay

2.1 Interaction Hamiltonian

The Hamiltonian density of the nuclear β decay is described by the current-current type interaction,

$$H_I = \frac{1}{\sqrt{2}} J_\lambda L_\lambda + \text{h.c.}, \tag{2.1}$$

with

$$J_\lambda = V_\lambda + A_\lambda, \tag{2.2}$$

$$L_\lambda = -i\bar{\psi}_e(x)\gamma_\lambda(1+\gamma_5)\psi_\nu(x), \tag{2.3}$$

where the nucleon current J_λ consists of the vector current V_λ and the axial-vector current A_λ, and L_λ is the lepton current which has the form generating maximum parity violation. γ_λ is Dirac matrix. Hermitian conjugate h.c. represents positron decay. The vector and axial-vector currents have the following general form which is covariant under Lorentz transformation,

$$V_\lambda = i\bar{\psi}_p(f_V\gamma_\lambda + f_W\sigma_{\lambda\rho}k_\rho + if_S k_\lambda)\psi_n, \tag{2.4}$$

$$A_\lambda = i\bar{\psi}_p\gamma_5(f_A\gamma_\lambda + f_T\sigma_{\lambda\rho}k_\rho + if_P k_\lambda)\psi_n, \tag{2.5}$$

where f_V, f_W, f_S, f_A, f_T, and f_P are vector, weak magnetism, induced scaler, axial-vector, induced tensor and induced pseudoscaler terms, respectively. k_λ is the momentum transfer, $k_\lambda = k_p - k_n$, and $\bar{\psi} = \psi^\dagger \gamma_4$, and $\sigma_{\lambda\rho} = [\gamma_\lambda, \gamma_\rho] / 2i$. It is important to determine the coupling constants in the weak nucleon currents experimentally.

The main vector coupling constant f_V has been determined from $0^+ \rightarrow 0^+$ superallowed Fermi transitions, as

$$f_V/(\hbar c)^3 = (1.14959 \pm 0.00038) \times 10^{-5}\ \mathrm{GeV}^{-2}, \tag{2.6}$$

which is the most recent value given by Towner et al. [TO95], where the nuclear dependent radiative correction and the nuclear mismatch correction are taken into account.

The weak magnetism term is predicted as

$$f_W = -(\mu_p - \mu_n)\frac{f_V}{2M} = -\frac{3.706}{2M}, \tag{2.7}$$

from the CVC (Conserved Vector Current) hypothesis which is described in detail in the Sec. 2.4. Here, μ_p and μ_n are the anomalous magnetic moment of a proton and neutron, respectively, and M is the nucleon mass.

The induced scaler term becomes

$$f_S = 0, \tag{2.8}$$

from the divergence relation of the vector current in the CVC hypothesis.

The main axial-vector coupling constant f_A has been given from the angular

distribution of polarized neutron to be

$$f_A / f_V = -1.2601 \pm 0.0025\ [\mathrm{PA96}]. \tag{2.9}$$

The induced tensor term is classified as the second class current which has the different G-parity from its main term, where the G-transformation is defined as

$$G = C \exp(i\pi T_y). \tag{2.10}$$

Here C is the operator of the charge conjugation and $\exp(i\pi T_y)$ is 180° rotation around iso-y axis [WE58]. The induced scaler term in the vector current is also the second class current. According to the CVC hypothesis, the induced scaler term should be exactly zero, so that only the induced tensor term violates the G-parity. The G-parity of the system is conserved if the Hamiltonian is invariant under the charge conjugation and the isospin is conserved. The search for the G-parity violating second class current has been long performed in the mass 6, 8, 12, 19, and 20 system. Up to now, all data are consistent with non existence of the second class current,

$$f_T \approx 0. \tag{2.11}$$

The induced pseudoscaler term f_P is theoretically derived from PCAC (Partially Conserved Axial vector Current) hypothesis. PCAC gives the divergence relation

$$\partial A_\lambda = a\phi_\pi, \tag{2.12}$$

where a is related to the pion decay constant. Thus, the divergence of the axial vector is proportional to the pion field ϕ_π to allow a pion decay in the free space. This relation gives the induced pseudoscaler term as

$$\frac{f_P}{f_A} = \frac{2M}{m_\pi^2 + k^2}. \tag{2.13}$$

The induced pseudoscaler term has a very small contribution to the nuclear β decay because of small momentum transfer. The value has been experimentally determined from, for example, the muon capture in hydrogen to be

$$m_\mu \frac{f_P}{f_A} = 7.0 \pm 1.5, \tag{2.14}$$

which is consistent with the PCAC prediction of 6.8 [BA81].

2.2 β-ray angular distribution from the oriented nucleus

A new theory of nuclear β decay was formulated by Morita et al. [MO76][MO78], in which the higher order corrections such as the Coulomb correction for the finite size of the nucleus and higher partial waves of the lepton wave function are properly taken into account. For the analysis of the present study, it is necessary to employ such a formalism, since we are concerned with the quantities of the recoil order in the β decay.

The transition probability of β-ray emission with the energy between E and $E + dE$ in the angle $d\Omega_e$ is generally given by

$$\frac{dW}{dEd\Omega_e} = \frac{1}{(2\pi)^5} pE(E_0 - E)^2 \sum_{M_i} \rho_{M_i M_i} a_{M_i}, \tag{2.15}$$

with the density matrix defined by

$$\rho_{M_i' M_i} = \sum_{S_e S_\nu M_f} \int d\Omega_e \langle J_f M_f | H_I | J_i M_i \rangle \langle J_f M_f | H_I | J_i M_i' \rangle^*. \tag{2.16}$$

Here, the initial and final states are represented by $|J_i M_i\rangle$ and $|J_f M_f\rangle$, respectively, with their spins (Z components) J_i (M_i) and J_f (M_f). S_e and S_ν are the Z component of the spins of the emitted leptons. The β-ray energy (endpoint) and momentum are E (E_0) and p, respectively. a_{Mi} is the magnetic substate population with the normalization,

$$\sum_{M_i} a_{M_i} = 1. \tag{2.17}$$

The β-ray angular distribution from the oriented nucleus is explicitly given as

$$\frac{dW}{dEd\Omega_e} = \frac{G^2}{(2\pi)^4} pE(E_0 - E)^2 \sum_l \sum_{J \le J'} \hat{f}_l(J_i) \frac{1}{\sqrt{2J_i+1}} (-)^{J_f - J_i + J + J' + l} W(J_i J_i J J'; l J_f) b^l_{JJ'} \cdot P_l(\cos\theta), \tag{2.18}$$

with

$$\hat{f}_l(J_i) = \sum_{M_i} \sqrt{2J_i+1} (-)^{J_i - M_i} (J_i J_i M_i - M_i | l 0) a_{M_i}. \tag{2.19}$$

Here, $P_n(\cos\theta)$ is Legendre polynomials, and $W(J_i J_i J J'; l J_f)$ is Racah coefficients. The structures of the weak nucleon currents are all included in the particle parameter $b^l_{JJ'}$, the explicit form of which is given in [MO76]. In the above equation, the recoil effect of the final state nucleus is neglected. Using the impulse approximation, the β-ray angular distribution is written as

$$\frac{dW}{dEd\Omega_e} = \frac{G^2}{(2\pi)^4} F_0 pE(E_0 - E)^2 \frac{2}{2J_i+1} g_A^2 \langle\sigma\rangle^2 \{B_0 \mp P B_1 P_1(\cos\theta) + A B_2 P_2(\cos\theta)\}, \tag{2.20}$$

with

$$B_0 = L_0 \mp 4a\left(\frac{q}{3}L_0 + N_0\right) \pm 2b\left(\frac{q}{3}L_0 - N_0\right), \tag{2.21}$$

$$B_1 = 2\Lambda_1 \mp 4a\left(\frac{2q}{3}\Lambda_1 + N_{11} - \frac{1}{2}L_{12}\right) \mp 2b\left(-\frac{2q}{3}\Lambda_1 + N_{11} + L_{12}\right) \pm \frac{3}{\sqrt{10}} c L_{12}, \tag{2.22}$$

$$B_2 = \mp 2(a-b)L_{12} \mp \frac{3}{\sqrt{10}} c L_{12}, \tag{2.23}$$

where L_0, N_0, etc. are the combination of the electron wave functions which are also given in [MO76]. The parameters a, b and c are defined by

$$a = -\frac{1}{2}\frac{f_V\langle\alpha \times r\rangle}{g_A\langle\sigma\rangle}, \tag{2.24}$$

$$b = \pm\frac{f_A\langle i\gamma_5 r\rangle}{g_A\langle\sigma\rangle}, \tag{2.25}$$

$$c = -\frac{f_V\langle iA_{ij}\rangle}{g_A\langle\sigma\rangle}. \tag{2.26}$$

Here, $g_A = f_A \mp E_0 f_T$. In the case of $A = 12$, c is zero. The values $\boldsymbol{P}$ and $\boldsymbol{A}$ represent the spin polarization and alignment, respectively, which are defined by the magnetic substate populations as

$$P = a_{+1} - a_{-1}, \tag{2.27}$$

$$A = 1 - 3a_0, \tag{2.28}$$

$$\text{with } a_{+1} + a_0 + a_{-1} = 1. \tag{2.29}$$

In the limit of the point charge of the nucleus, the correlation terms in the eq. (2.20) are simply described as

$$\frac{B_1(E)}{B_0(E)} = \mp\frac{p}{E}(1+\alpha_{\mp}E), \tag{2.30}$$

$$\frac{B_2(E)}{B_0(E)} = \alpha_{\mp}E, \tag{2.31}$$

with

$$\alpha_{\mp} = \frac{2}{3}\left\{\pm\left(a - \frac{f_T}{f_A}\right) - \frac{y}{2M}\right\}, \tag{2.32}$$

where $B_1(E)$ and $B_2(E)$ are called the polarization and alignment correlation term, respectively. The upper and lower $\mp$ signs refer to the electron and positron decay, respectively. It is noted that the same term $\alpha_{\mp}E$ is included in the both polarization correlation term and alignment correlation term. It is difficult, however, to measure the polarization correlation term reliably, because the energy-independent leading term in the polarization term has dominant asymmetry. A small energy-dependent disturbance such as β-ray scattering gives spurious asymmetry easily in deriving the polarization correlation term.

The first term a in the alignment correlation coefficient $\alpha_{\mp}$ is the weak magnetism term, that is the ratio of the space like component of the vector to the

axial vector current as

$$a \approx -\frac{f_V}{f_A}\frac{1}{2M} + \frac{f_W}{f_A} = -(\mu_p - \mu_n + 1)\frac{f_V}{f_A}\frac{1}{2M}. \tag{2.33}$$

y is the ratio of the time like component of the axial-vector to the main axial-vector current,

$$y = -2Mi\frac{\int \gamma_5 r}{\int \sigma}, \tag{2.34}$$

where M is the nucleon mass. In the present study, we call this ratio y the axial charge for simplicity. In the non relativistic approximation, y is written as

$$y = 1 + 2i\frac{\int r(\sigma\cdot p)}{\int \sigma}. \tag{2.35}$$

Thus, the alignment correlation coefficient is composed of the weak magnetism term a, the induced tensor term f_T and the axial charge y. The sum of the alignment correlation coefficients in mirror decays singles out the ratio y as,

$$\alpha_- + \alpha_+ = -\frac{2}{3}\frac{y}{M}, \tag{2.36}$$

which is less sensitive to nuclear models and can be compared with the theoretical

calculations reliably. Similarly, the induced tensor term f_T can be derived from the difference between the alignment correlation coefficients,

$$\alpha_- - \alpha_+ = \frac{4}{3}\left(a - \frac{f_T}{f_A}\right). \tag{2.37}$$

Here, it should be mentioned that the precise axial charge is obtained by using the full formula with the higher order terms of the eq. (2.20), instead of the simple from of eq. (2.32), because the higher order terms in the alignment correlation term should not be neglected and are not canceled in the sum of the alignment correlation coefficients in the eq. (2.36). In the actual analysis, the alignment correlation terms were simultaneously fitted by the full formula of the eq. (2.20) for ^{12}B and ^{12}N. The simple analysis was only performed to check the consistency with the previous results.

2.3 Meson exchange current in the axial charge

In nuclear physics, the nuclear response to the external field is usually described as the sum of the those of the individual nucleons, that is called impulse approximation. Although this approach has been succeeded in many cases, it is necessary to take into account the effect of nucleons strongly interacting in the nucleus, for more precise description of the nucleus. Thus, the exchange current was introduced in the impulse calculation. Generally, the transition matrix element T is given as the sum of the contributions from the one-body and two-body operator as

$$T = \sum_{i=1}^{A} t(i) + \sum_{i<j=1}^{A} t(i,j) + \varepsilon, \tag{2.38}$$

where the higher order term ε is negligibly small. In the present case, the transition operator is the axial charge operator. In the low energy phenomena, the one-pion exchange current mainly contributes to the two-body current by the soft-pion theorem. In the diagram in Figure 2.1, the matrix element of the two-body current is given as

$$\begin{aligned}\tilde{J}_\lambda^\alpha &= (2\pi)^3 \delta(P_1 + P_2 + k - P_1' - P_2')\langle P_1' P_2' | J_\lambda | P_1 P_2 \rangle \\ &= (2\pi)^3 \delta(P_1 + P_2 + k - P_1' - P_2') \\ &\times \left\{ \langle \pi^\beta(q) N(P_1') | J_\lambda^\alpha | N(P_1) \rangle \frac{1}{q^2 + m_\pi^2} \langle N(P_2') | J_\pi^\beta | N(P_2) \rangle \right\},\end{aligned} \tag{2.39}$$

where P_i, P_i' and q are the four momentum of the initial nucleon, final nucleon, the

pion. k is the momentum transfer by the external field. α and β are the isospin indices of the current and the pion, respectively. $<\pi^{\beta}(q)\, N(p_1')\,|\,J_{\lambda}{}^{\alpha}\,|N(p_1)>$ is the pion production amplitude, and $<N(p_2')\,|\,J_{\pi}{}^{\beta}\,|N(p_2)>$ is the pion source current. In the present case, the external field J_{λ}^{α} is corresponding to the axial-vector current. According to the soft-pion theorem, the pion production vertex is given as

$$\left\langle \pi^{\beta}(q)N(P_1')\middle|J_{\lambda}^{\alpha}\middle|N(P_1)\right\rangle = i\frac{g_r}{Mf_A}\langle N(P_1)|[Q_{\beta}^{5}, J_{\lambda}^{\alpha}]|N(P_2)\rangle, \tag{2.40}$$

where g_r is the pion nucleon coupling constant. This is called the commutator term. Here, $Q_{\beta}{}^{5}$ is the axial charge operator defined as

$$Q_{\beta}{}^{5} = \int d^3x\, A_0{}^{\beta}(x, 0). \tag{2.41}$$

Here, the current algebra holds,

$$[Q_{\beta}{}^{5}, A_{\lambda}{}^{\alpha}] = i\varepsilon_{\alpha\beta\gamma} V_{\lambda}{}^{\gamma}, \tag{2.42}$$

$$[Q_{\beta}{}^{5}, V_{\lambda}{}^{\alpha}] = i\varepsilon_{\alpha\beta\gamma} A_{\lambda}{}^{\gamma}. \tag{2.43}$$

These relations imply that the magnitude of the time like component $\lambda = 4$ of the axial-vector current corresponds to that of the vector current $\gamma_{\lambda} \sim \kappa O(1)$, while the space like component $\lambda = 1 \sim 3$ is recoil order $\gamma_{\lambda} \sim \kappa O(p/M)$, as is listed in Table 1.1. Thus, the axial charge is significantly enhanced by the one-pion exchange current, as predicted by KDR [KU78]. Finally, the pion production amplitude and the pion source current is given as

$$\left\langle \pi^{\beta}(q)N(P_1')\middle|J_4^{\alpha}\middle|N(P_1)\right\rangle = \frac{g_r}{Mf_A} i\varepsilon_{\alpha\beta\gamma}\tau_1^{\gamma}, \tag{2.44}$$

$$\langle N(P_2')|J_{\pi}^{\beta}|N(P_2)\rangle = ig_r\frac{\sigma\cdot q}{2M}\tau_2^{\beta}. \tag{2.45}$$

Thus, the transition operator of the two-body current is obtained in the non relativistic form as

$$\tilde{J}_4^{\alpha} = \frac{1}{(2\pi)^3}\delta^3(P_1 + P_1' + k - P_2 - P_2')\frac{g_r^2}{Mf_A}\frac{1}{q^2 + m_{\pi}^2}\frac{\sigma\cdot q}{2M}(\tau_1 \times \tau_2)^{\alpha}. \tag{2.46}$$

The exchange current operator in the coordinate space is obtained by the Fourier transformation of that in the momentum space as follows

$$\rho_A(x) = \rho_A^1(x) + \rho_A^2(x), \tag{2.47}$$

with

$$\rho_A^1(x) = \sum \tau_i^{\pm}\delta(x - x_i)\left\{f_A\frac{\sigma_i\cdot p_i}{2M} + (\pm 2Mf_T + E_0 f_P)\frac{\sigma_i\cdot k_i}{2M}\right\}, \tag{2.48}$$

$$\rho_A^2(x) = -\frac{1}{2f_A}\frac{g_r^2}{4\pi}\left(\frac{m_{\pi}}{M}\right)^2\sum_{i<j}(\tau_i\times\tau_j)^{\pm}\left\{\sigma_i\hat{r}\delta(x - x_j) + \sigma_j\hat{r}\delta(x - x_i)\right\}Y_1(m_{\pi}r), \tag{2.49}$$

and $$Y_1(x) = \left(1+\frac{1}{x}\right)\frac{e^{-x}}{x}. \tag{2.50}$$

Here, $\rho_A{}^1$ and $\rho_A{}^2$ are the axial charge operator of the one-body and two-body current, respectively.

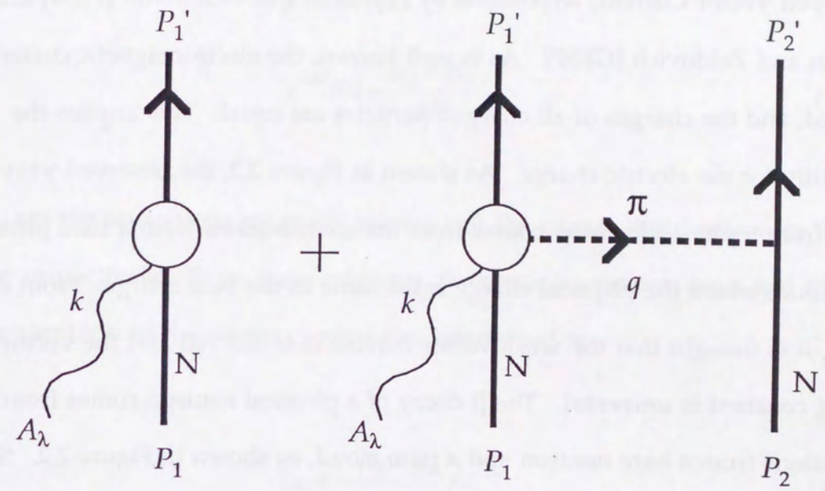

"one-body" "two-body"

Figure 2.1 Diagram of the one-body and two-body currents which interact with the weak current. In the two-body current, the one-pion exchange currnet is dominant for the low energy phenomena. In the right figure, the pion is produced through the interaction of the nucleon with the external field A_λ, and is absorbed again by other nucleon. The pair current mainly contributes to the exchange current in the case of axial-vector decay.

2.4 Strong CVC hypothesis

Originally, Fermi introduced the weak interaction in an analogy with the electromagnetic interaction. This analogy was extensively generalized as the CVC (Conserved Vector Current) hypothesis by Feynman and Gell-Mann [FE58] and Gershtein and Zeldovich [GE57]. As is well known, the electromagnetic current is conserved, and the charges of all charged particles are equal. This implies the universality for the electric charge. As shown in Figure 2.2, the observed γ-ray emitted from a physical proton comes from the contributions from a bare proton and a pion cloud, where the physical charge is the same as the bare charge. From this analogy, it is thought that the weak vector current is conserved and the vector coupling constant is universal. The β decay of a physical neutron comes from the contributions from a bare neutron and a pion cloud, as shown in Figure 2.2. So, the divergence relation holds,

$$\partial V_\lambda = 0. \tag{2.51}$$

Another important assumption is that the isovector part of the electromagnetic current and the weak vector currents form the components of the isovector current. This is called the isotriplet vector current hypothesis. From this assumption, the structure of the weak vector current is derived. The isovector part of the electromagnetic current is given as

$$J^{\mathrm{EM}} = e\overline{\psi}_1(f^{\mathrm{EM}}\gamma_\mu - ig^{\mathrm{EM}}\sigma_{\mu\nu}p_\nu)\psi_2. \tag{2.52}$$

Here f^{EM} and g^{EM} are the charge and magnetic form factors of the nucleon. These

form factors have the decreasing function of the momentum transfer p^2, and have the following forms,

$$f^{\mathrm{EM}}(0) = 1, \tag{2.53}$$

$$g^{\mathrm{EM}}(0) = \frac{\mu_{\mathrm{p}} - \mu_{\mathrm{n}}}{2M}. \tag{2.54}$$

μ_{p} and μ_{n} are the anomalous magnetic moment of the proton and neutron in the free space, respectively. From these relations, the weak magnetism term and the induced scaler term in the vector current are determined as

$$f_W = -\frac{\mu_{\mathrm{p}} - \mu_{\mathrm{n}}}{2M} f_{\mathrm{V}}, \tag{2.55}$$

$$f_{\mathrm{S}} = 0. \tag{2.56}$$

In experiments, the CVC hypothesis has been tested by the shape factor in β-ray energy spectrum and the γ-decay width $\Gamma\gamma$ of the analog transition. The best known candidate is the β decay of the mass A = 12 system; ^{12}B-^{12}C-^{12}N isotriplet. The β-ray energy spectrum has the effect of the weak magnetism term, and is described as

$$W_{\mp}(E) \propto pE(E_0 - E)^2\left(1 \pm \frac{8}{3}aE\right), \tag{2.57}$$

where a is the weak magnetism term defined as

$$a = \frac{\mu}{2M}\left|\frac{f_V}{f_A}\right|. \tag{2.58}$$

Here, μ is the transition moment, $\mu = 1 + \mu_p - \mu_n$. The magnitude of the weak magnetism term a is very small ≤ 1 %, but it has opposite sign to the positron and electron decay, so that the effect is enhanced two times in observing the both decays. Several experiments have been performed until now, using different method; the magnetic spectrometers, inorganic-, and plastic-scintillation counters [WU77][KA77][CA90][FU96]. The summary is shown in Table 2.1. All data are consistent with the CVC prediction, but the precision looks rather poor. Therefore, we use the weak magnetism term obtained from the γ-ray width of the analog transition of ^{12}C, in extracting the axial charge from the alignment correlation terms.

Group	$a_- - a_+$ (%/MeV)	ref.
Wu et al.	0.86 ± 0.24	[WU77]
Kaina et al.	1.09 ± 0.09	[KA77]
Camp	1.24 ± 0.42	[CA90]
Fukuda et al.	0.99 ± 0.41	[FU96]
Theory	1.14 ± 0.02	[KO86]

Table 2.1 Summary of the spectral shape factor in the β-ray energy spectra of the A = 12 mirror nuclei.

The analog M1 transition $^{12}C^*(15.11\ \text{MeV}) \rightarrow {}^{12}C(\text{ground})$ has been precisely observed by the electron scattering experiments. The gamma width Γ_γ is related the γ decay rate as

$$\Gamma_\gamma = \frac{\mu^2 |\int \sigma|^2}{2\times 3}\frac{\alpha E_\gamma^3}{M^2}, \tag{2.59}$$

where $E\gamma$ is the γ-ray energy and α is the fine structure constant. In the above equation, the Gamow-Teller matrix element is obtained from the ft-value as follows

$$\frac{ft_{0\to 0}}{ft} = \frac{|\int \sigma|^2 f_A^2}{2 f_V^2}. \tag{2.60}$$

From the eq. (2.58)-(2.60), the weak magnetism is given as

$$a = \sqrt{\frac{3}{4\alpha}\frac{\Gamma_\gamma}{E_\gamma^3}\frac{ft}{ft_{0\to 0}}}, \tag{2.61}$$

for this analog transition. $ft_{0\to 0}$ is ft-value of the β decay for the superallowed transition. The average value $\Gamma_\gamma = 38.2 \pm 0.6$ eV of all available data [EN68][CH73][DE83] gives the weak magnetism term to be

$$a_{\text{exp.}}^{\text{ave.}} = 4.02 \pm 0.02\ (1/2M). \tag{2.62}$$

It is noted that the isospin mixing of $T = 0$ [illegible] ate must be properly taken into account in the analy[illegible] support the strong CVC hypothesis.

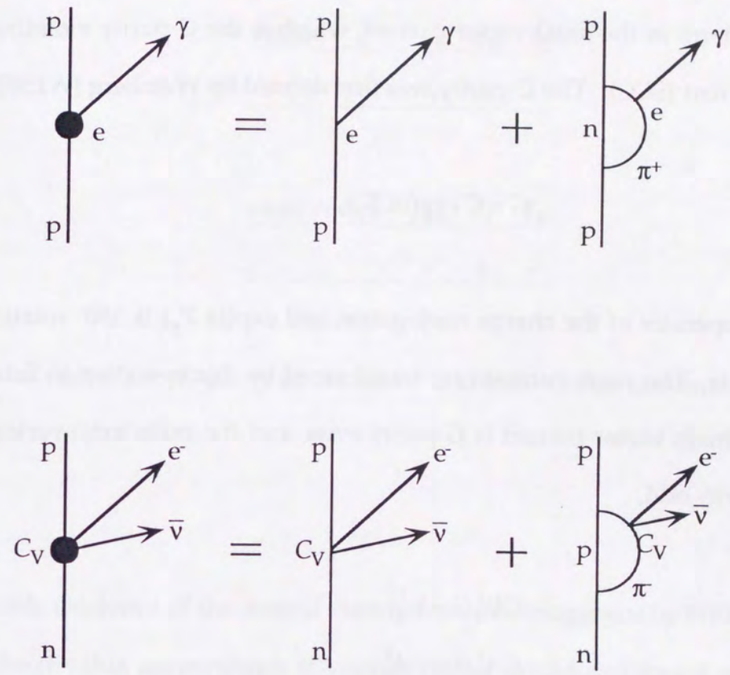

Figure 2.2 Comparison of the γ-decay and the weak vector decay. The γ-ray from the physical proton comes from the contributions from a bare proton and a pion cloud. Similarily, in the weak vector decay, the β decay has the contribution from a bare neutron and a pion cloud.

2.5 Second class current

The present experiment can place the limitation of a possible existence on the induced tensor term in the axial-vector current, which is the G-parity violating second class current (SCC). The G-parity was first defined by Weinberg [WE58] as

$$G = C \exp(i\pi T_y), \tag{2.63}$$

where C is the operator of the charge conjugation and $\exp(i\pi T_y)$ is 180° rotation around iso-y axis. The weak currents are transformed by this operation as listed in Table 2.2. The main vector current is G-parity even, and the main axial-vector current is G-parity odd,

$$GV_\lambda^{\mathrm{I}}G = V_\lambda^{\mathrm{I}}, \tag{2.64}$$

$$GA_\lambda^{\mathrm{I}}G = -A_\lambda^{\mathrm{I}}. \tag{2.65}$$

The induced term with the G-parity equal to the main term is classified into the first class current, and that with the G-parity different from the main term is classified into the second class current. As listed in Table 2.2, the induced scaler term in the vector current and the induced tensor term in the axial-vector current are classified into the second class current. The search for the second class current is very important for the structure of the weak nucleon current, since the nuclear β decay is symmetric in the isospace under the G-parity invariance.

vector	f_V	f_W	f_S
	+	+	-

axial vector	f_A	f_T	f_P
	-	+	-

Table 2.2 G-parity of the vector and axial-vector current.

A possible existence of the second class current was suggested by Wilkinson, who analyzed the ft-value asymmetries of various mirror nuclei and found systematic deviations from the symmetries [WI70]. The ft-value asymmetry is written as

$$\frac{(ft)_+}{(ft)_-} - 1 = \delta_{\mathrm{exp}} = \delta_{\mathrm{SCC}} + \delta_{\mathrm{nucl.}} \tag{2.66}$$

Here δ_{SCC} is the contribution from the SCC, and $\delta_{\mathrm{nucl.}}$ comes from the asymmetry of the Gamow-Teller matrix elements in mirror nuclei, which is caused by the electromagnetic interaction. Kubodera, Delorme and Rho analyzed the ft-value asymmetries systematically using the KDR model [KU73], but the results strongly depended on the nuclear models.

For this purpose, the alignment correlation terms in the β-ray angular

distributions of the $A = 12$ system have been long studied, which are less sensitive to the nuclear models as described at section 2.2. Up to now, all results from the angular distributions and correlations are consistent with non existence on the second class current. The results of the second class current are shown in Figure 2.3, which were obtained from the data in Table 1.3 using the simple analysis described at the section 2.2. However, a possible mass and/or charge difference between up and down quarks causes the second class current. The present study gave the strict limitation of the existence on the second class current, which is described in detail in the section 5.3. Here, it is noted that the induced scaler term is the second class current, too. This has to be also searched by the experiment, although the induced scaler term is zero according to the strong CVC hypothesis. In the present $A = 12$ experiment, the induced scaler term does not contribute to the alignment correlation term, even if it exists.

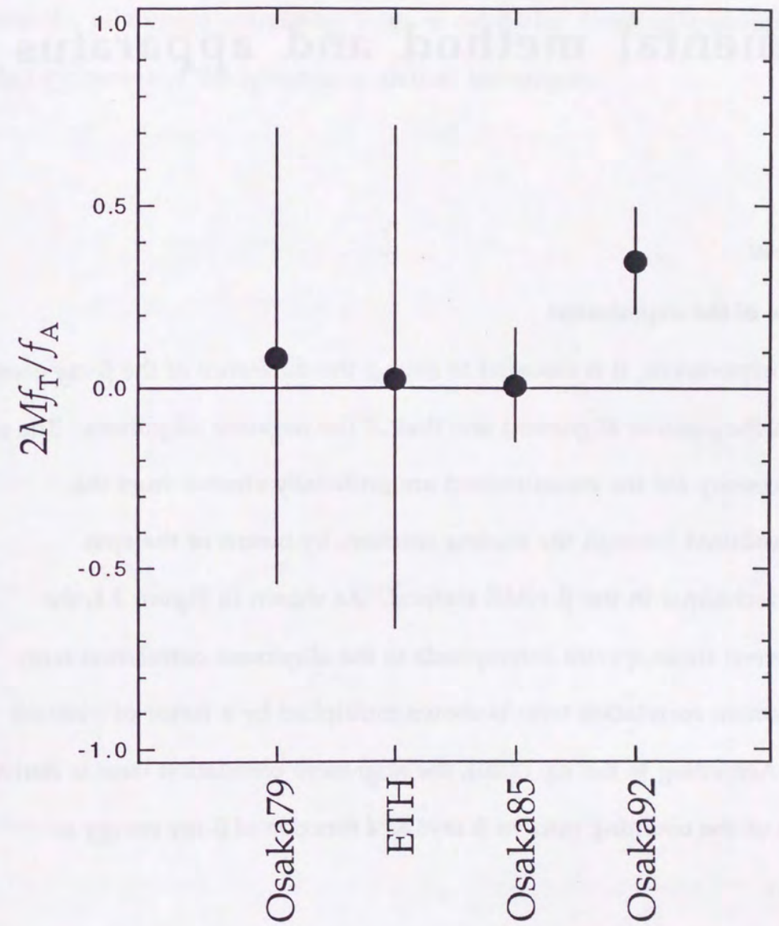

Figure 2.3 Summary of the induced tensor term in the axial-vector current. The induced ternsor terms were calculated from the differences between the alignment correlation coefficients listed in Table 1.3, according to the eq. (2.37) in the section 2.2.

Chapter 3

Experimental method and apparatus

3.1 Overview

3.1.1 Principle of the experiment

In the present experiment, it is essential to extract the difference of the β-ray energy spectrum with the positive alignment and that of the negative alignment. The spin alignments necessary for the measurement are artificially created from the polarization produced through the nuclear reaction, by means of the spin manipulation technique in the β-NMR method. As shown in Figure 3.1, the difference between those spectra corresponds to the alignment correlation term. Here, the alignment correlation term is shown multiplied by a factor of ~100 for convenience. According to the eq. (2.20), the alignment correlation term is derived from this ratio of the counting rates of β rays as a function of β-ray energy as

$$\frac{B_2(E)}{B_0(E)} = \frac{1}{\Delta A}\left(\frac{N(E,\theta,A^+)}{N(E,\theta,A^-)} - 1\right), \tag{3.1}$$

$$\text{with} \quad \Delta A = A^+ - A^-, \tag{3.2}$$

where $N(E, \theta, A^{\pm})$ is the β-ray counting rate in the spectrum with the positive or negative alignment without polarization, that was measured by the β-ray counter

telescope placed at 0° (up) and 180° (down) relative to the spin orientation axis. The difference ΔA between the positive and negative alignment, which is necessary to determine the alignment correlation term, is calculated from polarization-changes controlled by means of the spin manipulation technique.

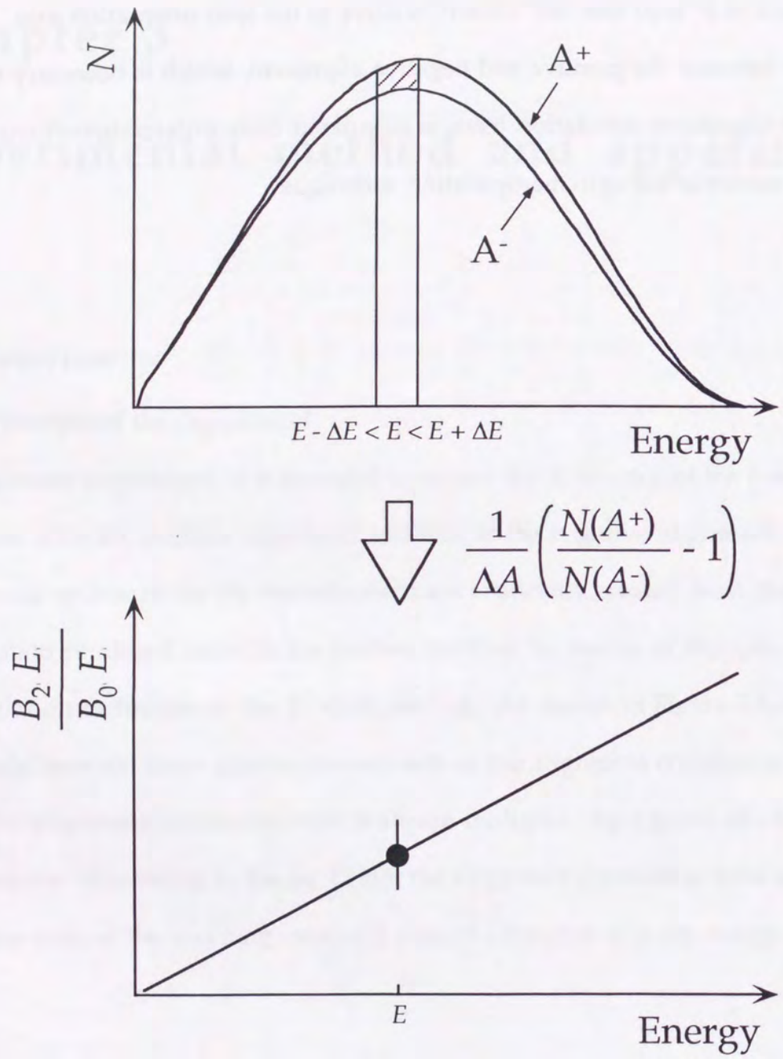

Figure 3.1 Principle for the measurement of the alignment correlation terms. In the upper figure, the difference between two spectra with positive and negative alignment corresponds to the alignment correlation term which is derived from the ratio of them as a function of energy (lower figure).

3.1.2 Survey of the experimental method

One of the essential part of the present experimental method in measuring the alignment correlation terms is the conventional β-NMR method. Using the pulsed beam technique, four processes described below are repeated sequentially for the measurements of the alignment correlation coefficients;

1. production of polarized nuclei, ^{12}B and ^{12}N,
2. maintenance of the polarization following recoil implantation into a Mg single crystal,
3. spin manipulation; creation of spin alignment from spin polarization, and
4. β-ray spectrum measurements.

Firstly, polarized ^{12}B and ^{12}N nuclei are produced through the nuclear reaction. Then, they are implanted into an implantation medium, a recoil stopper made of a single crystal Mg which has the electric field gradient parallel to its c-axis at the site where the nuclei reside. The polarization produced by the nuclear reaction is manipulated and converted to the spin alignment by a set of rf-fields using the NMR method in high magnetic field, frequencies of which are split caused by the quadrupole interaction in the stopper. Finally, β-ray spectra from aligned nuclei are measured. The production-counting cycles with positive and negative alignments are alternatively repeated until enough counting statistics are accumulated. The whole experimental setup is shown in Figure 3.2. Details of the experiment are described in the following sections.

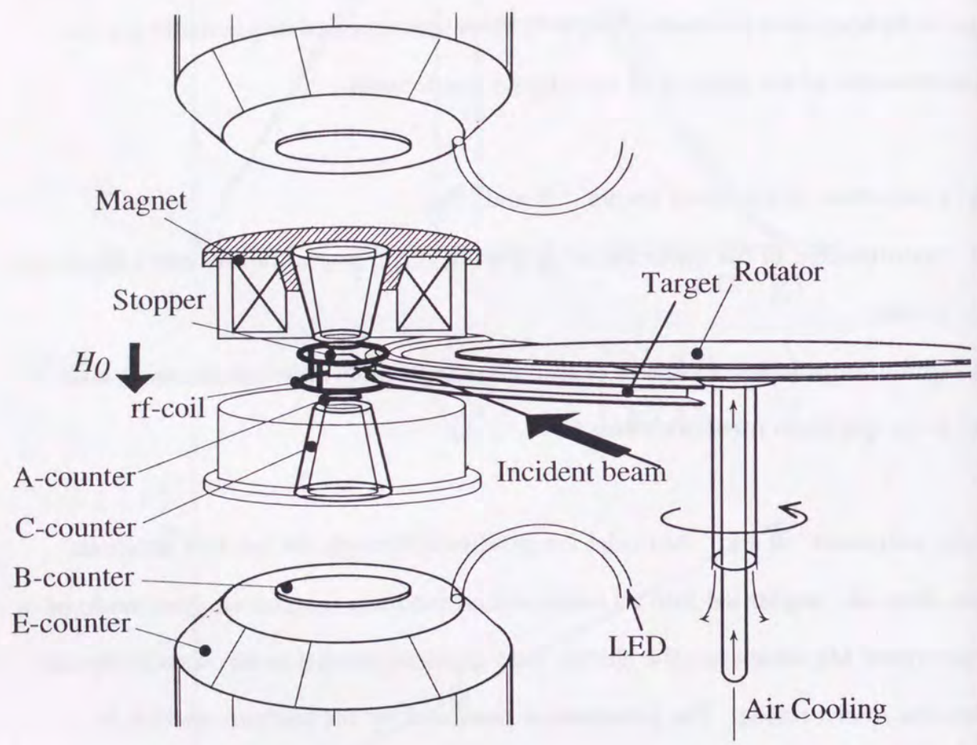

Figure 3.2 Schematic view of the experimental setup.
The rotating target system, recoil stopper, rf coil, magnet, and up-down β-ray counter telescopes are shown. The rotating target system, recoil stopper and rf coil are set in vacuum in the reaction chamber whose part near the recoil stopper are made of plastics to prevent the β-ray scattering.

3.1.3 Comment on the experimental technique

The present experiment requires high reliability for the spin manipulation technique and the spectrum measurements, since the alignment correlation term is a very small quantity, an order of a few %. The present method is quite unique and less sensitive to systematic uncertainties.

The correlation term to be measured is appeared both in the polarization term and in the alignment term, as described in the section 2.2. Although the polarization produced by the nuclear reaction is large enough to measure the polarization correlation term, the present polarization correlation term $\alpha_{\mp}E$ can not be reliably extracted out from the leading parity violating allowed term. It is easily affected by energy-dependent disturbances such as β-ray scattering which is easily become comparable with the $\alpha_{\mp}E$ value. So, it is much more reliable to measure the alignment correlation term directly if the alignment is created artificially since there exists no leading parity violating allowed term, although the initial alignment produced by the nuclear reaction is small, a few %. The spin alignments necessary for the measurements of the alignment correlation terms are realized by the present spin manipulation technique. The efficiency to manipulate the spin ensemble is so high that almost pure aligned ensemble with the vanishingly small polarization can be created from the polarization by using this technique. Besides, the difference between the positive and negative alignment created by the spin manipulation is three times larger than initial polarization produced by the nuclear reaction, $\Delta A = 3P_0$, as will be later described. In addition, as understood from the correlation coefficients, the ratio of β-ray spectra with positive and negative alignment is almost free from the energy-dependent systematic uncertainties such as background, scattering, response of the β-ray counters, and so on, since they are all small fractions that can be estimated.

3.2 Production of spin polarized ^{12}B and ^{12}N

3.2.1 Rotating target system

The experiment was performed using the 4.75-MV Van de Graaff accelerator at Osaka University. The incident beam from the accelerator is analyzed by a dipole magnet, and focused on the target by the quadrupole magnet and X-Y steering magnets, as shown in Figure 3.3. In order to realize the timing sequence described in the section 3.6, the pulsed beam technique was employed. The continuous beam from the accelerator was pulsed by a combination of the electrostatic deflector and a chopper stopper as shown in Figure 3.3. The beam was on during the production time to bombard the target, and was stopped by the chopper system during rf and counting times.

The rotating target system was employed as shown in Figure 3.4. The target rotor rotates at a period of 60 ms. The target ribbon is set in a groove of the target holder which is connected on the side of the rotor. The beam pulsing is synchronized with the rotation of the rotor. This system makes background activities much reduced, since the target rotor is moved far away from the solid angle of the β-ray counter telescopes to the opposite side of the stopper during the following counting time and is shielded by lead blocks. The target holder is cooled by an air-jet from inside of the rotor. The air-jet was cooled by use of the system which utilizes air expansion and heat exchanging system given in the Figure 3.2. The rotation of the target system is detected by the photosensitive rotation-pickup system. This system consists of bulbs and CdS cells that detect the change of the lights when the rotor cuts the paths of the lights, i.e., when the target system rotates across between the pair of the bulb and CdS to cut the light, the pulses are generated at the timing corresponding to the target-in

or target-out positions. This rotation pickup system is schematically shown in Figure 3.5. The timing pulse generated by this system starts the timing sequence. The control of the whole system is described in the section 3.6.

Figure 3.3 Schematic view of the beamline. The beam from the accelerator is analyzed by the magnet, and focused on the target by the steering magnets and the quadrupole magnet. The continuous beam is pulsed by the electric deflector.

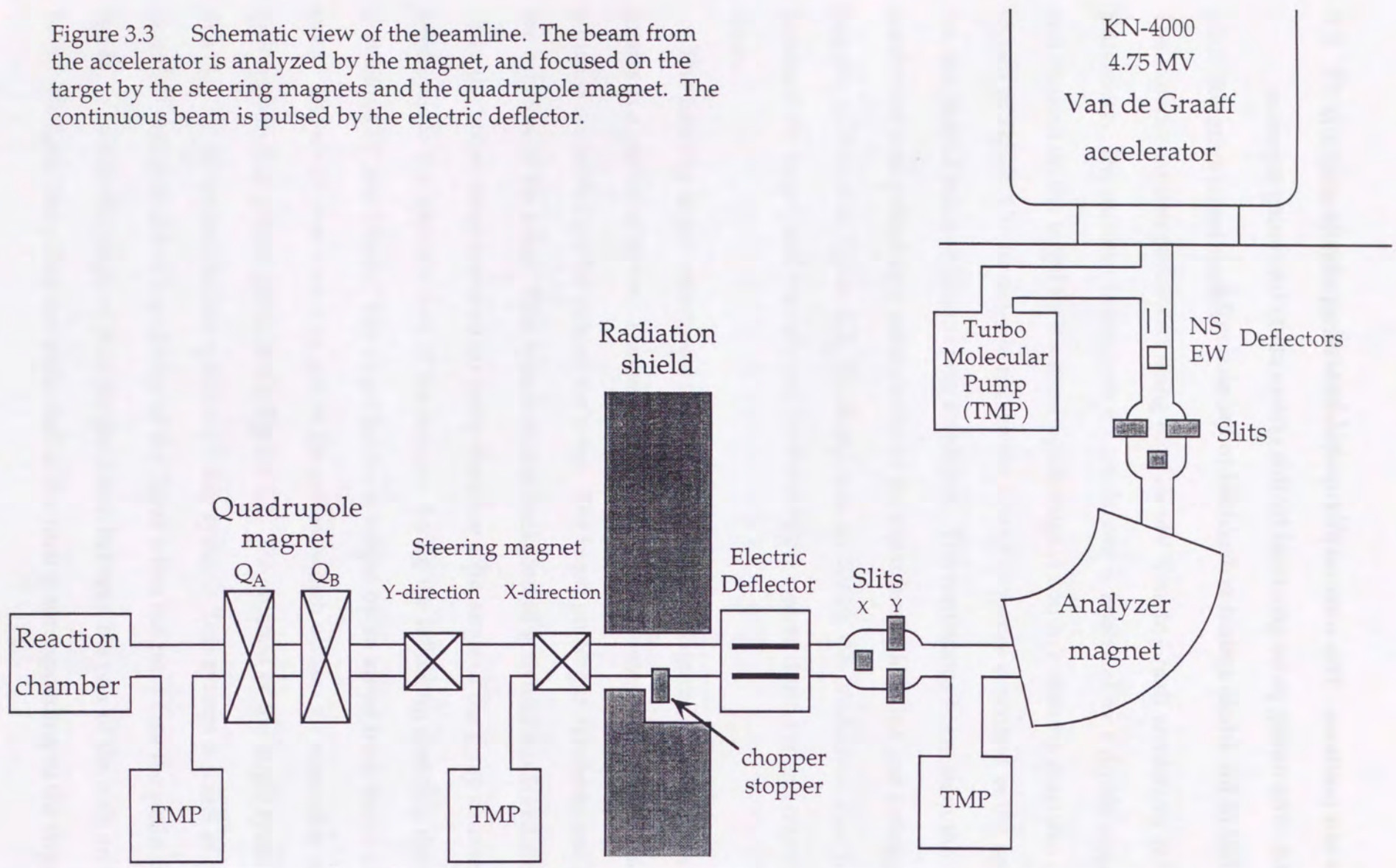

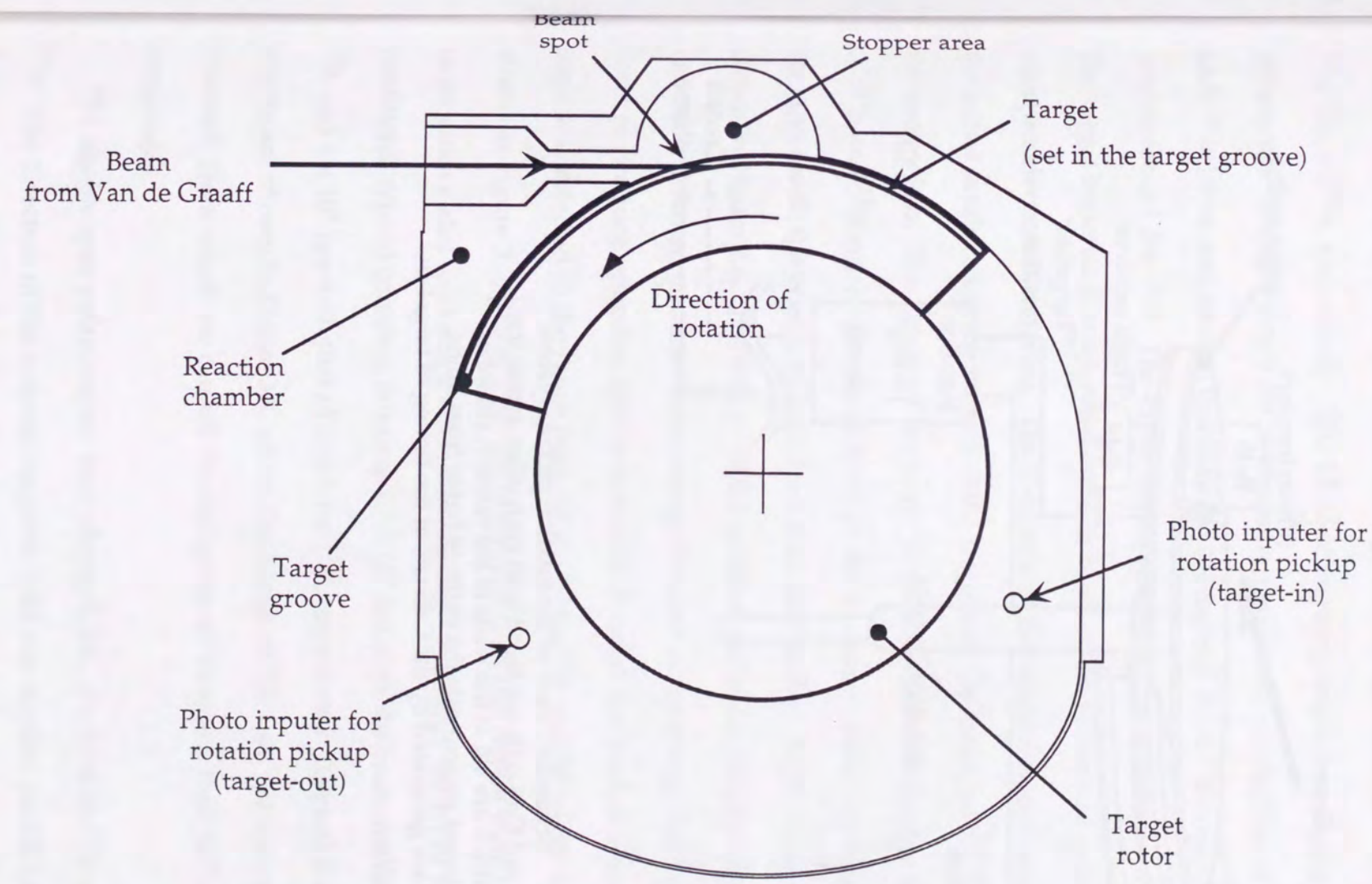

Figure 3.4 Schematic view of the reaction chamber (horizontal cross section). The rotating target system is shown. The pulsed beam bombards the target in the groove only during the production time, which rotates at a period of 60 ms.

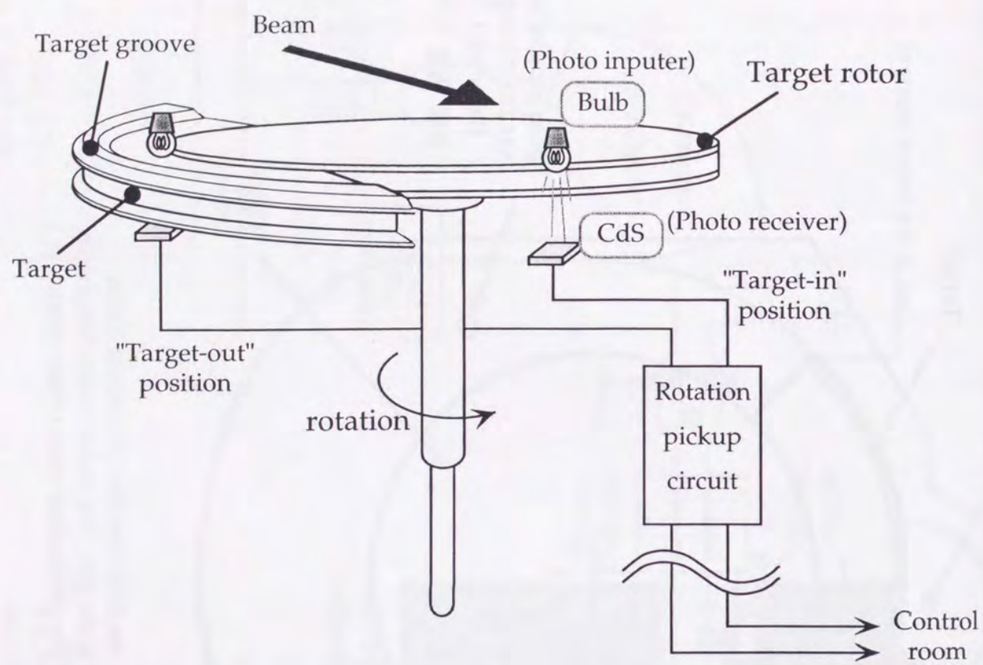

Figure 3.5 Schematic view of the rotation pickup system. The bulbs and CdS cells are faced with each other across the vacuum, which are set at the walls of the reaction chamber. When the target groove cuts the paths of lights from bulbs, the pulses are generated by the CdS cell at the timing of target-in or target-out.

3.2.2 Production of ^{12}B and ^{12}N

^{12}B and ^{12}N nuclei were produced through the nuclear reaction $^{11}B(d, p)^{12}B$ and $^{10}B(^{3}He, n)^{12}N$, respectively. The 1.5 MeV deuteron beam was used to bombard the 300-μg/cm^2 thick ^{11}B target (99 % concentration) for the production of ^{12}B, and the 3.0 MeV ^{3}He beam was used to bombard the 300-μg/cm^2 thick ^{10}B target (90 % concentration) for ^{12}N. The experimental conditions are summarized in Table 3.1. The target material is evaporated on Mo ribbon at the vacuum of order 10^{-6} torr, using an electron bombarder. The thickness of the target was determined to allow the nuclei produced at the bottom of the target can come out, taking into account of the energy loss. The details of the target preparation are described in the appendixes.

^{12}B and ^{12}N nuclei produced through the nuclear reaction are recoiled out from the target with the energy of maximum 0.44 MeV and 1.5 MeV, respectively, as is shown in Figure 3.6. The energy of the recoiled nuclei are distributed almost uniformly from zero to maximum energy because of the energy loss in the target. In order to produce optimum spin polarization through the nuclear reaction, the recoil angle was selected to the range from 40° to 75° for ^{12}B and 20° to 55° for ^{12}N. As shown in Figure 3.7, β rays from the stopper only in this region were observed. The target groove also works as a kind of a collimator to restrict the recoil angle. In these conditions, typical counting rates are 1.5×10^3 cps with the beam intensity of 5 μA for ^{12}B, and 1×10^2 cps with that of 20 μA for ^{12}N, respectively. Typical β-ray time spectra are shown in Figure 3.8, where the decays of ^{12}B and ^{12}N was clearly observed, from which we can tell the backgrounds were less than 10^{-2} of the main component.

The sizable spin polarizations were obtained, i.e., $P \sim 10$ % for ^{12}B and 20 % for ^{12}N. The direction of the external magnetic field was applied parallel to the spin polarization for both ^{12}B and ^{12}N nuclei, as shown in Figure 3.9. The spin

polarization was determined from the β-ray asymmetry change determined from the counting rate ratios between the up and down β-ray counter telescopes. The details of determining the polarization are described in the section 4.2.

	^{12}B	^{12}N
Reaction	$^{11}B(d, p)^{12}B$	$^{10}B(^{3}He, n)^{12}N$
Beam energy	1.5 MeV	3.0 MeV
Q-value	1.1444(13) MeV	1.5631(90) MeV
Beam intensity (typ.)	5 μA	20 μA
Recoil angle	40° ~ 75°	20° ~ 55°
Recoil energy (typ.)	0.44 MeV	1.5 MeV
β-ray yield (typ.)	1.5×10^3 cps	1×10^2 cps
Magnetic field	300 Oe	600 Oe
Stopper	Mg	Mg
Implantation depth	1.5 μm	2.7 μm

Table 3.1 Experimental conditions.

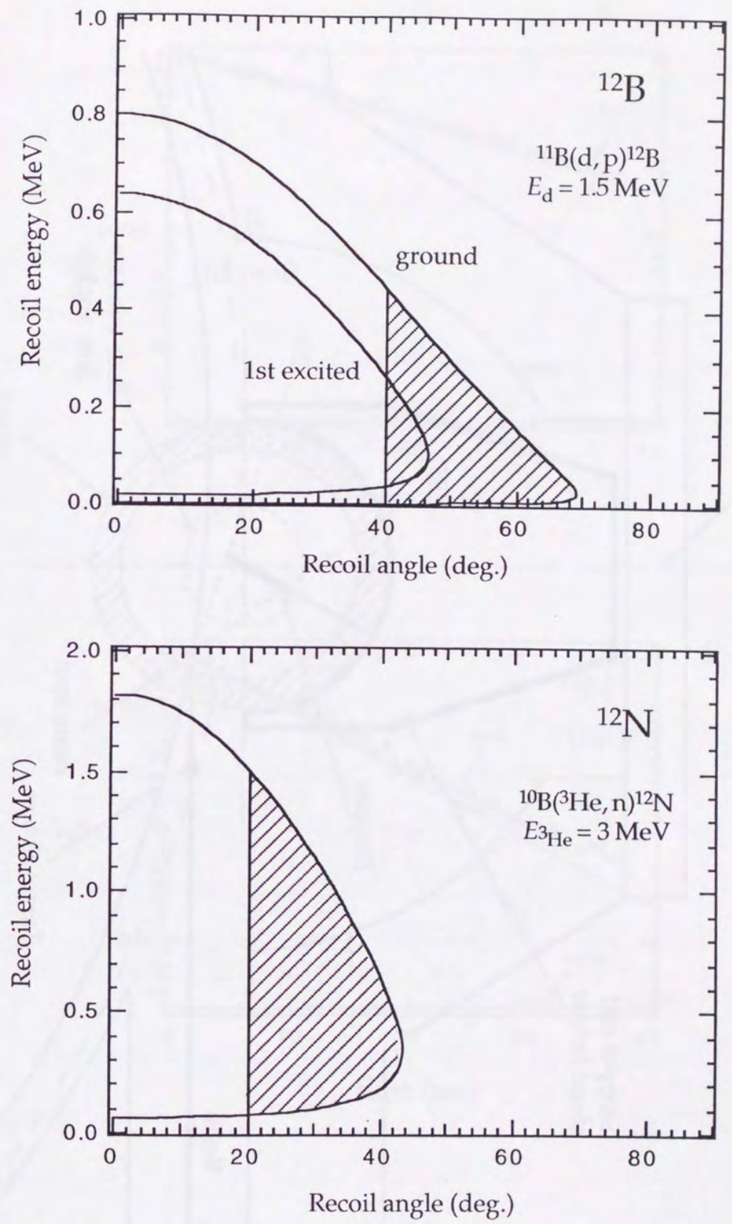

Figure 3.6 Kinematics of the recoiled nuclei. The nuclei in the hatched areas are allowed to be implanted in the stopper.

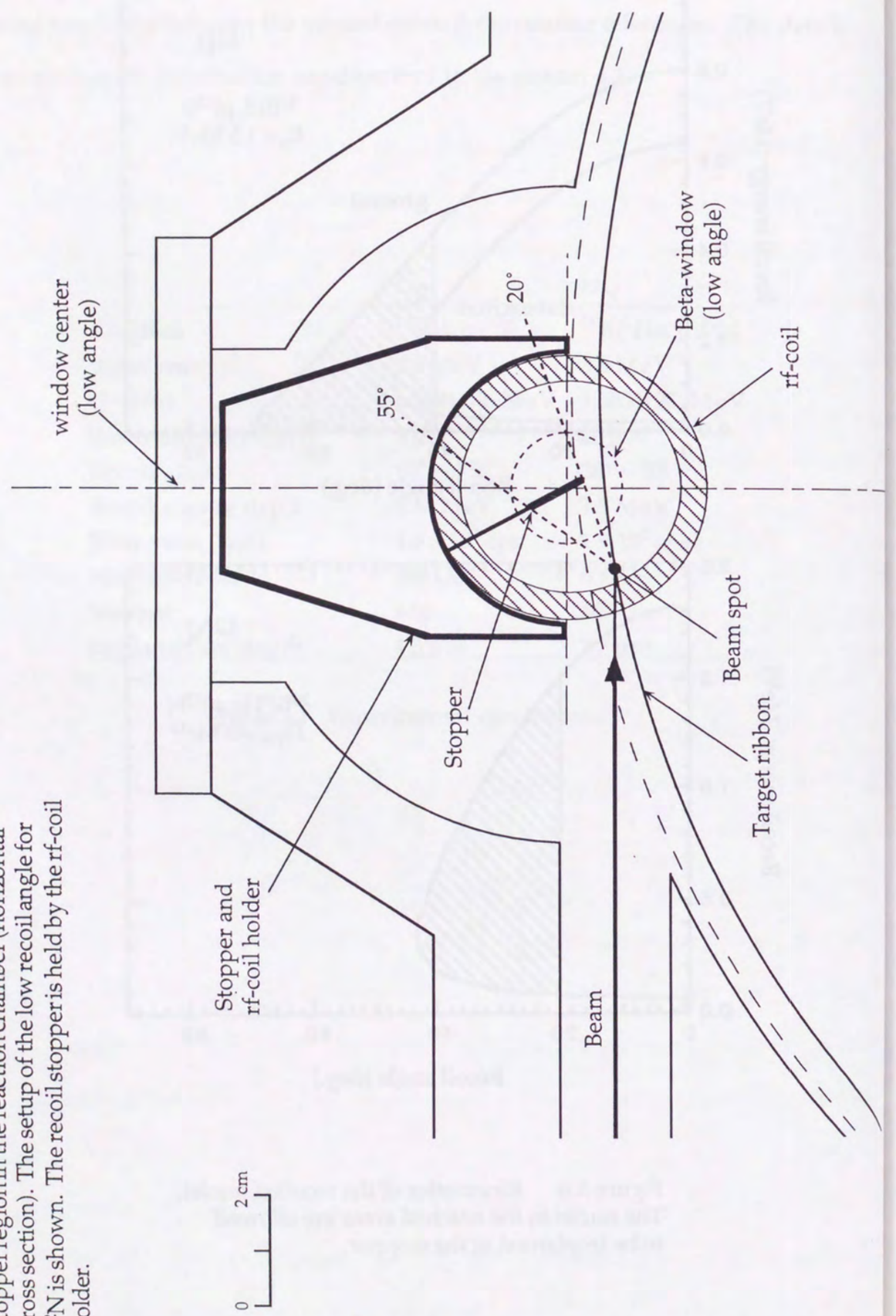

Figure 3.7 Schematic view of details around the stopper region in the reaction chamber (horizontal cross section). The setup of the low recoil angle for ^{12}N is shown. The recoil stopper is held by the rf-coil holder.

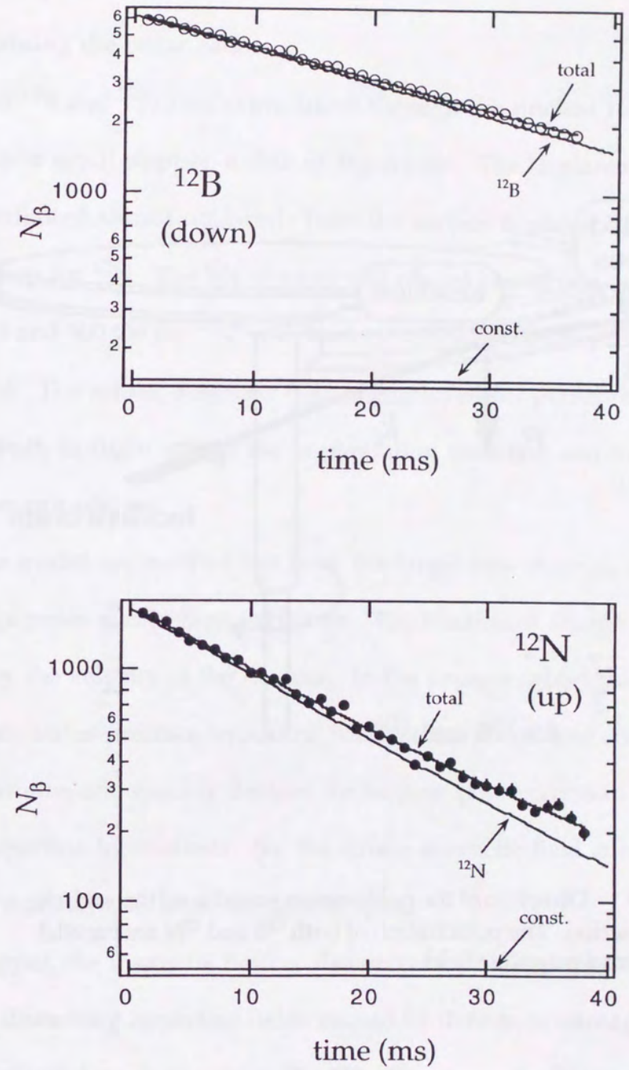

Figure 3.8 β-ray time spectra of the ^{12}B and ^{12}N. The decay of the ^{12}B and ^{12}N are clearly observed.

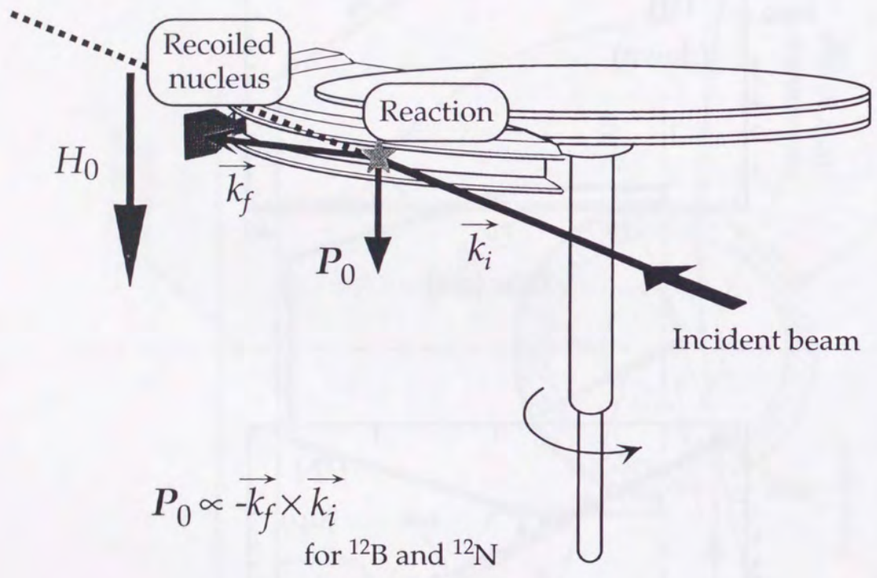

Figure 3.9 Direction of the polarization prouduced through the nuclear reaction. The polarization of both ^{12}B and ^{12}N are parallel to the external magnetic field.

3.3 Recoil implantation

3.3.1 Maintaining the polarization

The polarized ^{12}B and ^{12}N nuclei produced through the nuclear reaction were implanted into a recoil stopper, a disk of Mg crystal. The implantation depth in the crystal is distributed almost uniformly from the surface to about 1.5 μm deep for ^{12}B and 2.7 μm deep for ^{12}N. The Mg stopper was placed in a strong magnetic field H_0 = 300 Oe for ^{12}B and 600 Oe for ^{12}N, with the crystalline c-axis set parallel to the magnetic field. The strong magnetic field is employed for preserving the polarization both in flight and in the implantation medium, and to apply the NMR for the spin manipulation.

When the nuclei are recoiled out from the target into vacuum, they are in various charge states and in high excitation. The fraction of charge states is determined by the velocity of the nucleus. In the present case, 1^+ state is dominant. Various atomic states produce hyperfine fields at the position of the nucleus with various magnitude, and quickly destroy the nuclear polarization in flight because of the atomic hyperfine interactions. So, the strong magnetic field is necessary to decouple the nuclear spin from the atomic spin.

In the stopper, the magnetic field is also necessary to decouple the nuclear spin from various disturbing hyperfine fields caused by defects or damages on the site where the implanted nucleus resides [TA77]. The magnetic interaction of the nuclear magnetic moment with the field is superposed on the quadrupole interaction and is also used to carry out NMR.

3.3.2 Hyperfine interactions of ^{12}B and ^{12}N in a Mg crystal

The hyperfine interactions of ^{12}B and ^{12}N in Mg have been studied by means of the β-NMR technique in order to refine the spin manipulation technique necessary for the artificial conversion of the polarization to the alignment. A Mg single crystal has hexagonal closed packing (hcp) structure, and is presumed to have an electric field gradient parallel to the crystalline c-axis because of its crystal structure, as shown in Figure 3.10. The implanted nuclei, ^{12}B and ^{12}N nuclei, interact with the electric field gradient q in Mg, superimposed on the external magnetic field H_0. The interaction Hamiltonian is described as follows,

$$H_I = H_M + H_Q, \tag{3.3}$$

where

$$H_M = -\mu H_0, \tag{3.4}$$

$$H_Q = \frac{eqQ}{4I(2I-1)}\left\{3I_Z^2 - I(I+1) + \frac{\eta}{2}(I_+^2 + I_-^2)\right\}. \tag{3.5}$$

Here, μ and Q are the nuclear magnetic and quadrupole moment, respectively. I is the spin of implanted nucleus, and I_+ and I_- are the creation and annihilation operators, respectively. The electric field gradient is generally defined as

$$V_{ij} = \frac{d^2V}{dX_i dX_j}. \tag{3.6}$$

For ^{12}B (^{12}N) nuclei in a Mg crystal, the electric field gradient is presumed to be symmetric around the crystalline c-axis, so the asymmetry parameter η of the field gradient is zero;

$$\eta = \frac{V_{XX} - V_{YY}}{V_{ZZ}} = 0. \tag{3.7}$$

The Z-component is defined as $q = V_{ZZ}$. In the first-order perturbation calculation,

the energy levels E_m are unequally split caused by the quadrupole interaction H_Q as

$$E_m = -h\nu_L m + \frac{\nu_Q}{6}\left(\frac{3\cos^2\beta}{2} + \eta\sin^2\beta\cos 2\gamma\right)\left\{3m^2 - I(I+1)\right\}, \tag{3.8}$$

where ν_L and ν_Q are the Larmor frequency and the quadrupole coupling constant, $\nu_Q = 3eqQ/2$, and β and γ are the polar angles of the crystal. According to the eq. (3.8), Larmor frequency of the implanted nucleus is split into two separate frequencies in the case of $I = 1$, as shown in Figure 3.11.

The quadrupole coupling constant eqQ/h has been already measured with good precision to be -47.0 ± 0.1 kHz for the case of ^{12}B in Mg and -59.3 ± 1.7 kHz for the case of ^{12}N [KI90]. Since the c-axis of the Mg crystal was placed parallel to the external magnetic field, $\beta = 0°$, in the present experiment, the quadrupole splitting corresponds to $3eqQ/2$. The implantation site of ^{12}N in Mg was determined to be trigonal with lattice relaxation of $\Delta a/a = 15 \pm 5$ %, a being the lattice constant, as is shown in Figure 3.10. It has been identified from the angular dependence of the dipolar broadening of the resonance width for the double quantum transition, $m = -1 \leftrightarrow +1$. From the quadrupole moment of ^{12}N measured recently, $Q = 9.5 \pm 0.8$ mb [MI98], the electric field gradient at N site was derived experimentally to be $q = (-2.58 \pm 0.23) \times 10^{20}$ V/m^2. Both the electric field gradient and the implantation site are accounted for by the first-principle band calculation in the framework of the KKR method. According to this prediction, the total energy has the minimum at the trigonal site with the lattice relaxation of $\Delta a/a = 17$ %, and the electric field gradient $q = -1.92 \times 10^{20}$ V/m^2 are derived [OH93].

Recently, however, other minor locations of ^{12}B and ^{12}N nuclei in Mg have been found from the β-NMR studies, as shown in Figure 3.12 (a) [KI90][YA96]. Typical β-NMR spectra obtained by the single quantum transition is shown in Figure 3.12 (a),

and two pairs of resonances are clearly observed for both ^{12}B and ^{12}N. The major component with 85 % fraction has an electric field gradient parallel to the crystalline c-axis, that is well reproduced by the KKR band calculation. The residual component is clearly observed at exactly a half of the eqQ splitting for the main component. From this fact, it is suggested that the minority component comes from the micro grains whose c-axis is aligned in the plane perpendicular to the original c-axis, to give a half of eqQ splitting for the main component.

For advanced β-NMR studies of this second component, we have further developed the β-NMR method to measure the quadrupole splittings precisely. The modified β-NMR method, β-NQR, applies a set of AFP rf-fields to the resonance frequencies sequentially and inverts the initial spin ensemble completely. Figure 3.12 (b) and (c) show typical β-NQR spectra for ^{12}B and ^{12}N, respectively. The details of this technique are described in the appendixes. Using this method which can detect small polarization-change much effectively, the angular dependence of the quadrupole splitting of the second component was measured to confirm the above speculation. As a result, it has a large fraction (15 %) of the electric field gradient was found indeed to be perpendicular to the crystalline c-axis [YA96]. So, the second component was caused by micro grains in which c-axis grew perpendicular to the original c-axis, originating from defects of some kinds, which is easily introduced in the process of the crystal growth, or the cutting and treatment of the sample in preparation of the stopper. The detailed mechanism to produce an unique electric field gradient should be further investigated. In the actual experiment, we established the machining process which is free from such grains with disturbing second site. Also, even if any second site exists, the improved spin manipulation can reject completely the effect from the second site.

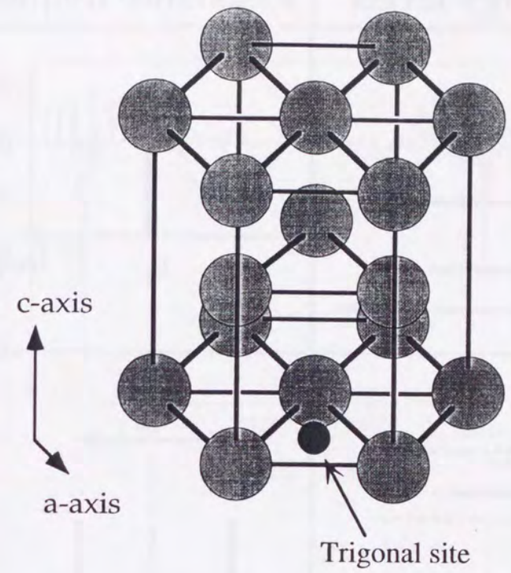

Figure 3.10 Crystal structure of Mg (hcp). The trigonal site is shown by the closed circle where ^{12}N is implanted.

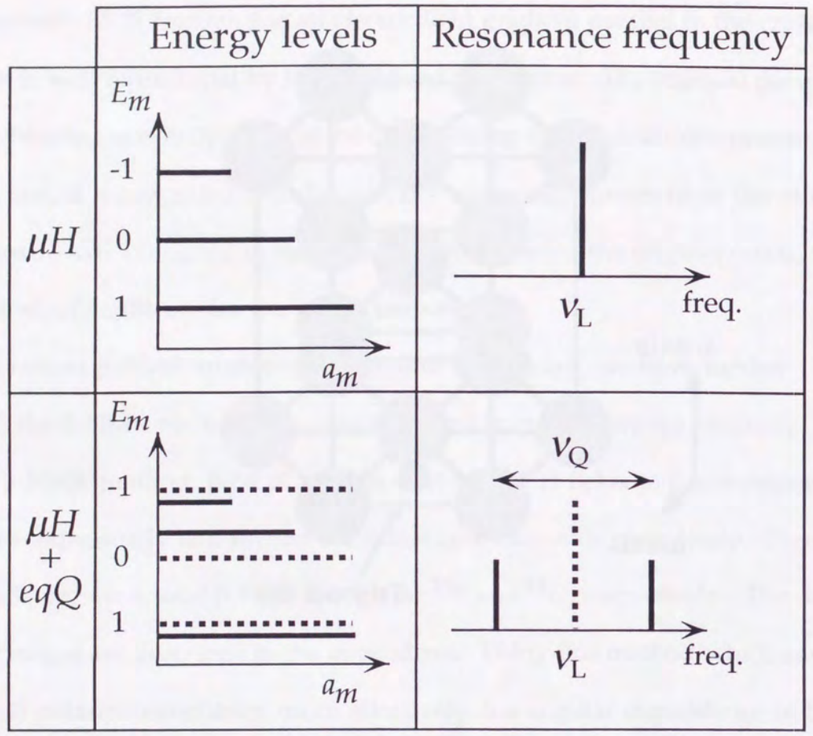

initial polarization	$P_0 > 0$
initial alignment	$A_0 > 0$
magnetic moment	$\mu > 0$
quadrupole coupling constant	$eqQ < 0$
EFG orientation	$\beta = 0^\circ$

Figure 3.11 Energy levels and frequency split caused by the magnetic and the quadrupole interaction in the stopper, where the above conditions are considered.

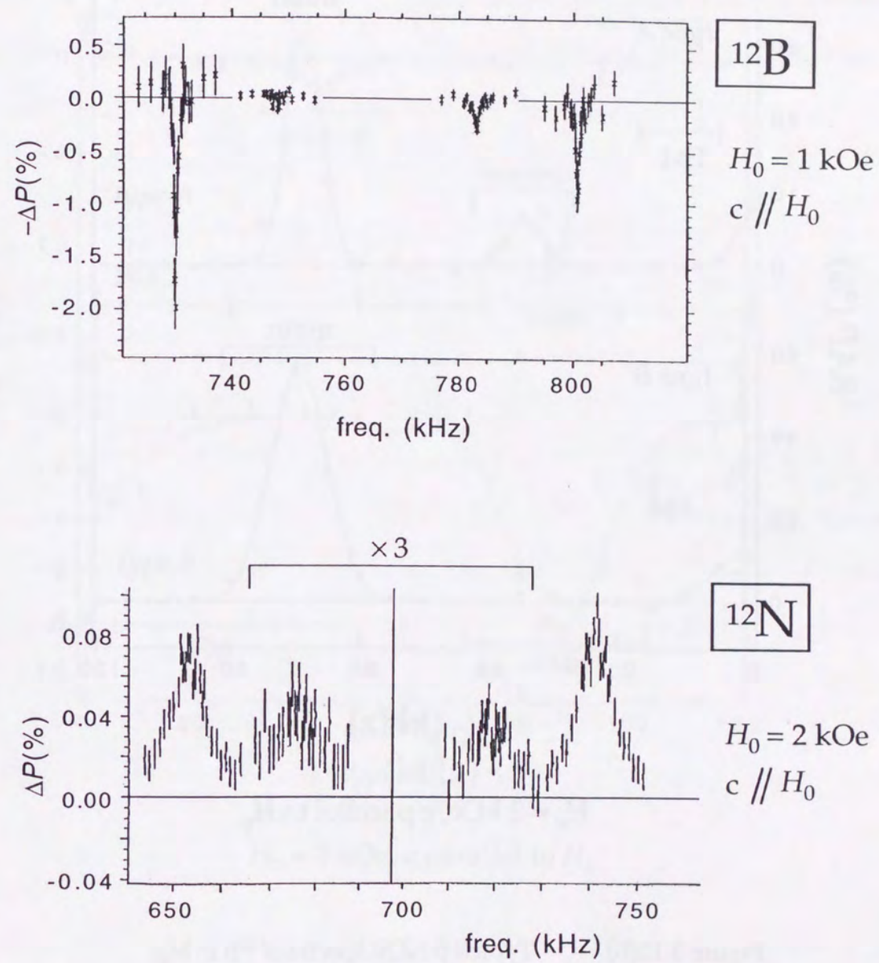

Figure 3.12(a) Typical NMR spectra of ^{12}B and ^{12}N in Mg [KI90]. The c-axis of Mg was set parallel to the external magnetic field. Two pairs of resonances are clearly shown in the both spectra, which correspond to the main and second sites. The vertical axis shows the polarization-change induced by the single rf, and the horizontal axis shows the frequency of the rf. For the spectrum of ^{12}N, a pair of peaks for the second site are three times multiplied.

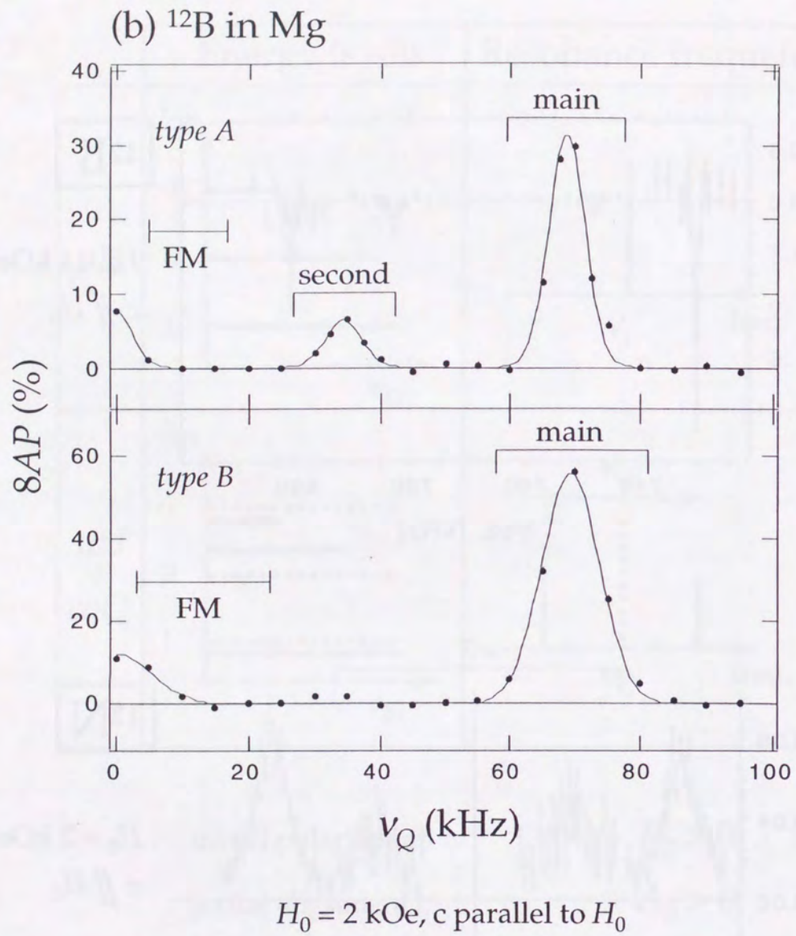

Figure 3.12(b) Typical β-NQR spectra of ^{12}B in Mg. The polarization-changes by the AFP techniquewere shown as a function of the quadrupole coupling constant. Two peaks of the main and second sites are seen in the sample A in the upper figure, but the second site is not seen in the sample B in the lower figure. The treatment of the sample is different between these two spectra. In the present experiment, the sample B was mainly used for the measurement of the alignment correlation terms. The peaks observed at $\nu_Q = 0$ are caused by the double quantum transition.

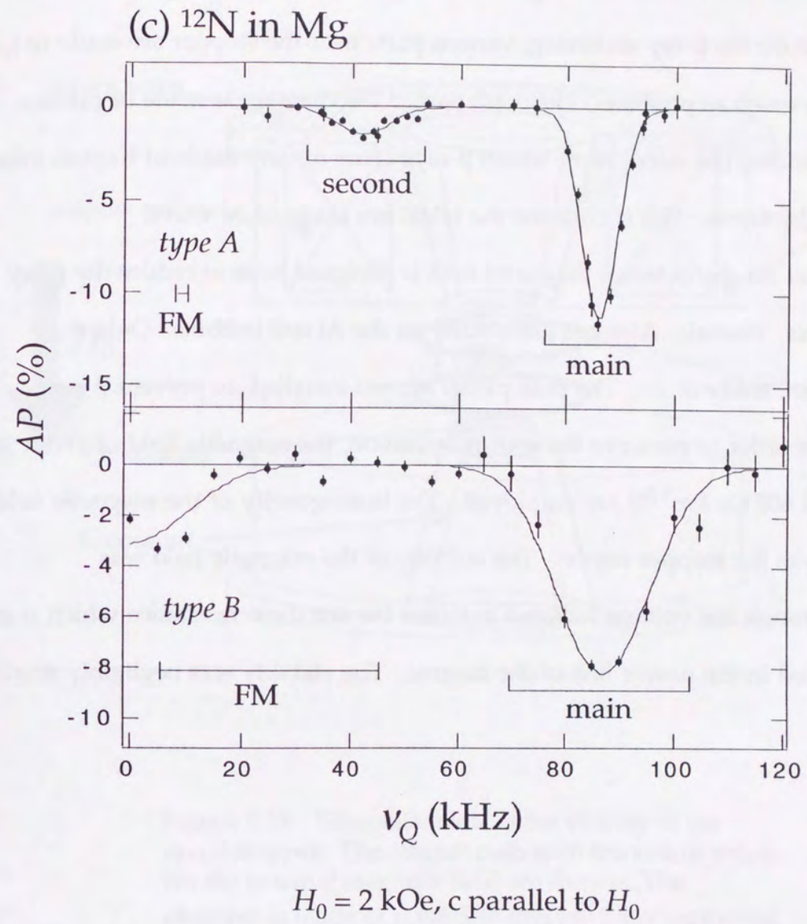

Figure 3.12(c) Typical β-NQR spectra of ^{12}N in Mg. The experimental conditions are the same as Figure 3.12(b).

3.3.3 Reaction chamber and magnet

The reaction chamber is shown in Figure 3.13, together with the magnet for NMR. In order to reduce the β-ray scattering, various parts near the stopper are made of low Z materials as much as possible. The main part of the chamber is made of plastics. The β-ray windows (20 mmϕ) from which β-rays come out are made of Kapton foils with 100 μm thickness. The rf coils for the NMR are made of Al wires.

The magnet for the external magnetic field is designed so as to reduce the β-ray scattering effect. Namely, Al wires are wound on the Al coil bobbins. Only the return yokes are made of Fe. The pole pieces are not installed, to prevent β ray scatterings. In order to preserve the spin polarization, the magnetic field of about 300 Oe for ^{12}B and 600 Oe for ^{12}N are employed. The homogeneity of the magnetic field is around 2 % in the stopper region. The stability of the magnetic field was monitored through the voltage induced between the standard resistance which is in series connected in the power line of the magnet. The stability was negligibly small, less than 10^{-3}.

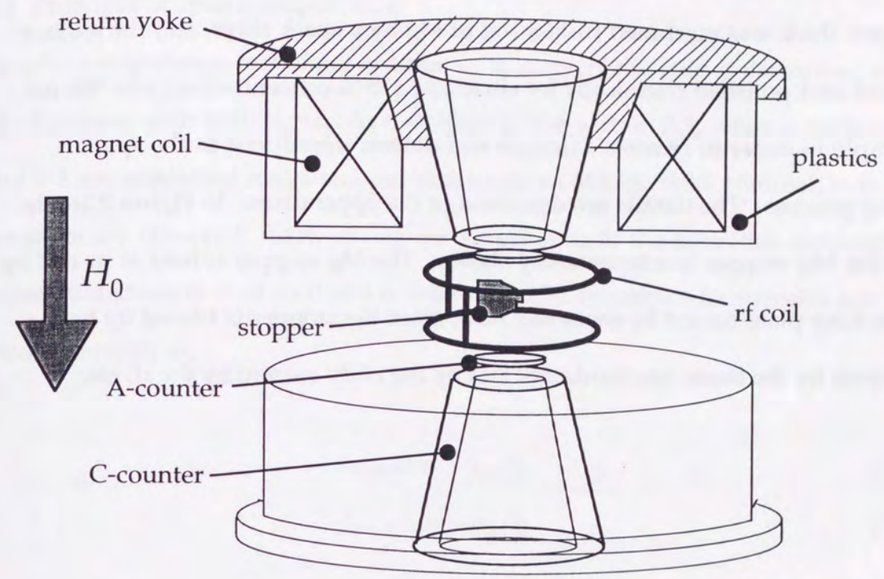

Figure 3.13 Schematic view of the vicinity of the recoil stopper. The magnet coils with the return yokes for the external magnetic field are shown. The chamber is made of plastics to prevent β-ray scattering. The C-counter of the cone shape also prevents the β-ray scattering caused by the magnet coil and the return yoke.

3.3.4 Implantation medium - Recoil stopper -

A Mg single crystal was used for the stopper, the structure of which is shown in Figure 3.10. In the present experiment, the Mg sample with the size of 12×16 mm^2 and 500 μm thick was machined from a rod of Mg by a spark slicer, and the surface was etched and polished chemically by citric acid (10 % concentration) into 300 μm thick sample in order to remove damages and defects introduced in the spark machining process. The details are described in the appendixes. In Figure 3.16, the setup of the Mg stopper is schematically shown. The Mg stopper is held at its end by the Al backing plate cooled by the water flow, since the stopper is heated up by the target ribbon by the beam bombardment and by the eddy current by the rf, etc.

3.4 Spin manipulation technique

3.4.1 Principle of spin manipulation

The spin manipulation technique enables us to convert the spin polarization to the spin alignment with both signs. As described in the section 3.3, when a nucleus with spin $I = 1$ are implanted into a stopper which has an electric field gradient, two resonances are observed. Each resonance corresponds to the transition between the magnetic substates $m = +1 \leftrightarrow 0$ and $m = 0 \leftrightarrow -1$. The resonance frequencies are explicitly written as,

$$f_{1\leftrightarrow 0} = \nu_L - \nu_Q/2, \tag{3.9}$$

$$f_{0\leftrightarrow -1} = \nu_L + \nu_Q/2, \tag{3.10}$$

where the definition of ν_L and ν_Q are the same as the eq. (3.8) in the section 3.3. For the main component of ^{12}B and ^{12}N nuclei in Mg, the resonances and energy levels are shown in Figure 3.11, under the present condition listed in Table. 3.2, so that, the transitions $m = -1 \leftrightarrow 0$ and $m = 0 \leftrightarrow +1$ correspond to the low frequency (LF) and the high frequency (HF), respectively. Here, the following conditions were considered, that is, the direction of the polarization relative to the magnetic field, the sign of the g-factor and the quadrupole coupling constant eqQ, and the direction of the electric field gradient relative to the magnetic field.

Applying a set of rf fields to the separate transition frequencies, the magnetic substate populations are manipulated. This is realized by two types of rf fields, the one for the depolarization method and the other for the AFP method. The depolarization rf-field equalizes neighboring magnetic substate populations, and the

AFP rf-field interchanges them. The details of NMR technique are described in the appendixes.

The way of creating the alignment is shown in Figure 3.14. For positive alignment, the substate populations between $m = 0$ and +1 are equalized by the depolarizing rf field with HF, and then those between $m = -1$ and 0 are interchanged by AFP rf field with LF. The pure positive alignment with no polarization is obtained at this stage for the measurement of the alignment correlation terms. Finally, the AFP field with LF is applied again and the alignment is converted back to the polarization, in order to check the relaxation of alignment during the measurement and to confirm the achievement of the spin manipulation. The polarization produced by the reaction is thus converted to the positive alignment, and converted back to the polarization. Similar manipulation is performed for negative alignment. The substate populations between $m = -1$ and 0 are equalized by depolarizing LF field and then those between $m = 0$ and +1 are interchanged by AFP HF field. Thus, both pure positive and negative alignment are created by the combination of AFP and depolarizing fields. In the case of perfect manipulation, the alignment to be created is described as

$$A^{\pm} = \pm\frac{3}{2}P_0 - \frac{1}{2}A_0, \tag{3.11}$$

where P_0 and A_0 are initial polarization and alignment, respectively, produced through the nuclear reaction. Therefore, the difference between positive and negative alignments is 3 times larger than the initial polarization directly produced through the nuclear reaction.

	^{12}B	^{12}N
I^{π}	1^+	1^+
Magnetic moment	$+1.00306(^{+15}_{-14})\mu_N$	$+0.4573(5)\ \mu_N$
Quadrupole moment	13.21 ± 0.26 mb	9.5 ± 0.8 mb
Stopper	Mg	Mg
Structure	hcp	hcp
Magnetic field H_0	300 Oe	600 Oe
eqQ/h (in Mg)	-47.0 ± 0.1 kHz	-59.3 ± 1.7 kHz
c-axis orientation	parallel to H_0	parallel to H_0
Polarization direction	parallel to H_0	parallel to H_0

Table 3.2 Experimental conditions for the spin manipulation.

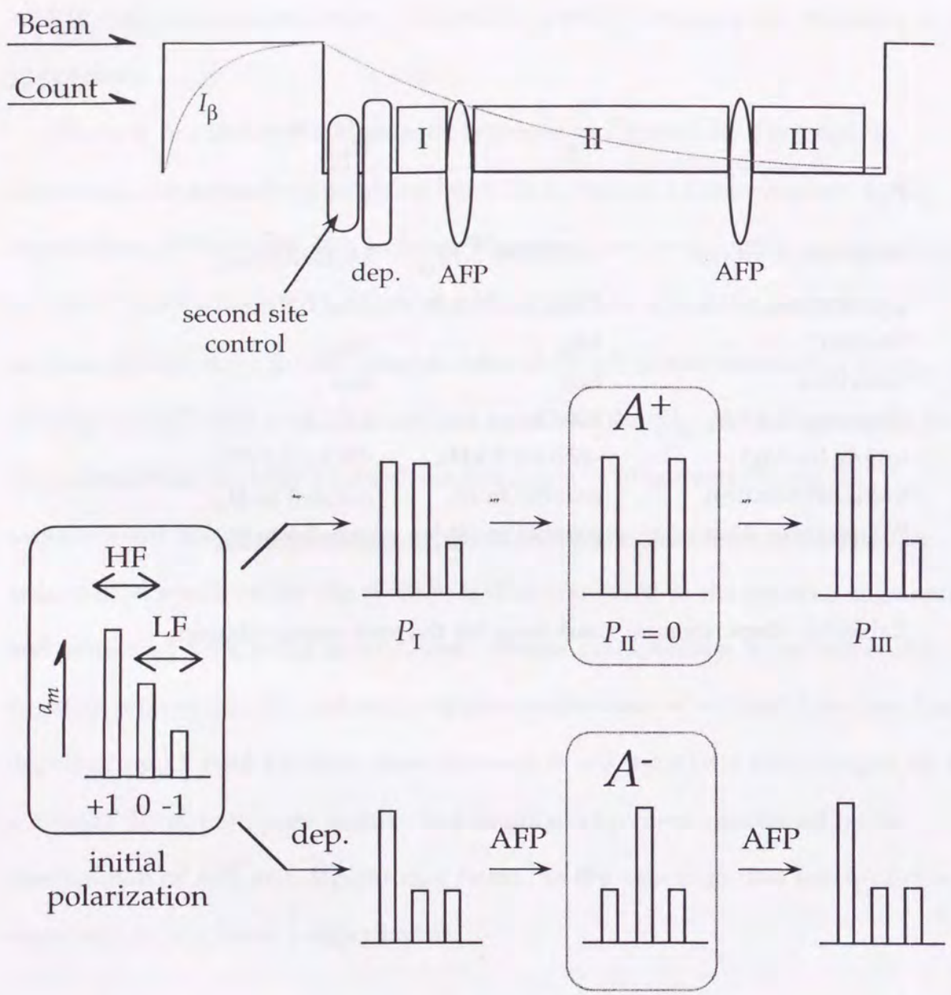

Figure 3.14 Spin manipulation for the creation of spin alignment from spin polarization. In the upper figure, timing sequence is shown. The alignments are created in the counting section II. The polarizations in I and III are used to calculate the created alignments. The cycles with the positive and negative alignments are alternatively repeated to accumulate enough counting statistics.

3.4.2 Improvements on the present spin manipulation

In the present experiment, the spin manipulation technique has been improved based on the knowledges of the hyperfine interactions of ^{12}B and ^{12}N in Mg single crystal. Since the crystalline c-axis of Mg was placed parallel to the external magnetic field, two pairs of resonances which come from the main and second component were completely separated. Thus, the spin manipulation on the main component does not disturb the spin ensemble for the second component. The residual polarization and alignment of the second component do not disturb the correlation measurement. However, for the completely reliable measurement the second component was depolarized before manipulating the main component. By this, the reliability of the spin manipulation was expected to be very much enhanced. The actual depolarization process of the second component is shown in Figure 3.15. The substate populations between m = 0 and +1 were interchanged by the AFP LF field, and then those between m = -1 and 0 were equalized by the depolarizing HF field. This manipulation is most efficient, since the most different substate populations are equalized by one rf field.

To make the spin manipulation more reliably, only the single quantum transitions, i.e. $m = -1 \leftrightarrow 0$ or $0 \leftrightarrow +1$, were used for the spin manipulation. Although the double quantum transition, $m = -1 \leftrightarrow +1$, is very efficient to invert the polarization, it induces the transitions of the second component at the same time because of the incomplete separation of the frequencies of the double quantum transition for the main and second component. In the previous experiments, the double quantum transition was used to check the geometrical asymmetry by inverting the polarization. The geometrical asymmetry in the counter telescopes is derived from this polarization-change, taking into account the degree of achievement of the AFP. The geometrical asymmetry is very important, since the

polarizations in the alignment cycles are determined based on the geometrical asymmetry. When the double quantum transition was applied, polarizations of the both components were inverted, so that the double quantum transition gives a false geometrical center for the main component. The true standard of the geometrical asymmetry is derived only when the polarization of the main component is inverted by the sequential single quantum transitions, which was completely accomplished in the present experiment.

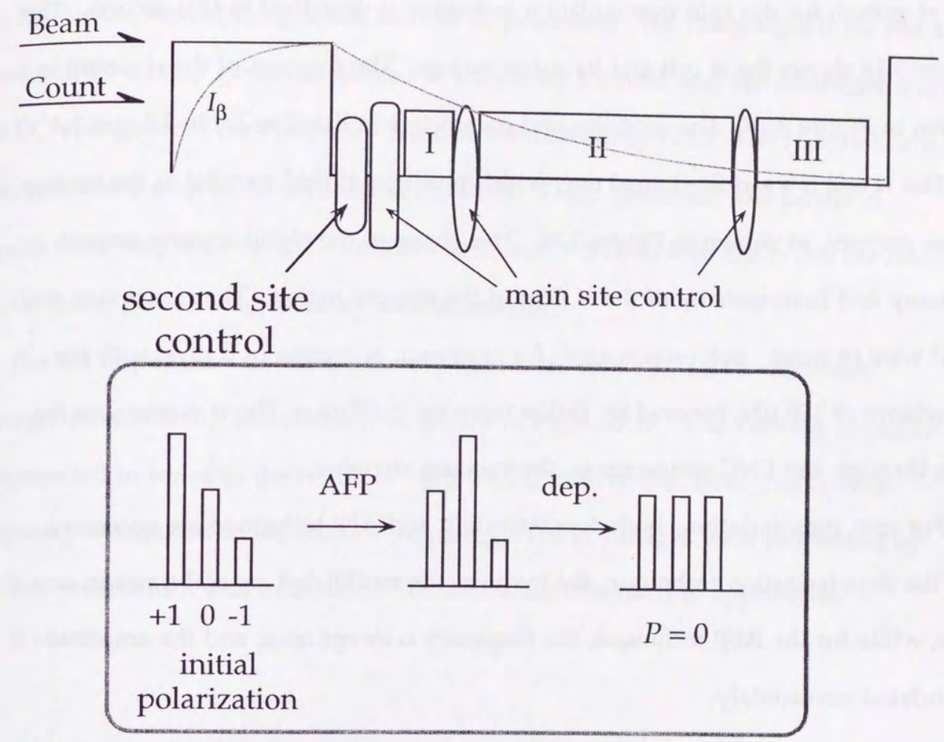

Figure 3.15 Spin manipulation for the second site.
In the upper figure, timing sequence is shown. The polarization of the second site was always destroyed before the spin manipulation of the main one.

3.4.3 Rf coil and amplifiers

The rf system for the spin manipulation technique is described in this section. The Figure 3.16 shows the rf coil and its surroundings. The diagram of the rf circuit is shown in Figure 3.17. The modules and parameters in listed in Table 3.3 and 3.4.

The rf coil is a saddle-shaped one, which produces rf field parallel to the surface of the stopper, as shown in Figure 3.16. This shape of the rf-coil ensures enough intensity and homogeneity of the rf field in the stopper region. The rf coil was made of Al wire (6 mmϕ , polyester coated) for minimum scattering of β rays, with the inductance of 100 μH, covered by Teflon tapes for insulation. The rf power was fed with through the BNC connector in the vacuum chamber.

For spin manipulation, both depolarization and AFP technique are necessary. For the depolarization technique, the frequency is modulated several times in one rf time, while for the AFP technique, the frequency is swept once, and the amplitude is modulated sinusoidaly.

Rf signals generated by an synthesizer are gated and processed by the signals from the supervising personal computer through the PIO control as shown in Figure 3.18. For AFP, three different of frequencies, LF and HF for the main component and LF for the second component, were applied. Frequency was controlled by DC voltage through VCO (Voltage Control Oscillator) input of the synthesizer. The Frequency Selector generates DC voltage corresponding to these 3 different frequencies, and the Frequency Control generates the ramp signals for FM. These two signals were combined by the HIZ mixer and fed to the VCO input. The output signals with FM were then amplitude-modulated sinusoidaly by one shot sine wave generated by the function generator with the RF-mixer. Finally, the rf signals are gated by the attenuated logic signals at the DBM (Double Balanced Mixer) for the complete isolation of the rf signals and to supply adequate power level for each rf.

For depolarization, three frequencies; LF and HF for the main component and the HF for the second component, have to be processed. The ramp signals for FM are produced by a ramp generator instead of Frequency Control, and are combined with the DC voltage from the Frequency Selector before feeding VCO. The rf signals are then gated and amplitude-adjusted at the DBM. These generated low power rf signals were amplified by the amplifiers 300L and A-1000 to feed the rf coil for NMR. The actual rf power is adjusted by an rf attenuator.

For the impedance matching, the rf power is fed to the LC series resonator through the matching transformer, as shown in Figure 3.19. The vacuum capacitor is connected in series to the rf coil to form the LC tank circuit, whose resonance frequency is adjusted to the Larmor frequency. The rf voltages were monitored by the test point which was calibrated. The details are described in appendixes.

List of Modules	
rf coil	saddle type
	Al wire (0.6 m mϕ polyester coated)
	$L = 100\ \mu H$
	$H_1 = 6.5\ Oe/A_{DC}$
PIO control	Adaptec AB98-04A
LA	OULNS Level Adapter 7971
Fan I/O	OULNS Logic Fan-IN Fan-OUT 7951
IG	OULNS Interval Generator 7975
Synthesizer	TAKEDARIKEN TR3133B
FG	NF Wide-Band Function Generator FG141
Dual Mixer	EG&G Dual Mixer AN308/NL
DBM	R&K Double Balanced Mixer M1CA
SUM&INVERT	ORTEC DUAL SUM AND INVERT 433A
300L	ENI RF POWER AMPLIFIER
M102L	RF POWER LABS, INC. WIDEBAND AMPLIFIER
A-1000	ENI RF POWER AMPLIFIER
Vacuum condenser	AMPEREX 50 ~ 1000 pF
Ferrite core	TOSHIBA M4B23

Table 3.3 List of modules used in the rf circuit.

AFP	^{12}B	^{12}N
H_1	5 ~ 7 Oe	5 ~ 7 Oe
T_{rf}	1 ms	1 ms
FM	± 15 kHz	± 15 kHz
dep		
H_1	5 ~ 8 Oe	5 ~ 8 Oe
T_{rf}	2 ms (8 sweeps)	2 ms (8 sweeps)
FM	± 10 kHz	± 10 kHz

Table 3.4 Rf conditions for making spin alignment.

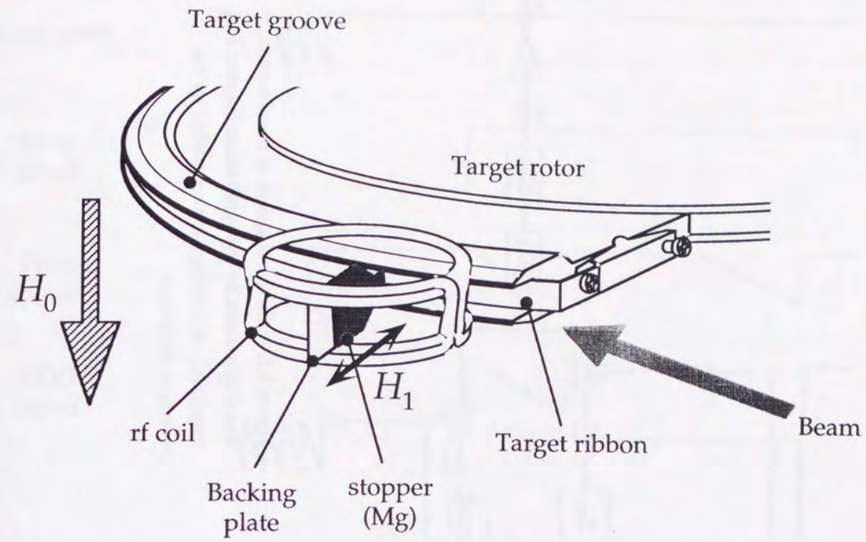

Figure 3.16 Schematic view of the stopper and rf coil. The recoiled nuclei produced by the nuclear reaction are implanted into the stopper which is held by the backing plate. The external magnetic field is applied parallel to the polarization.

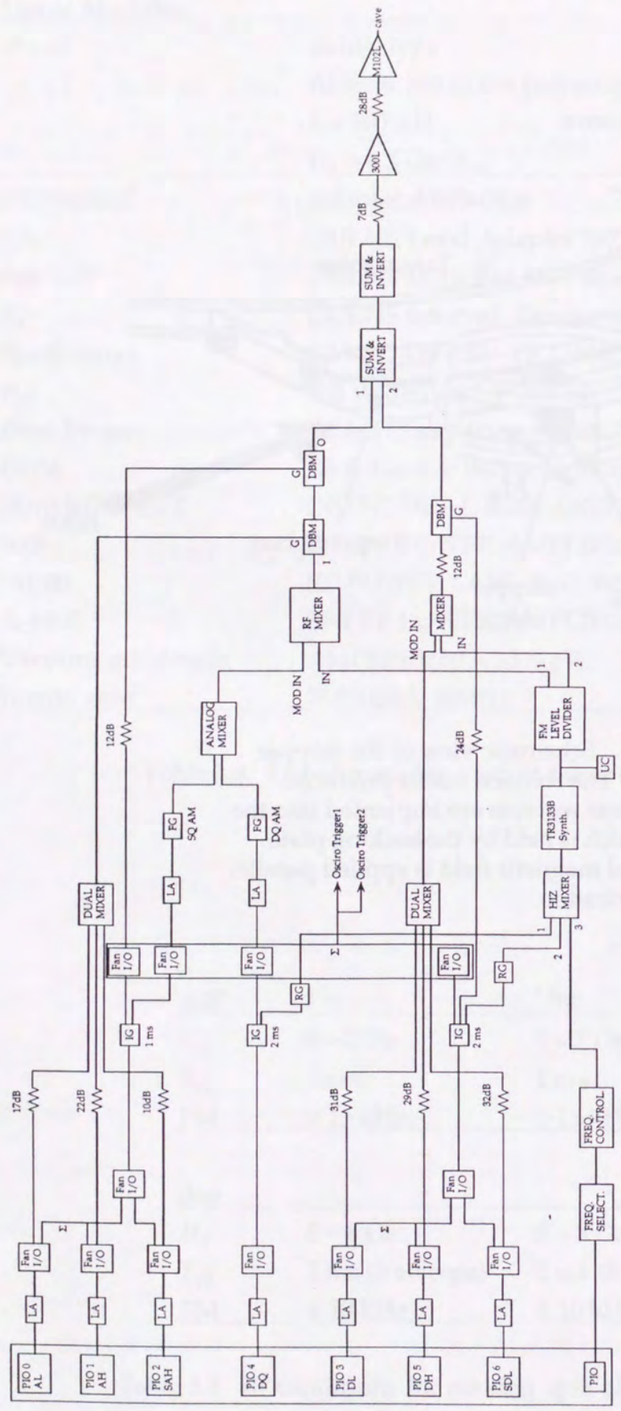

Figure 3.17 Circuit diagram of the rf control. The rf generated by the synthesizer is gated and amplified. All timings are controlled by the personal computer.

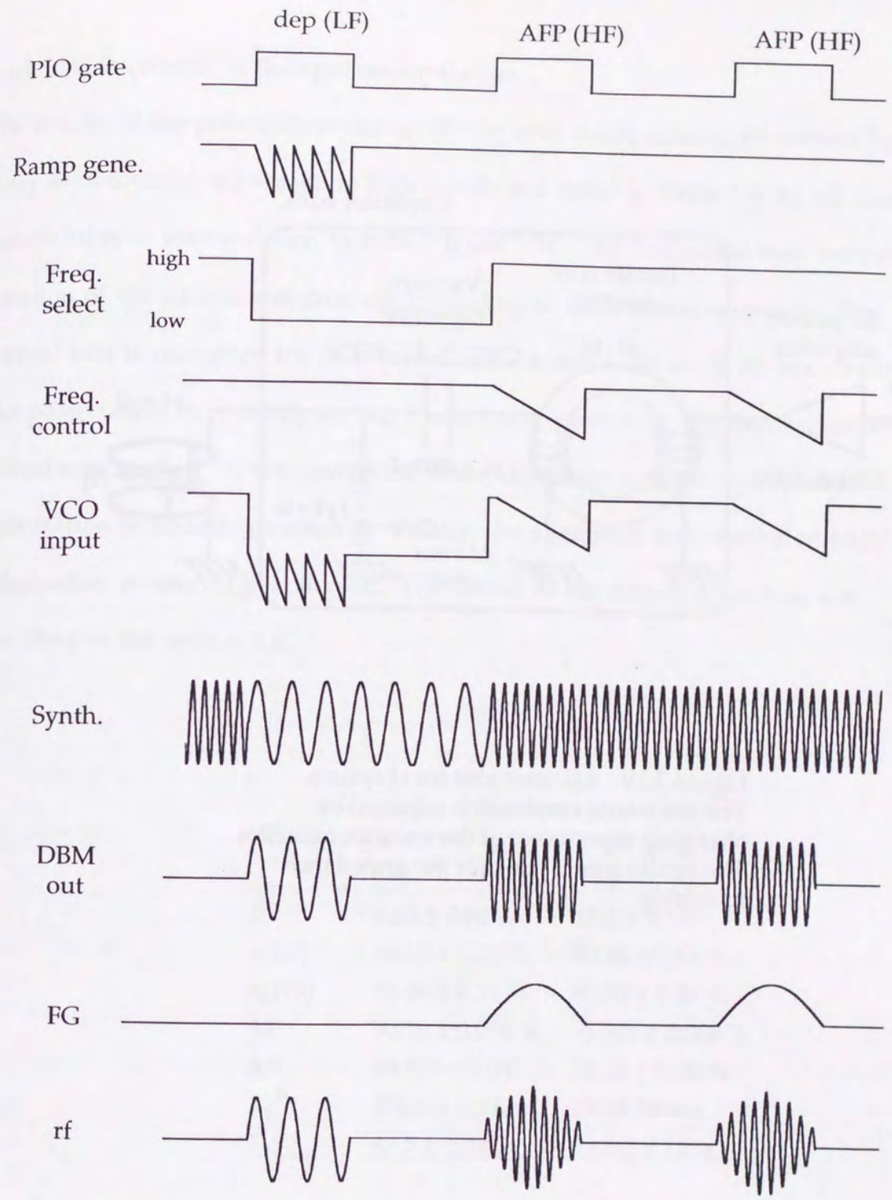

Figure 3.18 Timing sequence anf rf signals in the rf control circuit. The ramp signals which are fed to VCO are generated by Ramp generator, Frequency selector, and Frequency control. The rf signals with FM are gated by DBM, and are amplitude-modulated in the case of AFP.

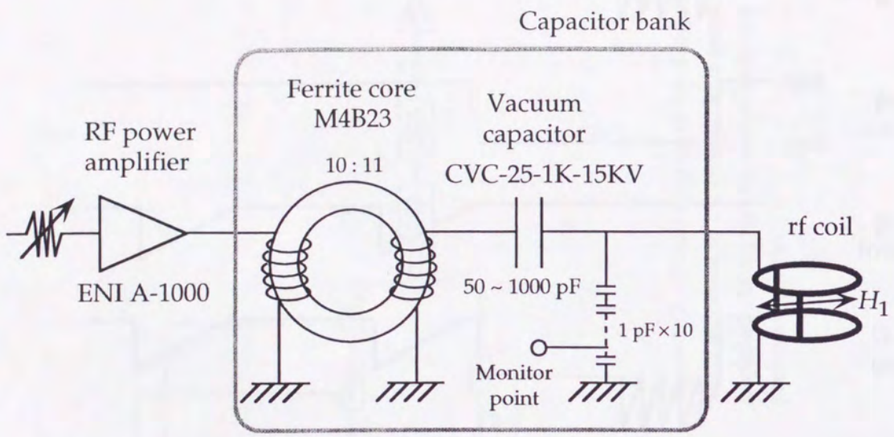

Figure 3.19 LC resonator for rf system.
The resonance condition is adjusted by changing capacitance of the vacuum capacitor. The ferrite core is used for the impedance matching.

3.4.4 Achievement of the spin manipulation

The results of the polarization-change by the spin manipulation, monitored by the β-ray asymmetries, are shown in Figure 3.20, and listed in Table 3.5, which shows successful spin manipulation in both ^{12}B and ^{12}N. The horizontal bars indicate time duration of the counting section corresponding to each timing sequence. The vertical axis is change of the polarization determined from the β-ray asymmetry. The polarization in counting-section I was the one just after the depolarization rf-field was applied. It was converted to the alignment with negligibly small polarization in counting-section II. Finally, the alignment was converted back to the polarization in counting-section III. The details of the timing sequences are described in the section 3.6.

	^{12}B	^{12}N
P	9.03 ± 0.02 %	19.2 ± 0.1 %
η(LF)	98.61 ± 0.29 %	99.46 ± 0.61 %
η(HF)	98.64 ± 0.21 %	99.82 ± 0.51 %
ΔP	0.019 ± 0.013 %	-0.347 ± 0.080 %
ΔA	20.859 ± 0.047 %	52.28 ± 0.30 %
T_1^P	166.6 ± 3.3 ms	292 ± 28 ms
T_1^A	47.5 ± 1.0 ms	99.5 ± 9.1 ms

Table 3.5 Spin alignments obtained by the spin manipulation.

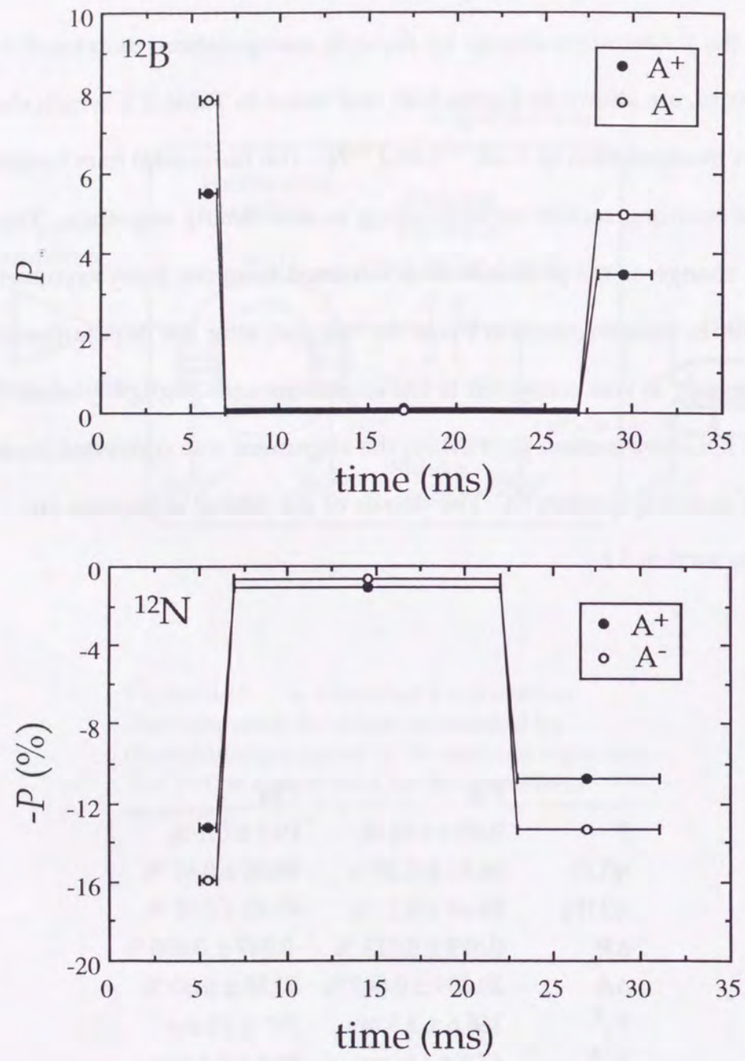

Figure 3.20 Polarization-change by the spin manipulation. The polarizations in the counting section I was converted to the alignment in II where the polarization vanished, and back to the polarizations in III. The difference of the polarizations between the counting section I and III is caused by imperfect spin manipulation and spin relaxation.

3.5 Detection of β rays

3.5.1 β ray detector

The β-rays were detected by two sets of plastic-scintillation-counter telescopes placed above and below the recoil stopper relative to the reaction plane. The β-ray counter telescope consists of four counters, A-, B-, $\overline{C}$-, and E-counters. The setup is shown in the Figure 3.21.

A-counters (12 m mϕ × 0.5 mmt) were placed just outside of the β-ray window of the stopper chamber. Their scintillation lights were guided through acryl light guide and fed to the PMT (Photo Multiplier Tube). The A-counters determine the solid angle with the B-counters (55 mmϕ × 1 mmt) and were also used to reject backscattered β-rays, which reduce the observed polarization. Backscattered β rays and cosmic rays were rejected by taking anticoincidence with the A-counter placed at the other side.

Cone-shaped $\overline{C}$-counters play a role of the active collimator to reject β rays scattered by the magnet, etc.. For uniform light collection efficiency, C-counters were seen by two photomultipliers through the fishtail-like light guides. The solid angle restricted by A-, B-, and $\overline{C}$-counter telescopes is cone region with the subtending angle of 28°. The detection efficiencies of counters are all more than 95 % except for the A-counters where efficiency is approximately 90 %.

To measure β-ray spectra, large cylindrical counters (152 m mϕ × 178 mmt) were used, which are mounted on the PMTs directly. In order to measure β-ray spectra precisely, the high stability is required for the detection system. Firstly, against the saturation of the PMT of the E-counters by the beam burst during the production time, the high voltage fed to the PMT was dropped during the production time not

to amplify photoelectrons, in order to prevent unwanted after effects in the β-ray counting time. Secondary, the gains of the E-counters were stabilized by the feedback system using the standard lights from the Light-Emitting-Diode (LED), which is embedded in a temperature controlled cell for high stability. The light pulses from the LED were fed to the head of the scintillators through optical fibers with a rate almost same as β-ray counting rate in the last section of the counting times, not to disturb β-ray countings.

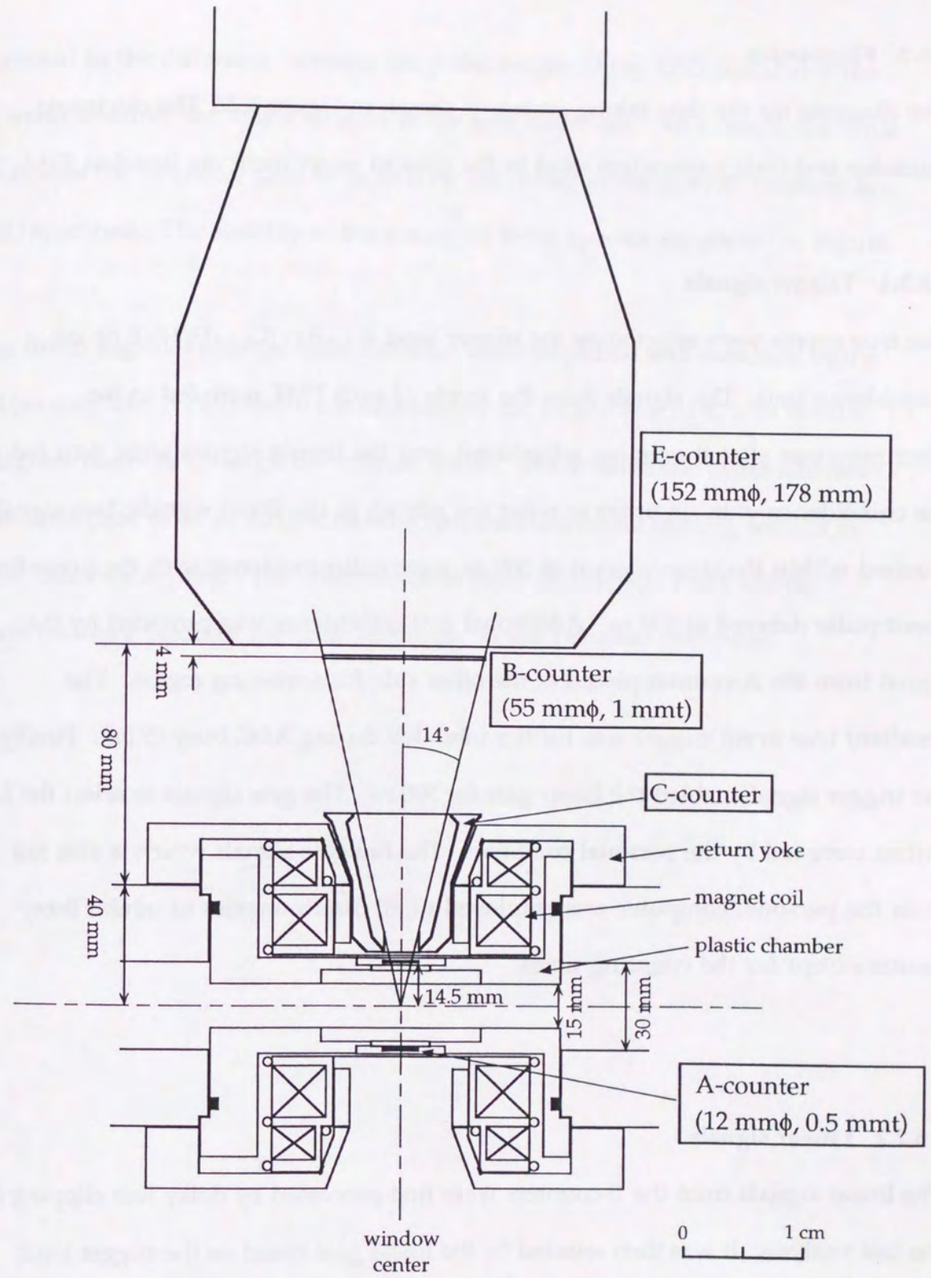

Figure 3.21 β-ray counter telescope (UP side).
A-, B-, C-, and E-counters consist of the counter telescope.
All detectors are plastic-scintillation counters. The geometrical condition for the counter telescope is shown.

3.5.2 Electronics

The diagram for the data taking system is shown in Figure 3.22. The electronic modules and their parameters used in the present experiment are listed in Table 3.6.

3.5.2.1 Trigger signals

The true events were selected by the trigger logic $A \cap B \cap (\overline{C_1} \cup \overline{C_2}) \cap E$ by the coincidence unit. The signals from the anode of each PMT were fed to the discriminators after the timing adjustment, and the timing signals were then fed to the coincidence unit. In order to reject the pile-up of the linear signals, two signals reached within the time interval of 500 ns were anticoincidence with the preceding event pulse delayed at 500 ns. Additional anti-coincidence was provided by the signal from the A-counter placed at the other side for scattering region. The resultant true event trigger was further inhibited during ADC busy (5 μs). Finally, the trigger signal enabled the linear gate for 500 ns. The gate signals to select the LED pulses were fed by the personal computer. The Bin gate signals which is also fed from the personal computer was employed to all discriminators to inhibit β-ray counts except for the counting times.

3.5.2.2 Linear signals

The linear signals from the E-counters were first processed by delay line clipping for the fast analysis. It was then selected by the linear gate based on the trigger logic mentioned above to reject all the unwanted signals. After amplified and shaped by the spectroscopy amplifier (SSA), the linear signals were fed to the gain stabilizer which controls overall gain of the amplifier system to give a standard pulse height for the LED light pulse. This was attained by the feedback loop where the error signal

proportional to the difference between the pulse height of the LED signal and the preset value controls the amplifier gain in the gain stabilizer. As a result, the error signal adjusts the amplifier gain so as to keep the center of the gravity constant for the LED spectrum. The stability of the gravity of β-ray spectra are shown in Figure 3.23.

The linear signals from the gain stabilizer were amplified and stretched by the gated bias amplifier (GBA) and were digitized by the ADC. The ADC sent the data to the histgram memory through the address shifter, which shifts the offset address of the spectrum data so as to accumulate the spectrum for each counting section in different memory regions. The spectrum data were finally read out from the histgram memory through the crate controller to the personal computer.

List of Modules

PM	A	Hamamatsu R329	HV = -2500 V
PM	B	Hamamatsu R329	HV = -2000 V
PM	C	Hamamatsu R329	HV = -2500 V
PM	E	Hamamatsu R1250	HV = -1600 V
Discriminator	A	LeCroy 821	thres. = -100 mV, wid. = 20 ns
Discriminator	B	LeCroy 821	thres. = -100 mV, wid. = 200 ns
Discriminator	E	LeCroy 821	thres. = -150 mV, wid. = 7 ns
Discriminator	C	EG&G T122/NL	thres. = -60 mV, wid. = 40 ns
OR C		EG&G T122/NL	
1st Coin.		ORTEC C314/NL	
2nd Coin.		ORTEC C314/NL	
TFA		ORTEC 454 gain 5, int 10, diff out	
Pileup Gate		EG&G GP100/NL 500 ns	
ADC busy		OULNS Gate Generator 7973 5 μs	
GDG		OULNS Gate&Delay Generator	
EF		OULNS Emitter Follower	
LG		ORTEC linear Gate LG101/NL	
SSA		ORTEC Spectroscopy Amplifier 452 shaping 0.5 μs, gain 500 × 5	
GS		Gain Stabilizer	
GBA		ORTEC Gated Bias Amplifier 444 bais 0, gain 5 × 8	
LGS		ORTEC Linear Gate Stretcher	
ADC		CANBERRA 8075 gain 256	
Address shifter		CI/LRS ADAPTER	
Histgram Memory		LeCroy 3588	
Crate Controller		TOYO CC7000	

Table 3.6 The modules and parameters used for the detection circuit.

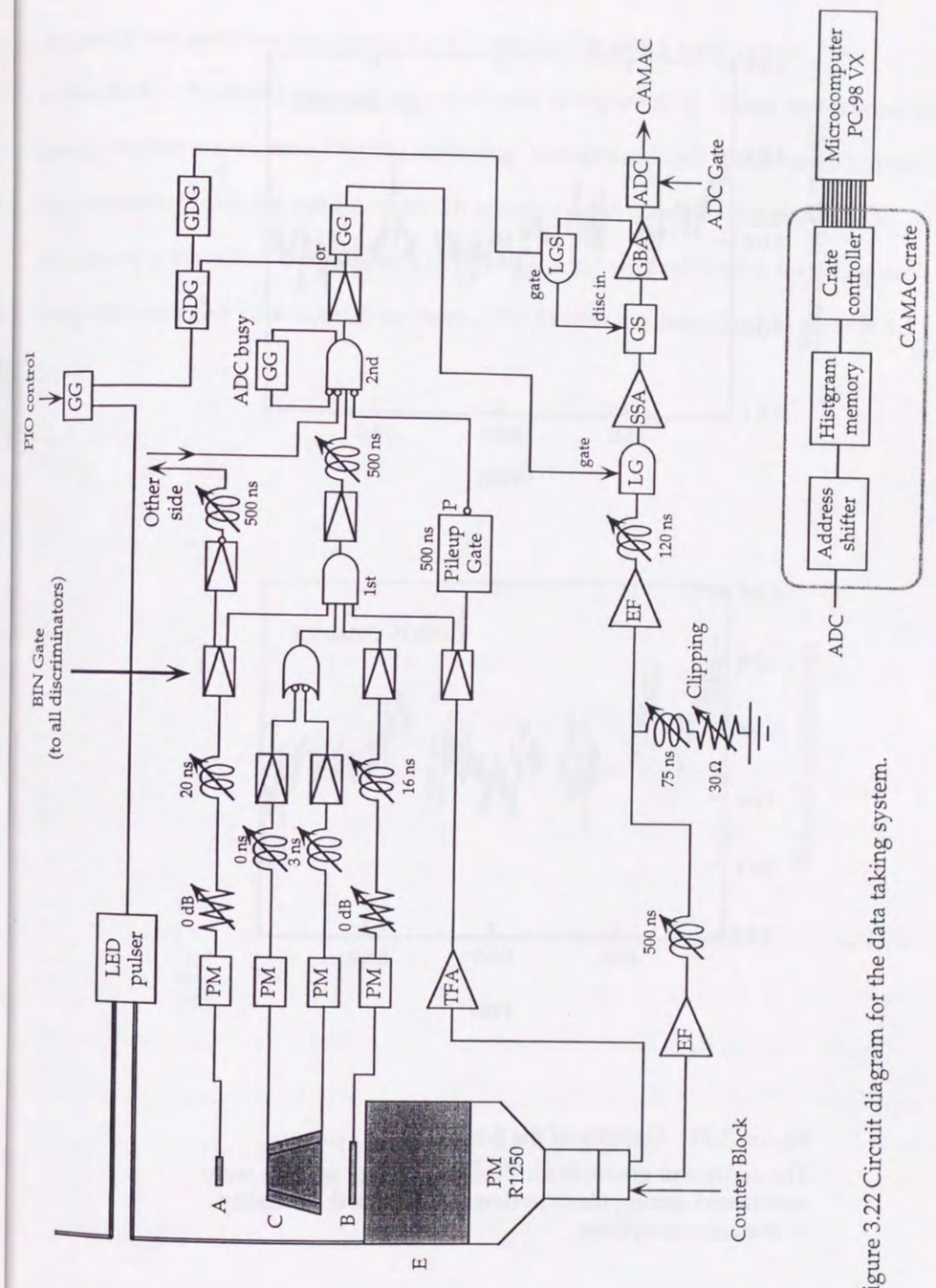

Figure 3.22 Circuit diagram for the data taking system.

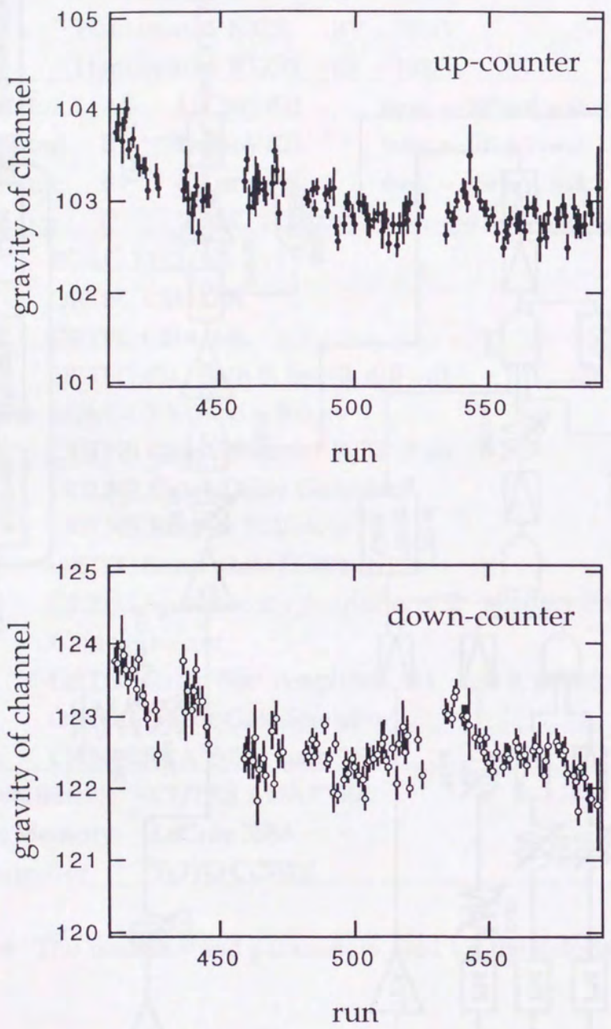

Figure 3.23 Stability of the β-ray counter system.
The centers of gravities for the β-ray energy spectra were monitored during the experiment, to check the stability of the counter system.

3.5.3 β ray energy spectra

Typical β-ray yields were about 1.5×10^3 cps for ^{12}B and 1×10^2 cps for ^{12}N, respectively. Typical β-ray spectra are shown in Figure 3.24. Some distortions in low energy region were caused by the scattering, background and disturbance effects in the magnetic field, the region of which was not used for determination of the alignment correlation coefficients. The energy scale was calibrated by using the endpoint energies of several β-emitters. The Details are described in section 4.1.

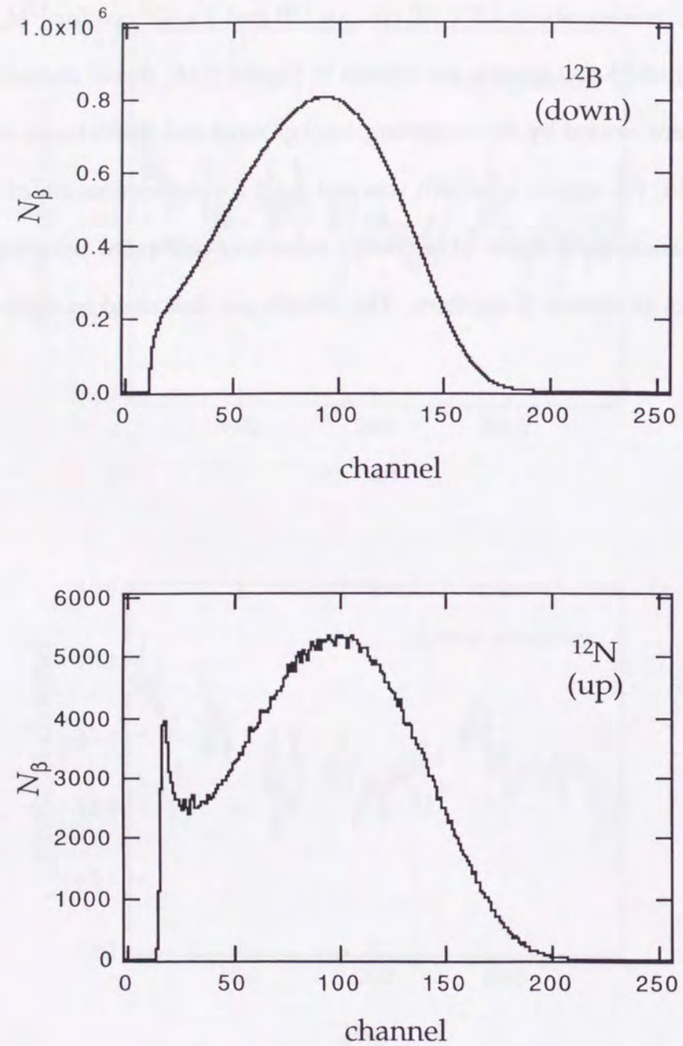

Figure 3.24 Typical β-ray energy spectra of ^{12}B and ^{12}N. Some distortions in the low energy are caused by the background and the β-ray scattering. The analysis was performed at 5 ~ 13 MeV where the distortion was not seen.

3.6 Experimental procedure and data acquisition

3.6.1 Experimental control and procedure

The diagram of the overall control system is shown in Figure 3.25. It consists of the rotating target system, rf system, and detectors. The every timing is synchronized by the timing sequences which is initiated by the target-in pulse from the timing pickup system. The target-in pulse triggers the beam bombardment on the target, and after the production time, the beam is stopped, and a set of rf fields are applied. The β rays are counted in the counting sections of the timing sequences. The whole system is supervised by the personal computer. The diagram of the control circuit is shown in Figure 3.26, together with the timing of the signals.

The experimental procedure is briefly described. Firstly, production of ^{12}B or ^{12}N was confirmed from the β-ray time spectra. Next, the resonances of ^{12}B or ^{12}N implanted in Mg were confirmed, which are split caused by the quadrupole interaction of the stopper Mg. Thirdly, The rf fields were adjusted so as to obtain optimum degrees for achievement of the AFP fields. Finally, the spin manipulation was performed to create the alignment, and the β-ray spectra were measured to get enough counting statistics. In the final step, two types of the timing sequence were alternatively repeated. One is the main sequence, in which the β-ray energy spectra from aligned nuclei were measured. The other is the test sequence, which was performed in order to confirm the degrees of achievement of the AFP field. The Details are described below.

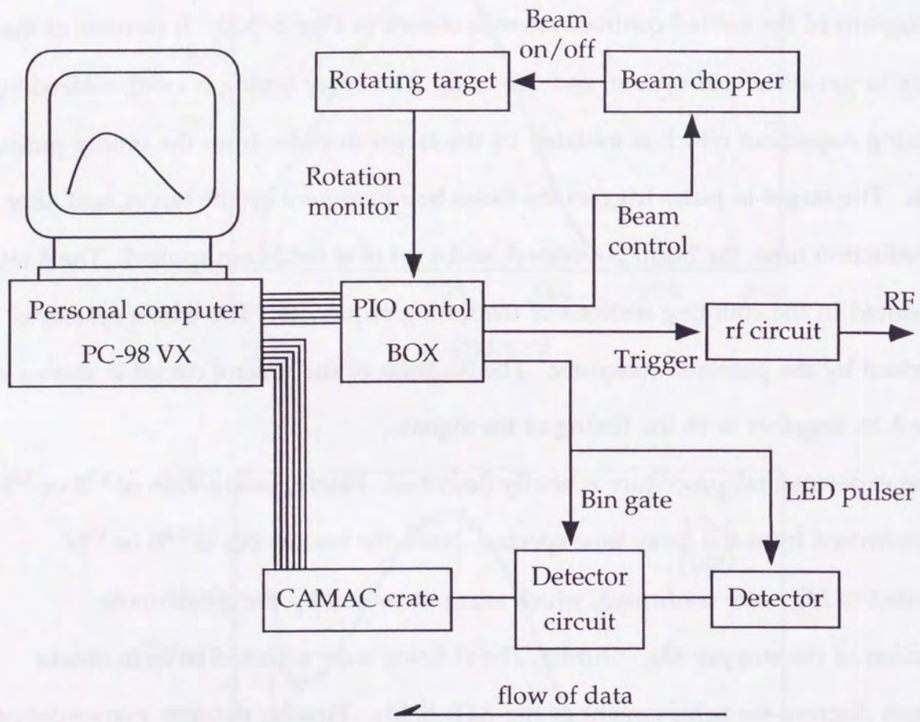

Figure 3.25 Diagram of the experimental control.
The beam control, rf timing and data taking are all controlled by the personal computer.

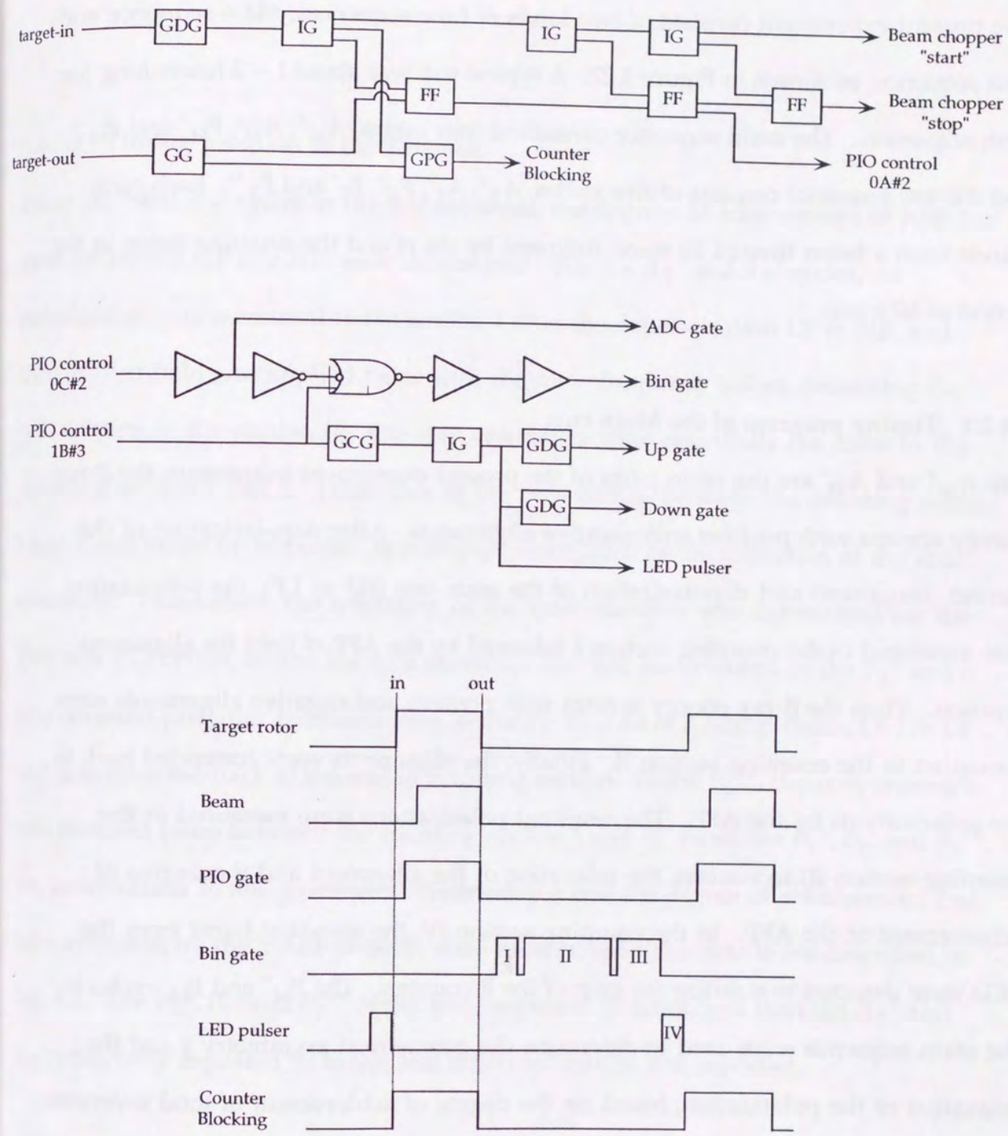

Figure 3.26 Schematic diagram and timings for the experimental control signals.
The upper figure shows the beam control diagram, and the middle figure shows the diagram which generates gate signals for detection circuit. Timings for the beam control and the gate signals for detector system are shown in the lower figure.

3.6.2 Timing programs of the data taking

The present experiment consists of two kinds of time sequences; Main sequence and Test sequence, as shown in Figure 3.27. A typical run was about 1 ~ 2 hours long for both sequences. The main sequence consists of four cycles, A_M^+, A_M^-, P_M^+ and P_M^-, and the test sequence consists of five cycles, A_T^+, A_T^-, P_T^+, P_T^- and P_T^{++}. Each cycle stands from a beam time of 20 msec, followed by the rf and the counting times in the period of 60 msec.

3.6.2.1 Timing program of the Main run

The A_M^+ and A_M^- are the main parts of the present experiment to measure the β-ray energy spectra with positive and negative alignments. After depolarization of the second component and depolarization of the main one (HF or LF), the polarization was measured in the counting section I followed by the AFP rf field for alignment creation. Then the β-ray energy spectra with positive and negative alignments were measured in the counting section II. Finally, the alignments were converted back to the polarizations by the AFP. The resultant polarizations were measured in the counting section III to confirm the relaxation of the alignment and the degree of achievement of the AFP. In the counting section IV, the standard lights from the LED were detected to stabilize the gain of the E-counters. The P_M^+ and P_M^- cycles in the main sequence were used to determine the geometrical asymmetry g and the relaxation of the polarization, based on the degree of achievement of total inversion by the 3 AFP rf-fields, LF-HF-LF, derived from the test sequence. Using the geometrical asymmetry g from the P_M^+ and P_M^- cycles, the polarizations in the counting section I, II and III in the A_M^+ and A_M^- were calculated. They were used to calculate the alignment in the counting section II. Five sets of P_M^+ and P_M^- cycles were followed by 20 sets of the A_M^+ and A_M^- and these sets were repeated

alternatively until necessary counting statistics were accumulated.

3.6.2.2 Timing program of the Test run

From A_T^+ and A_T^- cycles in the test sequence, the degrees of achievement of AFP for each frequency, LF and HF, were determined. For the A_T^+ and A_T^- cycles, the polarization was measured in the section I after the depolarization LF or HF, and then AFP rf field was applied twice with the same frequency before measuring the polarization in the section II. The spin ensembles were essentially the same in the counting section I and II. Difference of the polarization between the counting section I and II are cause by imperfect spin manipulation and/or the relaxation of the spin ensemble. Meanwhile, the relaxation of the spin ensemble was determined for the PT+ and PT- cycles, where the spin ensemble was not manipulated in the P_T^+ and it was inverted just after the beam time in the P_T^- by a set of 3 AFP rf-fields, LF-HF-LF and was inverted back at the end of counting section. In the P_T^{++}, the spin ensemble was inverted twice between the counting section I and II. From the P_T^+, P_T^- and P_T^{++}, the polarization $\boldsymbol{P}$, the geometrical asymmetry g and the degree of achievement ξ of total inversion by the 3 AFP rf-fields were determined. The details are described in Sec. 4.2. The P_T^+, P_T^- and P_T^{++} cycles were repeated 10 times, and then the A_T^+ and A_T^- cycles were repeated 10 times, and this combination was repeated.

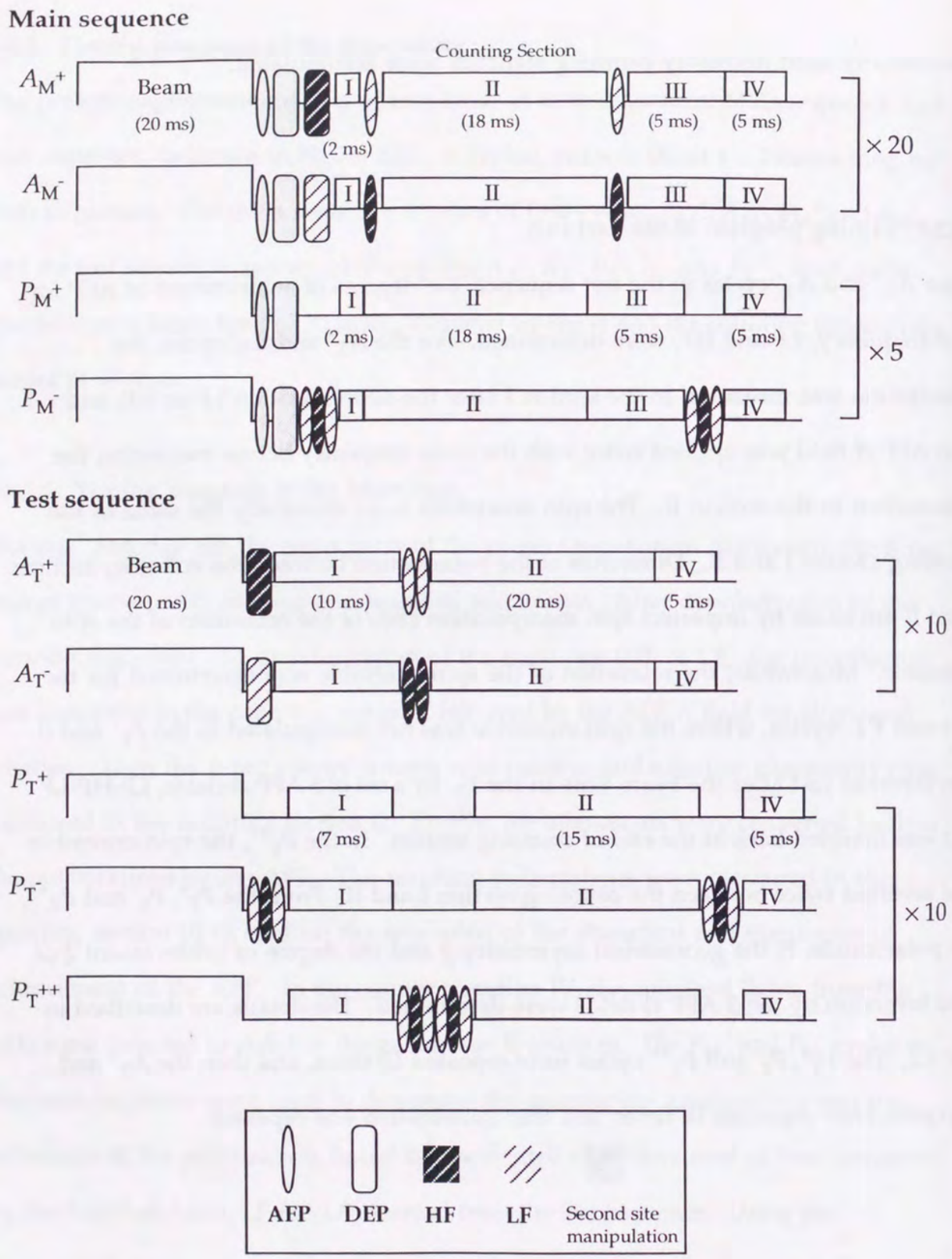

Figure 3.27 Timing sequence for the present experiment.
All cycles are repeated alternatively. The time scales are shown in the figures.

Chapter 4

Data analysis

4.1 Energy calibration

4.1.1 β-ray counter response and spectrum

To know the energy scales in β-ray energy spectra is very important to extract the alignment correlation coefficients, since the alignment correlation term is proportional to the β-ray energy. The energy calibration was performed by measuring β-ray energy spectra from several β-emitters. Since β-ray energy spectrum is the continuous one, endpoint channels corresponding to the β-ray endpoint energies were plotted against energies for several β-emitters. For the analysis process, it is necessary to know the shape of the energy spectrum to be detected by the actual detector. The β-ray energy spectrum is described as

$$W(E) \propto pE(E_0 - E)^2 F(\pm Z, E)\{1 + R(E, E_0)\}C(E), \tag{4.1}$$

where $F(\pm Z, E)$, $R(E, E_0)$, and $C(E)$ are Fermi function, radiative correction and spectral shape factor, respectively. The shape factor is described as

$$C(E) = 1 \pm (8/3)aE. \tag{4.2}$$

Here, a is the weak magnetism term. For the purpose of the energy calibration, small terms such as the shape factor and correlation terms were neglected.

To analyze the actual energy spectra, counter response has to be considered, because the total energy of a β-ray particle is not always absorbed in the counter when it enters into the plastic-scintillation counter. Due to the bremsstrahlung process, a part of its energy escapes from the counter. Namely even when a monochromatic β-ray enters into the E-counter, the counter response is not a simple delta function in the pulse height spectrum, but is the one having a low energy tail caused by the bremsstrahlung process. In addition, the counter resolution is finite. In the case of the positron decay, annihilation γ-rays make the counter response more complicated. The shape of low energy tail is increased due to the annihilation of positrons in flight, and the counter response also have a high energy tail due to the absorption of the annihilation γ-rays. So, strictly speaking, the energy deposit function is different between the electron and positron decay. As is shown in Figure 4.1, the energy deposit function is parameterized as

$$f(x, E) = (1 - r)\delta(x - E) + rY(x - E)\exp\{\lambda(x - E)\}, \tag{4.3}$$

where E is the incident β-ray energy, and x is the absorbed energy. The parameters r and λ are the ratios of the low energy tail and the dumping factor of the tail, respectively. $\delta(x)$ and $Y(x)$ are the delta function and the step function, respectively. Since actual β-ray counter has finite energy resolution, the response function $R(x, E)$ is constructed by folding the above energy deposit with the Gaussian function as follows,

$$R(x, E) = \int dy\, f(y, E)\, (1/\sqrt{2\pi}\,\sigma)\exp\{-(x - y)^2/\sigma^2\}, \tag{4.4}$$

where σ corresponds to the resolution for the monochromatic β ray. Since the

resolution σ is thought to come mainly from the finite number of the scintillation light and photoelectrons in the photomultiplier, it is reasonable to assume the form proportional to the square root of the β-ray energy, i.e., $\sigma = \sigma_0\sqrt{E}$. In the Figure 4.1, the schematic shape of the resultant response function is shown. Therefore, the observed β-ray spectrum is described as

$$S(E) = \int dE'\; W(E')R(E, E'). \tag{4.5}$$

The observed β-ray energy spectra were fitted with this type of function. The parameters r, λ, and σ had been determined by the previous experiments [MA85] as,

$$r = 0.17, \tag{4.6}$$

$$\lambda = 0.411/\mathrm{MeV}, \tag{4.7}$$

$$\sigma = 0.22\ (\mathrm{MeV})^{1/2}. \tag{4.8}$$

In the actual fitting process, the normalization factor, zero-point and endpoint channels were searched as free parameters for energy calibration. In the present experiment, the same response function was used for fitting of ^{12}B and ^{12}N spectra for simplicity, in spite of the possible small difference in the spectra between $\beta^{\mp}$ particles.

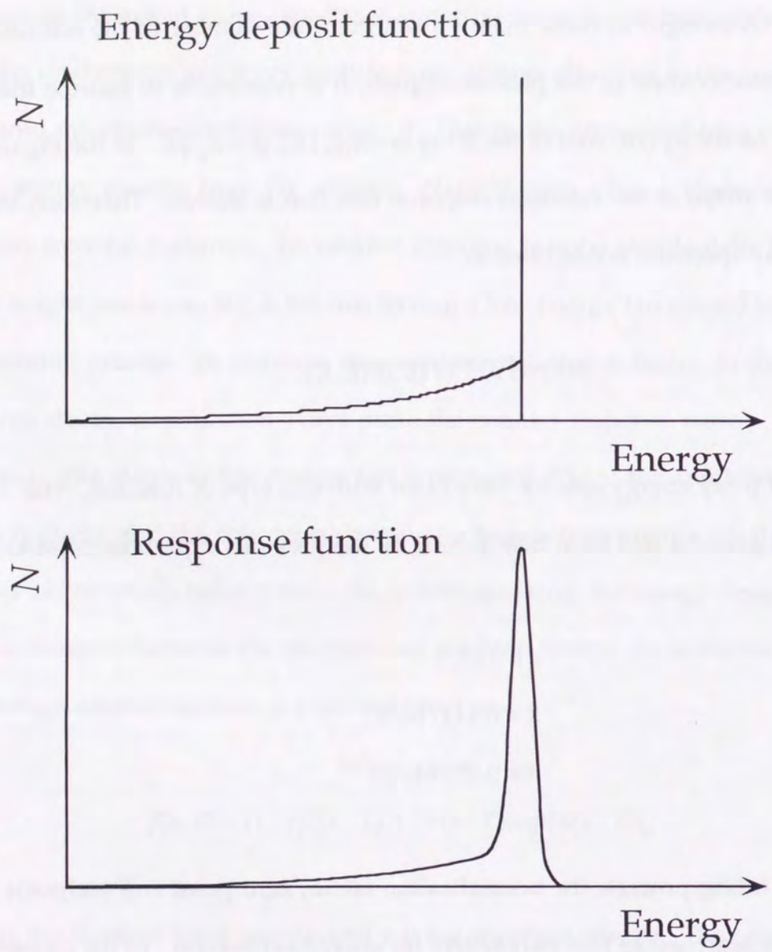

Figure 4.1 Response function of the β-ray counter telescope for the monochromatic β ray.
The energy deposit function has the low energy tail which corresponds to the escaped energy caused by the bremsstrahlung. The counter response function is folded by the Gaussian function .

4.1.2 Energy calibration

The β-ray energy spectra observed in several runs were summed up, and analyzed by the least χ^2 fitting for up and down counters individually. Such least χ^2 fitting analyses were performed for several β emitters. The β emitters used were ^{15}O, ^{17}F, ^{20}F, ^{28}Al, and ^{41}Sc. The β source ^{90}Sr was also used to confirm the energy scaling. The properties of these nuclei are listed in Table 4.1. The β-ray spectra of ^{12}B and ^{12}N together with those of calibration sources are shown in Figure 4.2.

The linearity of the β-ray counter telescopes had been confirmed in the previous experiment [KI92]. Plotting the endpoint channels against the endpoint energies determined by spectrum fittings, the whole scale was determined for both ^{12}B and ^{12}N. The results are shown in Figure 4.3. This procedure of the energy calibration is reliable, since the endpoint channels are free from the distortions due to β-ray scattering, the low energy tail in the counter response and the magnetic field.

Nucleus	$T_{1/2}$	E_0 (MeV)	Production	Energy (MeV)
^{12}N	10.97 ms	16.3160	$^{10}B(^3He, n)^{12}N$	3.0
^{12}B	20.41 ms	13.3695	$^{11}B(d, p)^{12}B$	1.5
^{20}F	11.00 s	5.39086	$^{19}F(d, p)^{20}F$	3.5
^{17}F	64.49 s	1.7387	$^{16}O(d, n)^{17}F$	3.5
^{28}Al	2.2414 m	2.86322	$^{27}Al(d, p)^{28}Al$	3.2
^{15}O	122.24 s	1.7319	$^{16}O(^3He, ^4He)^{15}O$	3.0

Table 4.1 Productions of the calibration β-sources.

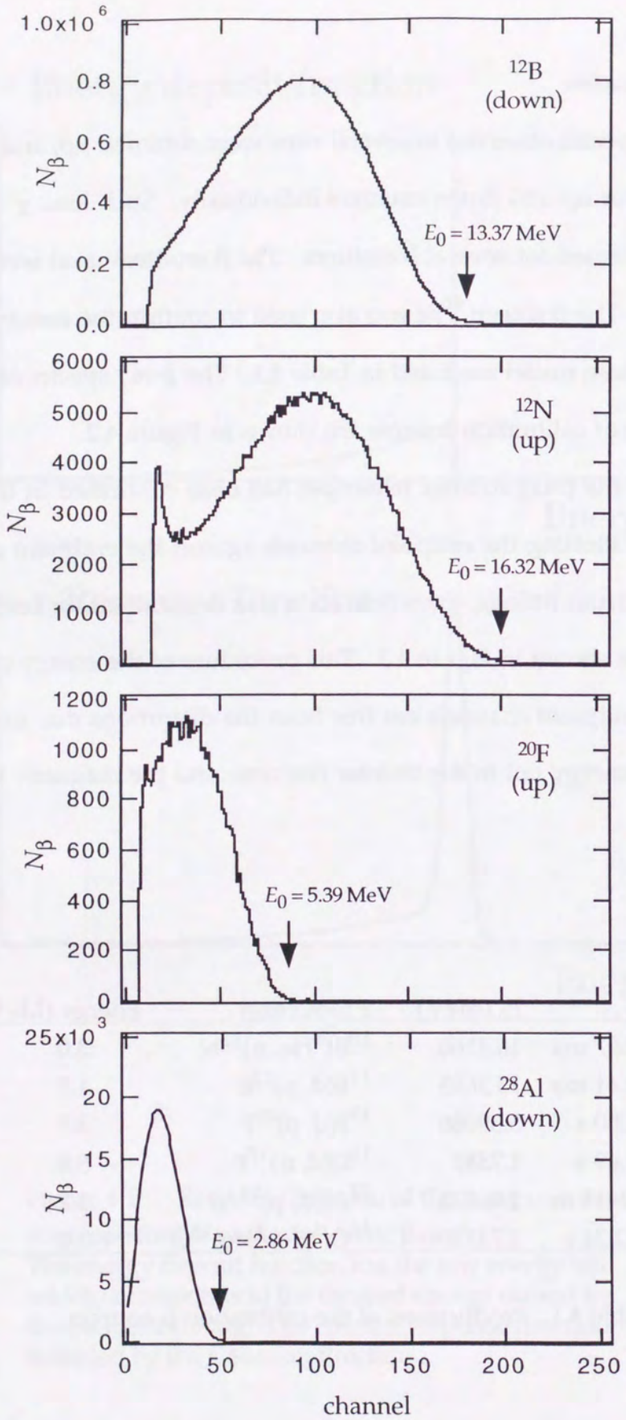

Figure 4.2 Typical β-ray energy spectra of ^{12}B, ^{12}N and calibration sources.

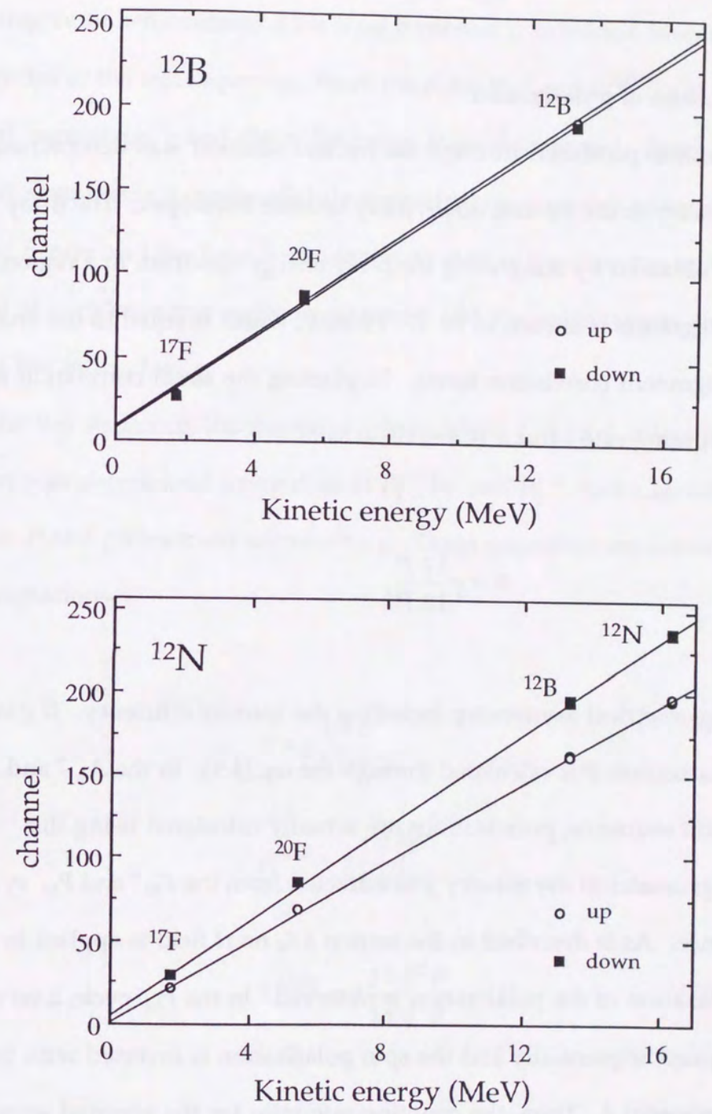

Figure 4.3 Energy calibration of the β-ray counter telescopes. The endpoint channels determined from spectrum fittings are plotted as a function of β-ray endpoint energy. The energy scales were determined by linear fittings of the endpoint channels.

4.2 Determination of polarization and alignment

4.2.1 Determination of polarization

The spin polarization produced through the nuclear reaction was determined from the β-ray asymmetry in the up and down β-ray counter telescopes. The β-ray counting rate is obtained by integrating the β-ray energy spectrum in a region. The region of the integration is chosen to be 5 ~ 13 MeV, which is equal to the analysis region of the alignment correlation terms. Neglecting the small correlation terms, the up-down counting-rate ratio R is described as

$$R = g\frac{1 \mp \boldsymbol{P}}{1 \pm \boldsymbol{P}}, \tag{4.9}$$

where g is the geometrical asymmetry including the counter efficiency. If g is known, the polarization $\boldsymbol{P}$ is calculated through the eq. (4.9). In the A_M^+ and A_M^- cycles in the main sequence, polarizations are actually calculated using this equation. The geometrical asymmetry g is extracted from the P_M^+ and P_M^- cycles in the main sequence. As is described in the section 3.6, no rf field is applied in the P_M^+ cycle, so the relaxation of the polarization is observed. In the P_M^- cycle, a set of AFP rf-fields are applied sequentially and the spin polarization is inverted with the degree of achievement ξ. Then, the counting-rate ratio for the inverted spin ensemble is

$$R^{\mathrm{AFP}} = g\frac{1 \mp \xi\boldsymbol{P}}{1 \pm \xi\boldsymbol{P}}. \tag{4.10}$$

Here, the degree of achievement ξ for total inversion is extracted from the P_T^+, P_T^- and P_T^{++} cycles in the test sequence. From the R for P_M^+ and R^{AFP} for P_M^-, the geometrical asymmetry g and the polarization $\boldsymbol{P}$ are determined. Since the geometrical asymmetry g can be slightly dependent on time due to small but finite background β-rays and the time dependent gain shift of the detector system, g is determined at each counting section separately, and the polarizations are calculated in terms of the individual g.

From the test sequence, the degree of achievement ξ of total inversion of the polarization was determined using data in P_T^+, P_T^- and P_T^{++} cycles, as well as the polarization $\boldsymbol{P}$ and geometrical asymmetry g. These quantities are extracted from following equations,

$$R = g\frac{1 \mp \boldsymbol{P}}{1 \pm \boldsymbol{P}}, \tag{4.11}$$

$$R^{\mathrm{AFP}} = g\frac{1 \mp \xi\boldsymbol{P}}{1 \pm \xi\boldsymbol{P}}, \tag{4.12}$$

$$R^{2\mathrm{AFP}} = g\frac{1 \mp \xi^2\boldsymbol{P}}{1 \pm \xi^2\boldsymbol{P}}, \tag{4.13}$$

Note that the degree of achievement ξ is a negative quantity close to -1. In the test sequences, the degrees of achievement η of the AFP were measured for both LF and HF using data in the A_T^+ and A_T^- cycles. The polarization of the counting section I is

$$P_{\mathrm{I}} = a_{+1} - a_{-1}, \tag{4.14}$$

by the magnetic substate populations a_m. By applying the LF AFP, the magnetic substates between m = -1 and 0 are interchanged, and the resultant polarization becomes

$$P_{\mathrm{I}\to\mathrm{II}} = a_{+1} - (\eta a_0 + (1 - \eta)a_{-1}). \tag{4.15}$$

Here, η denotes the degree of achievement of LF AFP. By applying the same rf, the polarization in the counting section II becomes

$$P_{\mathrm{II}} = a_{+1} - \{\eta((1 - \eta)a_0 + \eta a_{-1}) + (1 - \eta)(\eta a_0 + (1 - \eta)a_{-1})\}. \tag{4.16}$$

Using these three equations with $a_{+1} + a_0 + a_{-1} = 1$, the degree of achievement of LF AFP is extracted. The degree of achievement η for HF AFP is derived similarly. In this extraction of η, the relaxation of the polarization is taken into account, which is determined from the P_{T}^{+}, P_{T}^{-}, and P_{T}^{++} cycles.

4.2.2 Determination of alignment

The obtained alignments were calculated from the measured spin polarizations and the degrees of achievement of the AFPs. The alignment A_{II}^{i} at the begging of the counting section II is derived from the polarization-change between the counting section I → II, and so the final alignment A_{II}^{f} at the end of the counting section II from the polarization-change between II → III. In the A_{M}^{+} cycle, the observed polarizations at each section are described as follows,

$$P_{\mathrm{I}} = a_{+1} - a_{-1}, \tag{4.17}$$

$$P_{\mathrm{II}} = a_{+1} - \{\eta a_0 + (1 - \eta)a_{-1}\}, \tag{4.18}$$

$$P_{\mathrm{III}} = a_{+1} - [\eta\{(1 - \eta)a_0 + \eta a_{-1}\} + (1 - \eta)\{\eta a_0 + (1 - \eta)a_{-1}\}]. \tag{4.19}$$

Here, the relation $a_0 \approx a_{-1}$ holds due to the first depolarization field. The alignment to be calculated is

$$A_{\mathrm{II}}^{+} = 1 - 3\{(1 - \eta)a_0 + \eta a_{-1}\}. \tag{4.20}$$

So, the initial alignment A_{II}^{i} is calculated from the eq. (4.17), (4.18) and (4. 20) to be

$$A_{\mathrm{II}}^{i} = 2\eta P_{\mathrm{I}} - P_{\mathrm{II}}. \tag{4.21}$$

where P_i is the polarization in the counting section i, and η is the degree of achievement. Similarly, the final alignment A_{II}^{f} is calculated from the eq. (4.18), (4.19) and (4. 20) as

$$A_{\mathrm{II}}^{f} = (2/\eta)\, P_{\mathrm{II}} - P_{\mathrm{III}}, \tag{4.22}$$

In the alignment calculation of the eq. (4.21) and (4.22), the polarizations were corrected for the effect of the spin relaxation, because observed polarizations were averaged over the counting times.

The average alignment in the counting section II is calculated form the A_{II}^{i} and A_{II}^{f} taking into account the spin-lattice relaxation time of the alignment and the nuclear lifetime as

$$A_{\mathrm{II}}^{\mathrm{eff}} = \frac{\int A(t)N(t)dt}{\int N(t)dt}, \tag{4.23}$$

with

$$A(t) = A_i \exp(-\lambda_A t), \tag{4.24}$$

$$N(t) = N_i \exp(-t/\tau), \tag{4.25}$$

where λ_A is the relaxation constant of the alignment in the counting section II which is derived from the $A_{\mathrm{II}}{}^i$ and $A_{\mathrm{II}}{}^f$, and τ is the mean lifetime of the nucleus. The obtained results on the polarizations and alignments are shown in Figure 4.4 and are listed in Table 3.5.

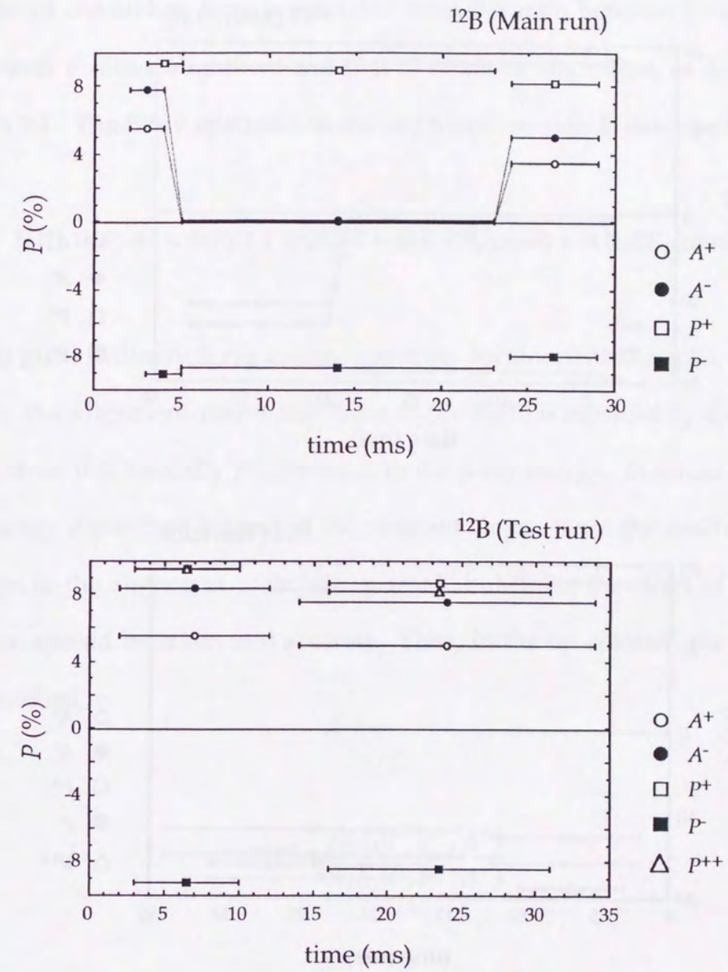

Figure 4.4(a) Result of the spin manipulation of ^{12}B. The upper figure shows the polarization-change in the Main run, and the lower shows that in the Test run. These figures show that the present spin manipulation was successful.

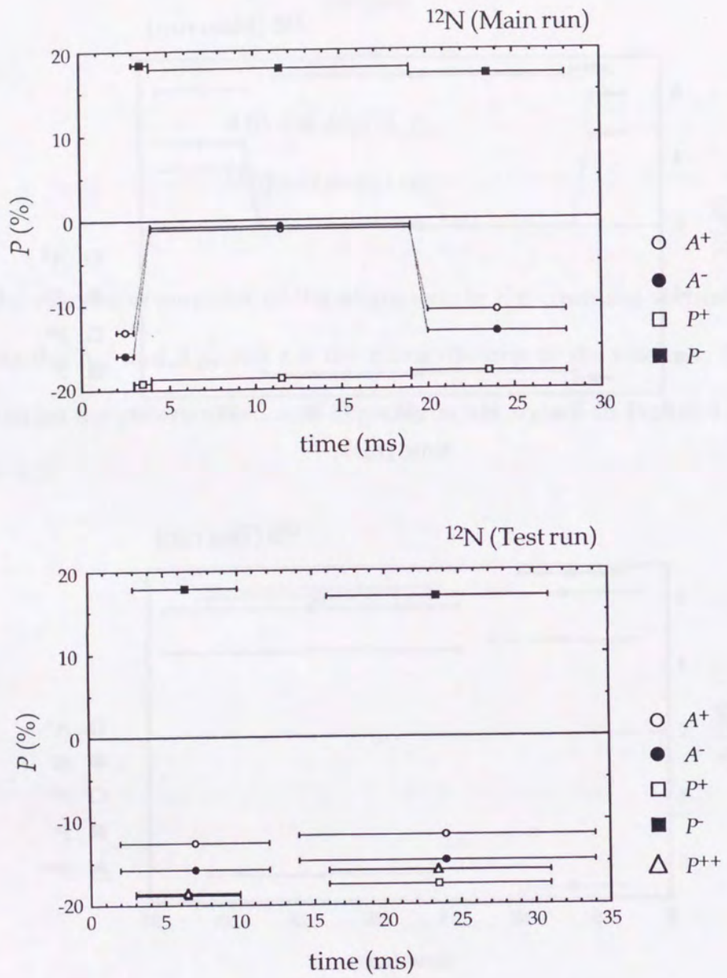

Figure 4.4(b) Result of the spin manipulation of ^{12}N.

4.3 Alignment correlation term

The alignment correlation term is extracted from the ratio between β-ray energy spectrum with positive alignment and that of negative alignment, as described in the section 3.1. The β-ray spectrum in the alignment section is described as

$$N(E, \theta, P, A) = S(E)\{1 \mp (p/E)(1 + \alpha_{\mp}E)PP_1(\cos\theta) + A\,\alpha_{\mp}EP_2(\cos\theta)\}, \qquad (4.26)$$

where $S(E)$ gives ordinary β-ray energy spectrum for unoriented nuclei In this expression, the alignment correlation term $B_2(E)/B_0(E)$ is replaced by the simple form $\alpha_{\mp}E$, since it is basically proportional to the β-ray energy. In actual case, $\alpha_{\mp}$ is slightly energy dependent instead of the constant slope. Since the residual polarization in the alignment cycle is very small, but finite, the effect of the polarization should be taken into account. Thus, in the up counter, the spectrum ratio is described as

$$R(E) = \frac{N(E,0°,P^+,A^+)}{N(E,0°,P^-,A^-)}. \qquad (4.27)$$

From this equation, the alignment correlation term is derived to be

$$\alpha_{\mp}E = \frac{1 \mp P^+(1+\alpha_{\mp}E) - R(E)\{1 \mp P^-(1+\alpha_{\mp}E)\}}{R(E)A^- - A^+}. \qquad (4.28)$$

In the alignment cycle, $P^+ \approx P^-$ and $\Delta P = P^+ - P^- < 0.01$. So, $\Delta P\alpha_{\mp}E < 1 \times 10^{-3}$ is negligible. Therefore, the alignment correlation term measured by the up counter is

written as

$$\alpha_{\mp}E = \frac{1 - R_{\mathrm{u}}(E) \pm \Delta P}{R_{\mathrm{u}}(E)A^{-} - A^{+}}. \tag{4.29}$$

Similarly, the alignment correlation term by the down counter is

$$\alpha_{\mp}E = \frac{1 - R_{\mathrm{d}}(E) \mp \Delta P}{R_{\mathrm{d}}(E)A^{-} - A^{+}}. \tag{4.30}$$

By summing the effects from the up and down counters, the effect of the residual polarization is canceled out. Finally, the alignment correlation term is given as

$$\alpha_{\mp}E = \frac{(R_{\mathrm{u}}(E) - 1) + (R_{\mathrm{d}}(E) - 1)}{2\Delta A}, \tag{4.31}$$

with

$$\Delta A = A^{+} - A^{-}. \tag{4.32}$$

The β-ray energy spectra measured in the alignment cycles were summed up in the ranges of 1 MeV bins. The alignment correlation term is calculated in each energy bin, through the eq. (4.31). Thus obtained alignment correlation terms $B_2(E)/B_0(E) \approx \alpha_{\mp}E$ are shown in Figure 4.5 as a function of the β-ray total energy.

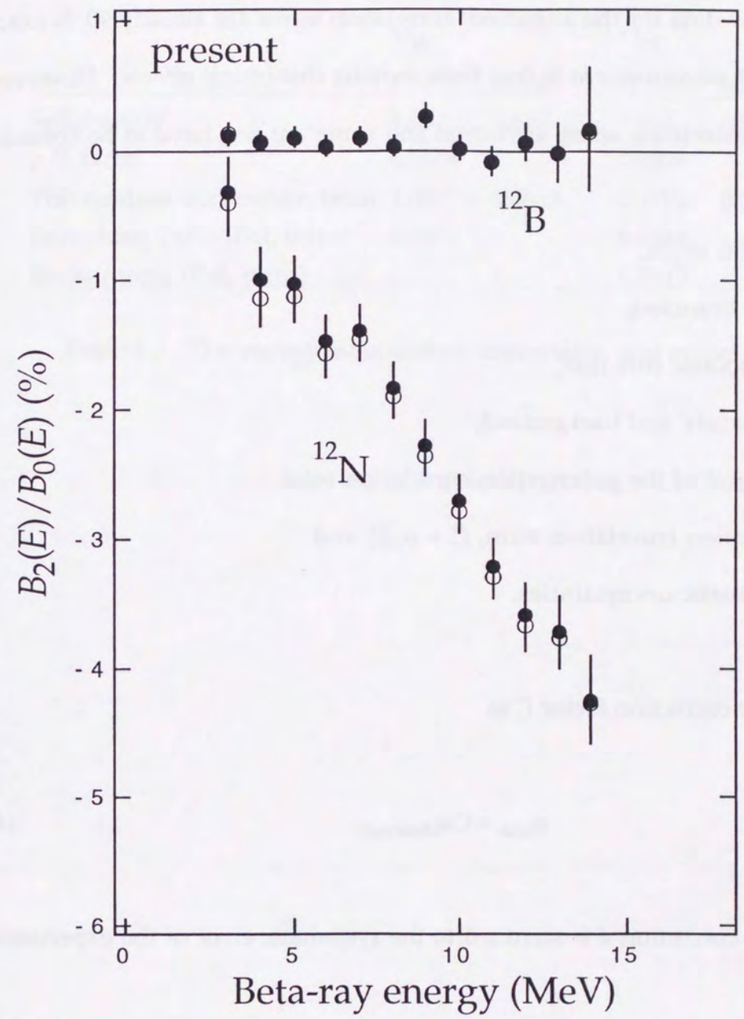

Figure 4.5 Alignment correlation terms as a function of β-ray energy. The open circles are uncorrected data, and the closed circles are corrected one. β-ray energy is the total one including the rest mass.

4.4 Corrections and errors

The obtained raw data for the alignment correlation terms are already 90 % exact, since the present measurement is free from various disturbing effects. However, possible small corrections, some are trivial and some are not, have to be considered.

1. counter solid angle,
2. other β-ray branches,
3. counter response function,
4. beam admixture and background,
5. coefficient p/E of the polarization correlation term,
6. the polarization correlation term, $(1 + \alpha_{\mp}E)$, and
7. other systematic uncertainties.

Let us define the correction factor C as

$$\alpha_{\text{true}} = C\alpha_{\text{observed}}. \tag{4.33}$$

The error of the correction d is summed to the systematic error of the experiment, as follows

$$\Delta\alpha_{\text{true}} = \{\Delta\alpha_{\text{observed}}^{2} + (d\ \alpha_{\text{observed}})^{2}\}^{1/2}. \tag{4.34}$$

The energy independent correction factors are summarized in Table 4.2. Those which depend on the β-ray energy are listed in Table 4.3 - 4.5.

	^{12}B		^{12}N	
	C	error	C	error
Solid angle	1.031	0.010	1.031	0.010
p/E factor	0.9974	-	0.9978	-
Polarization correlation term	1.0007	0.0010	0.9772	0.0020
Branching ratio (Pol. term)	0.9871	-	0.9746	-
Background (Pol. term)	-	-	0.9812	-

Table 4.2 The energy independent corrections and errors.

4.4.1 Solid-angle correction

Since the counter solid angle is finite, both polarization and alignment have to be replaced by the average over the present solid angle. The counter solid angle correction is necessary because of the different angular dependence between the polarization correlation term $P_1(\cos\theta)$ and the alignment correlation term $P_2(\cos\theta)$. The alignment ΔA is deduced from the polarizations and the degrees of achievement of the AFPs, but the alignment correlation term itself has the different angular dependence.

The observed polarization is the average over the solid angle as

$$P_{\rm obs} = \int d\Omega\, P P_1(\cos\theta) \,/\, \int d\Omega\,. \tag{4.35}$$

The solid angle Ω of the β-ray counter telescope is

$$\Omega = 2\pi(1 - \cos\theta_0). \tag{4.36}$$

The cone region with the polar angle θ_0 is the present solid angle. In the present condition, $\theta_0 = 14^\circ$. Thus, the polarization is written as

$$P_{\rm obs} = P(1 + \cos\theta_0)/2. \tag{4.37}$$

Since the observed alignment $\Delta A_{\rm obs}$ is calculated based on the observed polarizations,

$$\Delta A_{\rm obs} = \Delta A\,(1 + \cos\theta_0)/2. \tag{4.38}$$

Similarly, the observed alignment correlation term is

$$\begin{aligned}(A\,\alpha_{\mp}E)_{\rm obs} &= \int d\Omega\, A\,(\alpha_{\mp}E)_{\rm true} P_2(\cos\theta) \,/\, \int d\Omega \\ &= A\,(\alpha_{\mp}E)_{\rm true}\cos\theta_0(1 + \cos\theta_0)/2.\end{aligned} \tag{4.39}$$

The observed alignment correlation term $\alpha E_{\rm obs}$ is written as

$$(\alpha E)_{\rm obs} = (A\,\alpha E)_{\rm obs}/\Delta A_{\rm obs} = (\alpha E)_{\rm true}\cos\theta_0. \tag{4.40}$$

So, the correction factor is $C_\Omega = 1 / \cos\theta_0$, which is 1.031 for the present condition as listed in Table 4.2.

4.4.2 Decay-branch correction

The β-decay branches to the excited states of ^{12}C distort the β-ray energy spectra. This effect from other β-ray branches is caused through both the polarization term and the alignment term.

As is already explained, the β-ray angular distribution for the ground state transition is written as

$$W(E) = S_0(E)[1 \mp (p/E)(1 + \alpha_{\mp}E)PP_1(\cos\theta) + A\,\alpha_{\mp}EP_2(\cos\theta)], \tag{4.41}$$

while that for the β-ray branch to the first excited state (4.439 MeV) is written as

$$W(E) = S_1(E)[1 \pm (1/2)(p/E)(1 + \alpha_{\mp}E)PP_1(\cos\theta) + (1/10)A\,\alpha_{\mp}EP_2(\cos\theta)]. \tag{4.42}$$

Similarly, the angular distribution for the branch to the second excited state (7.654 MeV) is written as

$$W(E) = S_2(E)[1 \mp (p/E)(1 + \alpha_{\mp}E)PP_1(\cos\theta) + A\,\alpha_{\mp}EP_2(\cos\theta)]. \tag{4.43}$$

So, the actual angular distribution is the sum of these, as follows

$$\begin{aligned} W(E) = S(E)[1 & \\ & \mp (1 - 3/2\, S_1(E)/S(E))(p/E)(1 + \alpha_{\mp}E)PP_1(\cos\theta) \\ & + (1 - 9/10\, S_1(E)/S(E))A\,\alpha_{\mp}EP_2(\cos\theta)], \end{aligned} \tag{4.44}$$

where $S(E) = S_0(E) + S_1(E) + S_2(E)$ is the total β-ray spectral shape without the orientation.

So, the correction factor through the polarization term, which is independent of

the β-ray energy, is given as

$$C_{Br}^{P} = 1 - \frac{3}{2}\frac{\int S_1(E)dE}{\int S(E)dE}, \tag{4.45}$$

where the region of the integration is set equal to the analysis region 5 ~ 13 MeV. This is because the alignment is determined from the polarizations and the polarizations are quenched by the branches. This $C_{BR}{}^{P}$ is 0.9871 and 0.9746 for ^{12}B and ^{12}N, respectively, as shown in Table 4.2.

The correction factor of the alignment term is given as

$$C_{Br}^{A} = 1 - \frac{9}{10}\frac{S_1(E)}{S(E)}. \tag{4.46}$$

This correction factor and the total branch correction $C_{Br} = C_{Br}{}^{P} \times C_{Br}{}^{A}$ are given in Table 4.3 as a function of β-ray energy.

	^{12}B		^{12}N	
E (total)	$C_{Br}{}^{A}$	C_{Br}	$C_{Br}{}^{A}$	C_{Br}
3	1.0237	1.0104	1.0299	1.0037
4	1.0213	1.0080	1.0291	1.0030
5	1.0179	1.0048	1.0275	1.0014
6	1.0138	1.0007	1.0251	0.9991
7	1.0092	0.9962	1.0221	0.9962
8	1.0049	0.9919	1.0184	0.9926
9	1.0018	0.9889	1.0141	0.9884
10	1.0004	0.9875	1.0095	0.9839
11	1.0000	0.9871	1.0053	0.9798
12	1.0000	0.9871	1.0022	0.9768
13	1.0000	0.9871	1.0006	0.9753
14	1.0000	0.9871	1.0001	0.9747
15	1.0000	0.9871	1.0000	0.9746

Table 4.3 Branching ratio correction.

4.4.3 Correction for counter response

The counter response such as finite energy resolution and the low energy tail also disturbs the β-ray energy spectrum. The β-ray energy spectrum to be observed is described as

$$W_{\mathrm{obs}}(E) = \int dE'\ W(E')R(E, E'). \tag{4.47}$$

where $R(E, E')$ is the response function of the counter telescope, for finding energy at E for the incident monochromatic β-ray with energy E'. $W(E')$ is the β-ray angular distribution function. As is described in the section 4.1, the response function $R(E, E')$ is described as the energy deposit function folded by the Gaussian, where the energy deposit function has the form of the delta function with an exponential tail. The energy resolution is assumed to be proportional to the square root of β-ray energy.

The observed spectrum is written as

$$\begin{aligned} W_{\mathrm{obs}}(E) &= \int dE'\ S(E')(1 + A\alpha E)R(E, E') \\ &= S'(E)\{1 + A\alpha E\,(1/C_{\mathrm{res}})\}, \end{aligned} \tag{4.48}$$

So, the correction C_{res} is given as

$$C_{\mathrm{res}} = E\frac{\int S(E)R(E,E')dE}{\int S(E)ER(E,E')dE}, \tag{4.49}$$

$$S'(E) = \int dE'\ S(E')R(E, E'). \tag{4.50}$$

This correction factor C_{res} for the response function is listed in Table 4.4. The response function used for the analysis is the same as those used for the spectrum fitting.

	^{12}B	^{12}N
E (total)	C_{res}	C_{res}
3	0.8066	0.7765
4	0.8784	0.8538
5	0.9193	0.8987
6	0.9456	0.9272
7	0.9651	0.9470
8	0.9812	0.9619
9	0.9960	0.9740
10	1.0115	0.9849
11	1.0303	0.9955
12	1.0553	1.0065
13	1.0894	1.0194
14	1.1312	1.0358
15	1.1796	1.0578

Table 4.4 Response function correction.

4.4.4 Correction for polarization-correlation term

Since the spin alignment is calculated from the measured polarization, the correction due to the polarization correlation term is necessary. Trivial correction for the factor p/E in the polarization term is also necessary. Both the p/E and $(1 + \alpha_T E)$ terms are integrated over the analysis energy range, and these correction factors are given as

$$C_{v/c} = \int dE\,(p/E)W(E)/\int dE\,W(E), \tag{4.51}$$

and

$$C_{\text{p-term}} = \int dE\,(1 + \alpha_T E)W(E)/\int dE\,W(E), \tag{4.52}$$

Here, $W(E)$ is the β-ray spectral function, taking into account the response function. The obtained correction factors are listed in Table 4.2 together with other energy independent corrections.

4.4.5 Background correction

Since the analysis region of the alignment correlation terms is high (5 ~ 13 MeV), there should be no background activities in this energy region. However, a small admixture of HD molecular beam in the ^{3}He beam in the production of ^{12}N causes the nuclear reaction with the very small concentration of ^{11}B in the enriched ^{10}B target, to produce ^{12}B contamination in the ^{12}N energy spectrum.

The angular distribution function is distorted by the background $f(E)$, as follows

$$\begin{aligned} W(E) &= S(E)[1 \mp (p/E)(1+\alpha_{\mp}E)\boldsymbol{P}P_1(\cos\theta) + \boldsymbol{A}\,\alpha_{\mp}EP_2(\cos\theta)] + f(E) \\ &= \{S(E)+f(E)\}[1 \\ &\qquad \mp \{S(E)/(S(E)+f(E))\}(p/E)(1+\alpha_{\mp}E)\boldsymbol{P}P_1(\cos\theta) \\ &\qquad + \{S(E)/(S(E)+f(E))\}\boldsymbol{A}\,\alpha_{\mp}EP_2(\cos\theta)]. \end{aligned} \tag{4.53}$$

Thus, the correction factors for both the polarization term and the alignment term are necessary. For the correction for the polarization term is given by integrating the polarization over the present energy range. So, the correction factor is written as

$$\begin{aligned} C_{bg} &= \frac{\int S(E)dE}{\int\{S(E)+f(E)\}dE} \Big/ \frac{S(E)}{S(E)+f(E)} \\ &\approx 1 + \frac{f(E)}{S(E)} - \frac{\int f(E)dE}{\int S(E)dE}. \end{aligned} \tag{4.54}$$

The production ratio of total amount of ^{12}B in ^{12}N was previously determined to be 2 %. The correction factors are listed in Table 4.5.

E (total)	$C_{bg}{}^{A}$	C_{bg}
3	1.0293	1.0099
4	1.0284	1.0091
5	1.0271	1.0078
6	1.0257	1.0064
7	1.0240	1.0047
8	1.0219	1.0027
9	1.0192	1.0001
10	1.0160	0.9969
11	1.0123	0.9933
12	1.0084	0.9894
13	1.0047	0.9858
14	1.0021	0.9833
15	1.0007	0.9819

Table 4.5 Background correction.

4.4.6 Others

The following systematic errors are considered.

1. the error of the alignment,
2. energy scaling of the β-ray spectra, and
3. asymmetry caused by the beam fluctuation.

The error of the alignment shifts the whole data points of the alignment correlation terms. This uncertainty is included in the systematic error. As is described in the section 4.1, the endpoint energies determined from spectrum fittings slightly deviate from a straight line. The error coming from this non-linearity is considered in the systematic error. Finally, the beam fluctuation causes a spurious asymmetry, because the β-ray energy spectra for positive and negative alignments are measured in different beam cycles in the main sequence. This uncertainty is expected to be very small, because a lot of cycles are alternatively repeated, so that this spurious asymmetry will be averaged. In order to check the possible spurious asymmetry from this beam fluctuation, the counting asymmetry between positive and negative alignment was extracted from the present data as described in detail in the appendixes. However, calculated uncertainty of the asymmetry in this check analysis has a significantly large error due to counting statistics.

The corrections and errors are summarized in Table 4.6. These corrections were defined by the ratios of the corrected $\alpha_{\mp}$ to the uncorrected ones. The errors of these corrections were quadratically summed up like statistical error, because considerably large number of independent uncertainties are included.

	^{12}B		^{12}N	
	Corr.	Error	Corr.	Error
Alignment	-	0.23	-	0.58
Counter response	-2.63	2.13	-1.54	1.89
Background / HD admix.	-	-	-0.55	0.23
Branching ratio	-1.05	0.03	-1.71	0.03
Solid angle	3.10	0.40	3.10	0.40
p/E factor	-0.60	-	-0.30	-
$(1 + \alpha_{\mp}E)$ factor	-0.27	0.10	-2.37	0.20
Energy scaling	-	0.73	-	0.74
Total error	-	2.30	-	2.17

Table 4.6 The correction factors and errors.

Chapter 5

Results and discussions

5.1 Results

The obtained alignment correlation terms are shown in Figure 4.5, and are listed in Table 5.1. In order to check the consistency of the present analysis with reported old ones, we first analyzed the data by assuming a linear dependence on the β-ray energy for the alignment correlation term, neglecting the higher order contributions, as described in the section 2.2. The alignment correlation terms were analyzed in the energy range 5 ~ 13 MeV for both ^{12}B and ^{12}N, where the distorted low-energy region was rejected, since the β-ray scattering effect might not be avoided completely. From the least square fitting, the alignment correlation coefficients $\alpha_{\mp}$ were determined to be

$$\alpha_{-} = +0.0082 \pm 0.0029 \text{ (stat.)} \pm 0.0077 \text{ (syst.) \%/MeV}, \tag{5.1}$$

$$\alpha_{+} = -0.2661 \pm 0.0070 \text{ (stat.)} \pm 0.0103 \text{ (syst.) \%/MeV}. \tag{5.2}$$

The results are listed in Table 5.2.

We have two previously obtained data of the alignment correlation coefficients in the A = 12 system. Since 1985, we have been improving the spin manipulation technique. From the analyses using the improved knowledges of the hyperfine interactions, we obtain precise results from the previous experiments which were

essentially the same as the present one. The data, measured at 1985 and 1992, were reanalyzed in the same manner as the present analysis, and were corrected for the systematic corrections discussed in the previous sections. As the results, the alignment correlation coefficients were determined to be

$$\alpha_{-} = +0.0035 \pm 0.0048 \text{ (stat.)} \pm 0.0062 \text{ (syst.) \%/MeV}, \tag{5.3}$$

$$\alpha_{+} = -0.2727 \pm 0.0053 \text{ (stat.)} \pm 0.0185 \text{ (syst.) \%/MeV for 1985} \tag{5.4}$$

and

$$\alpha_{-} = -0.0176 \pm 0.0056 \text{ (stat.)} \pm 0.0108 \text{ (syst.) \%/MeV}, \tag{5.5}$$

$$\alpha_{+} = -0.2757 \pm 0.0078 \text{ (stat.)} \pm 0.0154 \text{ (syst.) \%/MeV for 1992} \tag{5.6}$$

as shown in Figure 5.1 and 5.2, and listed in Table 5.3 and 5.4. All results obtained by these simple analyses are consistent with each other.

In order to determine the alignment correlation coefficients more precisely, the higher order effect should be taken into account. Using the full formula of the angular distribution function of the eq. (2.20), the least square fittings were simultaneously performed for ^{12}B and ^{12}N [KO97]. The analysis region was 5 ~ 13 MeV. The analyses were also performed for all data point which include low-energy region. The free parameters for the fittings were the induced tensor term f_T in the axial-vector current and the axial charge y, instead of the alignment correlation coefficients $\alpha_{\mp}$. The experimental value was used for the weak magnetism term in the alignment correlation term. In these analyses, there is no approximation as far as the lepton part is concerned, i.e., the effects of higher order partial waves of leptons, Coulomb correction of the finite-size nucleus and radiative correction were considered. The results are shown in Figure 5.3 and listed in Table 5.5.

^{12}B

E(total) [MeV]	uncorr. [%]	error (stat.)	C	corr. [%]	error (stat.)	(total)
3.026	0.126	0.086	0.839	0.105	0.086	0.131
4.016	0.065	0.074	0.911	0.060	0.074	0.092
5.008	0.092	0.066	0.950	0.088	0.066	0.105
6.002	0.023	0.061	0.974	0.022	0.061	0.064
6.996	0.099	0.058	0.989	0.098	0.058	0.109
7.989	0.036	0.059	1.002	0.036	0.059	0.068
8.982	0.254	0.062	1.013	0.258	0.062	0.249
9.972	0.019	0.070	1.028	0.019	0.070	0.072
10.958	-0.082	0.086	1.047	-0.085	0.086	0.117
11.939	0.061	0.121	1.072	0.065	0.121	0.136
12.914	-0.021	0.210	1.106	-0.023	0.210	0.211
13.884	0.143	0.458	1.149	0.164	0.458	0.483

^{12}N

E(total) [MeV]	uncorr. [%]	error (stat.)	C	corr. [%]	error (stat.)	(total)
3.028	-0.395	0.257	0.791	-0.313	0.257	0.258
4.019	-1.143	0.235	0.869	-0.993	0.235	0.238
5.013	-1.125	0.212	0.912	-1.026	0.212	0.215
6.007	-1.567	0.193	0.937	-1.468	0.193	0.201
7.002	-1.454	0.181	0.953	-1.386	0.181	0.189
7.998	-1.901	0.174	0.962	-1.829	0.174	0.188
8.994	-2.353	0.172	0.968	-2.277	0.172	0.193
9.990	-2.791	0.177	0.971	-2.711	0.177	0.205
10.984	-3.298	0.188	0.974	-3.212	0.188	0.226
11.977	-3.670	0.210	0.978	-3.589	0.210	0.252
12.969	-3.779	0.249	0.985	-3.723	0.249	0.288
13.956	-4.271	0.319	0.998	-4.262	0.319	0.359

Table 5.1 Alignment correlation terms of $A = 12$ system in the present study. The uncorrected and corrected values of the alignment correlation terms are listed together with the total correction factors.

	^{12}B				^{12}N			
Year	α_-	Error stat.	syst.	total	α_+	Error stat.	syst.	total
1985	0.0035	0.0048	0.0062	0.0078	-0.2727	0.0053	0.0185	0.0192
1992	-0.0176	0.0056	0.0108	0.0121	-0.2757	0.0078	0.0154	0.0173
1996	0.0082	0.0029	0.0077	0.0082	-0.2661	0.0070	0.0103	0.0124
ave.	0.0030	0.0023	0.0077	0.0080	-0.2715	0.0037	0.0103	0.0109

Table 5.2 The simple analyses of the alignment correlation terms.

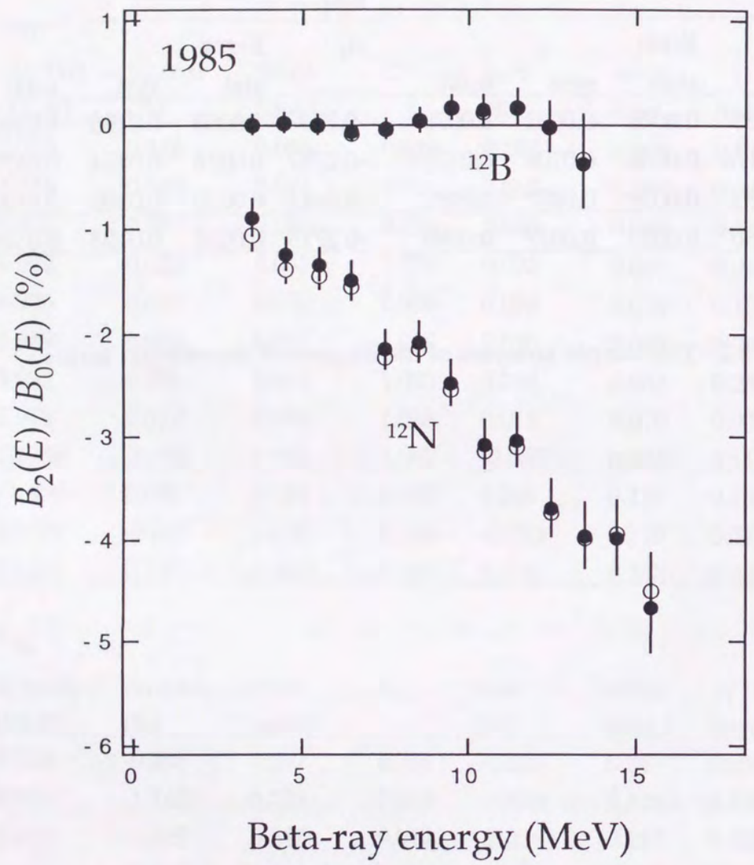

Figure 5.1 Alignment correlation terms (measured at 1985). The open circles are uncorrected data, and the closed are corrected one.

^{12}B

E(total) [MeV]	uncorr. [%]	error (stat.)	*C*	corr. [%]	error (stat.)	(total)
3.506	-0.016	0.111	0.881	-0.014	0.111	0.114
4.484	0.020	0.099	0.934	0.019	0.099	0.104
5.483	-0.005	0.093	0.964	-0.005	0.093	0.093
6.492	-0.081	0.092	0.983	-0.080	0.092	0.167
7.504	-0.053	0.092	0.996	-0.053	0.092	0.130
8.494	0.039	0.102	1.008	0.039	0.102	0.123
9.454	0.163	0.112	1.021	0.166	0.112	0.312
10.432	0.124	0.131	1.037	0.129	0.131	0.260
11.422	0.150	0.167	1.059	0.159	0.167	0.324
12.426	-0.034	0.241	1.089	-0.037	0.241	0.250
13.401	-0.334	0.432	1.128	-0.377	0.432	0.788

^{12}N

E(total) [MeV]	uncorr. [%]	error (stat.)	*C*	corr. [%]	error (stat.)	(total)
3.513	-1.062	0.173	0.841	-0.893	0.173	0.183
4.503	-1.385	0.152	0.899	-1.245	0.152	0.174
5.505	-1.443	0.140	0.932	-1.344	0.140	0.167
6.505	-1.563	0.134	0.952	-1.488	0.134	0.168
7.498	-2.227	0.131	0.964	-2.147	0.131	0.196
8.498	-2.157	0.131	0.971	-2.095	0.131	0.193
9.495	-2.547	0.136	0.976	-2.485	0.136	0.216
10.49	-3.146	0.144	0.978	-3.078	0.144	0.253
11.478	-3.098	0.161	0.982	-3.041	0.161	0.261
12.461	-3.735	0.181	0.987	-3.687	0.181	0.308
13.458	-3.979	0.213	0.997	-3.967	0.213	0.343
14.455	-3.933	0.271	1.013	-3.984	0.271	0.382
15.443	-4.494	0.364	1.037	-4.659	0.364	0.482

Table 5.3 Alignment correlation terms of $A = 12$ system measured at 1985.

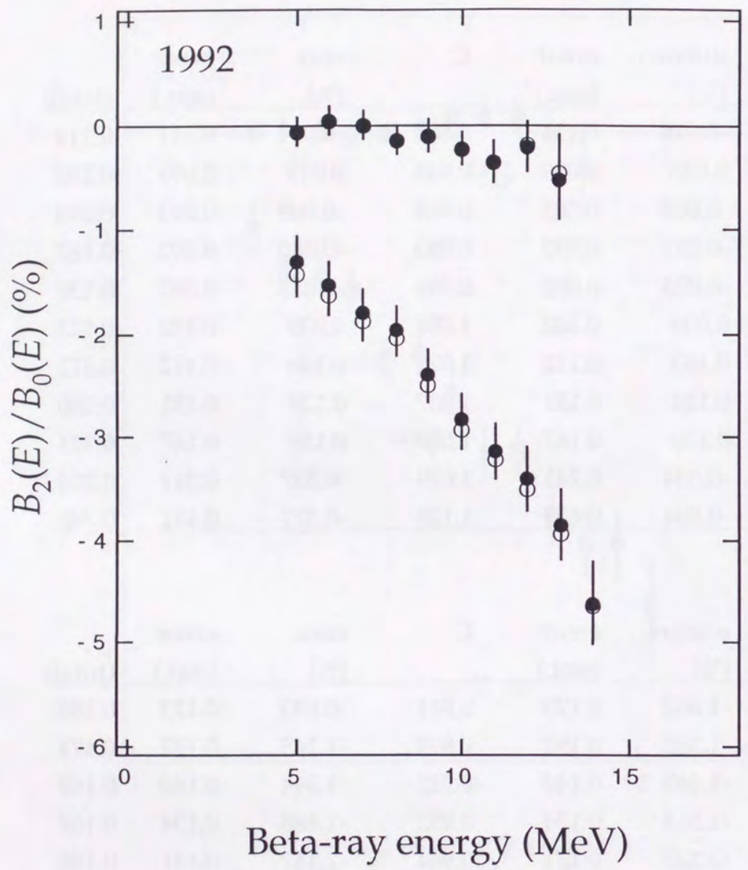

Figure 5.2 Alignment correlation terms (measured at 1992). The open circles are uncorrected data, and the closed are corrected one.

^{12}B

E(total) [MeV]	uncorr. [%]	error (stat.)	C	corr. [%]	error (stat.)	(total)
5.008	-0.078	0.132	0.949	-0.074	0.132	0.139
6.002	0.041	0.122	0.973	0.039	0.122	0.124
6.996	-0.008	0.116	0.988	-0.007	0.116	0.116
7.989	-0.156	0.116	1.001	-0.156	0.116	0.150
8.982	-0.112	0.121	1.012	-0.117	0.121	0.141
9.972	-0.236	0.134	1.027	-0.242	0.134	0.200
10.958	-0.351	0.162	1.046	-0.367	0.162	0.277
11.939	-0.196	0.220	1.071	-0.210	0.220	0.255
12.914	-0.466	0.362	1.105	-0.515	0.362	0.480

^{12}N

E(total) [MeV]	uncorr. [%]	error (stat.)	C	corr. [%]	error (stat.)	(total)
5.013	-1.432	0.229	0.909	-1.302	0.229	0.240
6.007	-1.632	0.212	0.934	-1.524	0.212	0.229
7.002	-1.887	0.200	0.950	-1.793	0.200	0.224
7.998	-2.052	0.194	0.959	-1.969	0.194	0.223
8.994	-2.493	0.193	0.965	-2.405	0.193	0.235
9.990	-2.924	0.199	0.968	-2.831	0.199	0.254
10.984	-3.228	0.213	0.971	-3.135	0.213	0.275
11.977	-3.499	0.236	0.975	-3.411	0.236	0.304
12.969	-3.932	0.277	0.982	-3.862	0.277	0.351
13.956	-4.640	0.345	0.995	-4.616	0.345	0.431

Table 5.4 Alignment correlation terms of $A = 12$ system measured at 1992.

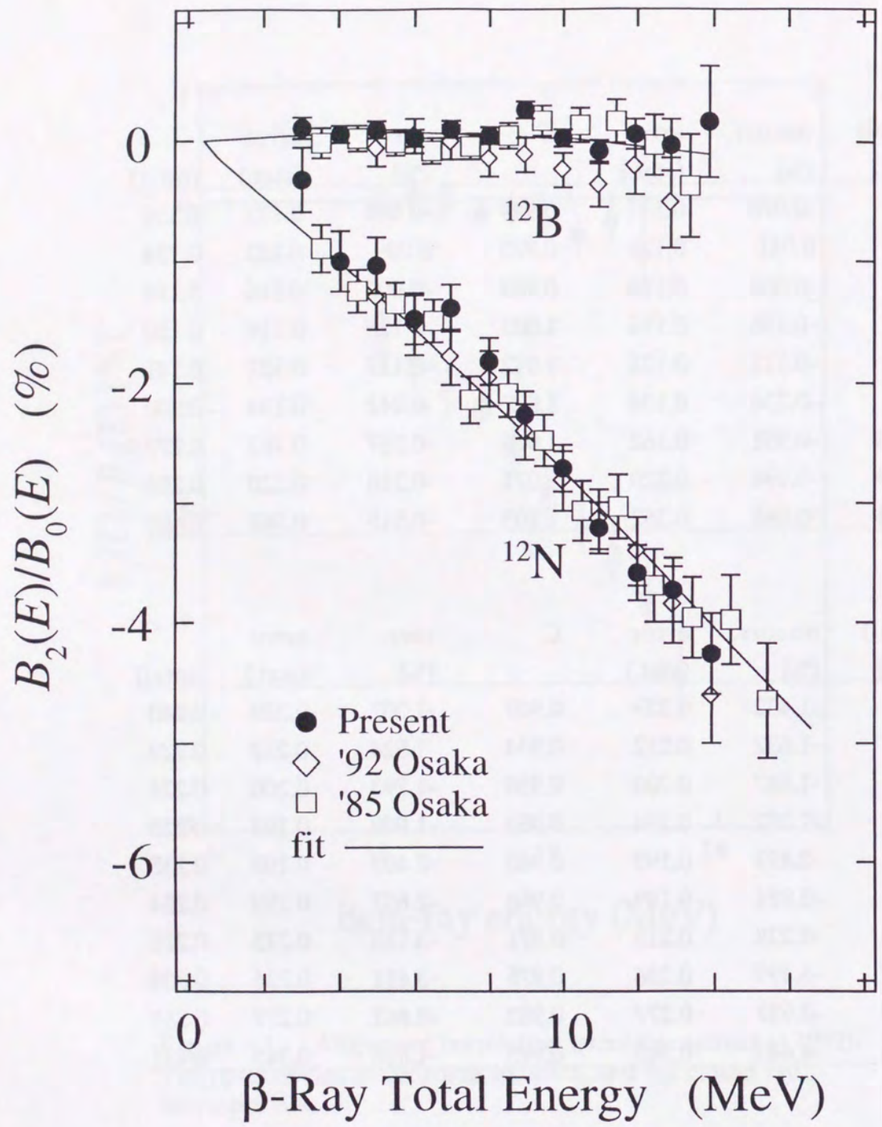

Figure 5.3 Alignment correlation terms (all data). The theoretical best fitted curves are also shown.

Analysis region; 5 ~ 13 MeV

Year	$2Mf_T/f_A$	Error stat.	Error syst.	Error total	y	Error stat.	Error syst.	Error total
1985	0.06	0.10	0.27	0.29	4.69	0.10	0.34	0.35
1992	0.29	0.12	0.27	0.29	5.04	0.13	0.33	0.35
1996	0.07	0.07	0.18	0.19	4.53	0.06	0.22	0.23
ave.	0.12	0.05	0.18	0.19	4.69	0.05	0.22	0.23

Analysis region; all data

Year	$2Mf_T/f_A$	Error stat.	Error syst.	Error total	y	Error stat.	Error syst.	Error total
1985	0.07	0.09	0.27	0.29	4.69	0.10	0.34	0.35
1992	0.23	0.12	0.27	0.29	5.07	0.13	0.33	0.35
1996	0.06	0.07	0.18	0.19	4.57	0.06	0.22	0.23
ave.	0.10	0.05	0.18	0.19	4.71	0.05	0.22	0.23

Table 5.5 Full analyses of the alignment correlation terms. The induced tensor terms and the axial charges are listed.

5.2 Giant mesonic effect in the axial charge and its implications

From the sum of the alignment correlation coefficients, the axial charge matrix element is extracted. The axial charge y was determined to be

$$y_{\text{pre.}} = 4.47 \pm 0.26, \tag{5.7}$$

in the present experiment by the simple analysis. Here, the experimental error includes both statistic and systematic ones. The axial charges from the previous data were also determined to be

$$y_{1985} = 4.66 \pm 0.36, \tag{5.8}$$

$$y_{1992} = 5.08 \pm 0.37. \tag{5.9}$$

Averaging these data, the axial charge was obtained to be

$$y_{\text{ave.}} = 4.65 \pm 0.24, \tag{5.10}$$

from this simple analysis, described in the previous section. This is consistent with the results of the full analysis. The results are listed in Table 5.6.

According to the theoretical calculation by Koshigiri and Morita [KO81][KO89] [KO95a], the axial charge matrix element is given as

$$y_{\text{theo.}} = y_{\text{IA}}(1 + \delta_{\text{CP}} + \delta_{\text{EX}}) + y_{\text{soft-}\pi}. \tag{5.11}$$

The impulse approximation value y_{IA} was evaluated to be 3.17 by the

Hauge-Maripuu model with the Sussex potential for the residual interaction, and the soft-pion contribution $y_{\text{soft-}\pi}$ was evaluated to be 1.30 which is 41 % relative to the impulse value. The core polarization effect δ_{CP} was -10 % relative to the impulse value. Here, the calculation of the core polarization effect was performed up to second order. δ_{EX} is an parameter to reproduce the experimental axial charge.

In order to reproduce the axial charge of the present experiment, an extra enhancement is derived to be δ_{EX} = 16 %. So, the net enhancement ε_{MEC} in the axial charge relative to the IA + CP value reaches 57 %. The extra enhancements were also obtained from the previous data. All the results are listed in Table 5.7, together with the net enhancements. Using all data, the average enhancement was determined to be 57 ± 7 %. From the present analysis, the large enhancement in the axial charge was confirmed in the A = 12 system, as shown in Figure 5.4. This result is similar to results obtained by the first-forbidden transition rates.

In order to understand this large enhancement, the short-range exchange effects of heavy mesons (σ, ω and ρ) were calculated by Koshigiri et al. in the hard-pion model [KO95a]. In this calculation the two-body exchange operators were derived from the realistic nucleon-nucleon interaction, Bonn potential. This is essentially the same manner as Kirchbach's calculation [KI92]. The results are summarized in Table 5.8 [KO95a]. While heavy-meson contributions in the axial charge is 15 ~ 20 %, total enhancement results in around 45 % in this calculation, because of the reduced soft-pion term. So, the present additional enhancement is still unresolved in the picture given here.

It is noted that the core polarization effect, δ_{CP} = -10 %, is strongly sensitive to the tensor force. Since the core polarization effect reduces the enhancement in the axial charge, weakening of the tensor force in the effective interaction is preferable to reproduce the experimental values of axial charges. In the A =12 analysis,

Hamada-Johnston type tensor force was used, which was employed in the analysis of the magnetic form factors of ^{12}C in the electron inelastic scattering [SA79]. So, the present analysis has no ambiguity in this way.

Year	y	stat.	syst.	total	enhance
1985	4.66	0.12	0.34	0.36	57 ± 11%
1992	5.08	0.17	0.33	0.37	70 ± 12 %
1996	4.47	0.13	0.22	0.26	51 ± 8 %
mean	4.65	0.08	0.22	0.24	57 ± 7 %

Table 5.6 Axial charge matrix elements obtained by the simple analysis. The net enhancements in the axial charge relative to the impulse calculation including the core polarization effect are also shown in the right column.

Year	δ_{EX}	stat.	syst.	total	enhance
1985	0.17	0.03	0.11	0.11	58 ± 11 %
1992	0.28	0.04	0.10	0.11	69 ± 11 %
1996	0.02	0.02	0.07	0.07	53 ± 7 %
ave.	0.16	0.02	0.07	0.07	57 ± 9 %

Table 5.7 Extra enhancement in the axial charge obtained by the full analysis. The net enhancements in the axial charge relative to the impulse calculation including the core polarization effect are also shown in the right column.

Meson	Model A [no src]	Model A [src]	Model B [no src]	Model B [src]
π - ρ	0.266	0.269	0.187	0.190
σ	0.096	0.069	0.102	0.073
ω	0.112	0.084	0.111	0.084
ρ	-0.005	0.006	0.032	0.027
$\sigma + \omega + \rho$	0.203	0.159	0.245	0.184
total	0.469	0.428	0.432	0.372

Table 5.8 The enhancement in the axial charge due to the heavy mesons.

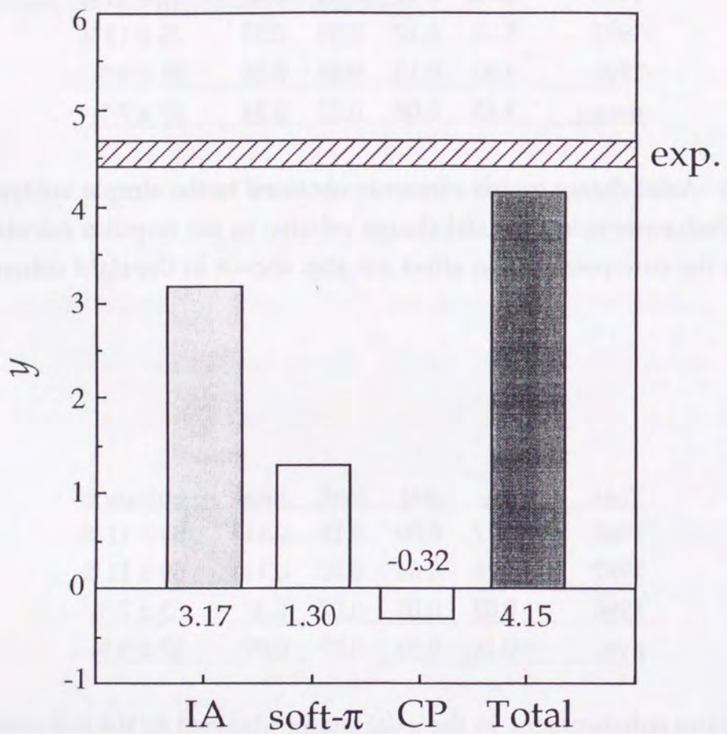

Figure 5.4 Axial charge y in the A = 12 system.
IA: impulse approximation, soft-p; meson exchange current (soft-π contribution), CP; core polarization.

On the other hand, in-medium renormalization of the nucleon mass and the pion-decay constant are proposed in the framework of the chiral perturbation theory [KU91]. According to this theory, masses of the hadrons are scaled as a function of the nuclear density ρ as follows,

$$\frac{m_N^*}{m_N} = \frac{m_\sigma^*}{m_\sigma} = \frac{m_\rho^*}{m_\rho} = \frac{m_\omega^*}{m_\omega} = \frac{f_\pi^*}{f_\pi} = \Phi(\rho), \tag{5.12}$$

where m_N, m_σ, m_ρ, and m_ω are masses of the hadrons, and f_π is the pion decay constant. Here, asterisks refer to the renormalized values in nuclear medium. The enhancement factor ε_{MEC} is written as

$$\varepsilon_{MEC} = \frac{M_1^* + M_2^*}{M_1} = \frac{1}{\Phi(\rho)}\left(1 + \frac{1}{\Phi(\rho)}\frac{M_2}{M_1}\right), \tag{5.13}$$

where

$$M_1{}^* = M_1/\Phi(\rho) \text{ and } M_1{}^* = M_1/\Phi(\rho)^2. \tag{5.14}$$

M_1 and M_2 are axial charge matrix element of the impulse current and the pion exchange current, respectively. In the A = 12 system, $\varepsilon_{MEC} = 1.57 \pm 0.07$ and $M_2/M_1 = 0.41 \pm 0.05$, so we have $\Phi(A = 12) = 0.92 \pm 0.04$. In the lead region, $\varepsilon_{MEC} = 1.8 \pm 0.2$ and $M_2/M_1 = 0.5 \pm 0.1$ [KU91], so we have $\Phi(A = 208) = 0.87 \pm 0.09$. Thus, in the framework of the chiral perturbation theory, the nucleon mass is reduced about 8 % in A = 12 and 13 % in lead region, compared with that in free space. The mass renormalization effect can be also evaluated from the magnetic moments. From the

isoscaler part derived from magnetic moments of mirror nuclei, the renormalization of about 1.5 % was found in the A = 16 system, and about 3 % in A = 40 [MI90]. In the lead region, the mass renormalization of 8 ± 3 % is extracted from anomalous orbital g-factors of magnetic moments [YA85]. The present result looks somewhat large, but is fairly consistent with the renormalization obtained from the analyses of the magnetic moments. In order to examine the in-medium renormalization effect, both experimental and theoretical studies are much encouraged.

5.3 Influences of the present results to other symmetry problems

5.3.1 Induced tensor term in the axial-vector current

The induced tensor current was extracted from the difference between the alignment correlation coefficients of ^{12}B and ^{12}N, as follows

$$\left(\frac{B_2(E)}{B_0(E)}\right)_- - \left(\frac{B_2(E)}{B_0(E)}\right)_+ = \frac{4}{3}\left(a - \frac{f_T}{f_A}\right). \tag{5.15}$$

In order to determine the induced tensor term precisely, the full analysis with higher partial waves of leptons was performed. The results are listed in Table 5.5, together with the axial charge. Here, the experimental value of the weak magnetism term a was used. The γ-decay width of the M1 transition from the 15.11 MeV state of ^{12}C presently gives the most precise value of the weak magnetism a through the relation of the eq. (2.61). Averaging all the available data [EN68][CH73] [DE83] for $\Gamma\gamma$, $\Gamma\gamma$ = 38.2 ± 0.6 eV was determined. The weak magnetism term was thus determined to be

$$2Ma_{\rm exp} = 4.02 \pm 0.02. \tag{5.16}$$

Using this value, the induced tensor term was determined in the present experiment to be

$$2Mf_T / f_A = +0.07 \pm 0.07\ (\text{stat.}) \pm 0.18\ (\text{syst.}), \tag{5.17}$$

where the systematic error was from the uncertainties of the corrections, as described in the section 4.4. The error of the weak magnetism was also included in the

systematic error. The results on the induced tensor term are shown in Figure 5.5, together with old data. Averaging all the results, the induced tensor term is determined with much improved precision to be

$$2Mf_T / f_A = +0.12 \pm 0.05 \text{ (stat.)} \pm 0.18 \text{ (syst.)}. \tag{5.18}$$

Here, it is noted that the statistical error is smaller than the systematic error, so further technical improvements can provide more precise induced tensor term.

A possible asymmetry in the axial charge should be carefully examined. The axial charges of ^{12}B and ^{12}N are not exactly canceled out, because of the difference in the binding energy of the decaying nucleon between ^{12}B and ^{12}N. Koshigiri et al. [KO95b] evaluated this asymmetry which is defined by $\Delta y = (y^+ - y^-)/2$. They obtained $\Delta y = 0.10 \sim 0.13$ using Wood-Saxon potential, the depth of which was adjusted so as to reproduce the binding energy of the decaying nucleon. In the calculation of Δy, meson exchange currents were not included, because the axial charge due to exchange currents consists of both parts from the valence nucleon and the core, while that of the impulse approximation is from the valence only, whose wave functions are subject to the charge asymmetry.

A possible asymmetry in the weak magnetism term is not important. The weak magnetism term is mainly determined by the term $(-f_V/f_A + 2Mf_W/f_A)$, and the residual part $(-f_V/f_A)\int l / \int \sigma$ is ~ 4.5 % of the main term, which may depend on the charge asymmetry.

Assume the Wood-Saxon type radial wave functions for decaying nucleons, $\Delta y =$ 0.10 is given. However, the theoretical asymmetry is model dependent. So, we include 50 % of uncertainty in the Δy, and so we have $\Delta y = 0.10 \pm 0.05$. Summing up Δy, the induced tensor term was finally determined to be

$$\begin{aligned} 2Mf_T/f_{A\text{exp}} &= 2Mf_T/f_{A\text{ave.}} + \Delta y \\ &= +0.22 \pm 0.05 \text{ (stat.)} \pm 0.18 \text{ (syst.}^{\text{exp}}) \pm 0.05 \text{ (syst.}^{\text{theo}}). \end{aligned} \tag{5.19}$$

The present result is much more precise than the old data. The present experiment has disclosed a possibility of non-zero induced tensor term in the axial-vector current for the first time, although the result can not reject completely non existence of the second class current.

Recently, a prediction [SH96] of the induced tensor term based on the QCD sum rule has been given to be

$$2Mf_T/f_A = +0.0152 \pm 0.0053. \tag{5.20}$$

The second class current arises from the mass- and charge difference between up and down quarks in QCD. This value is consistent with the present result.

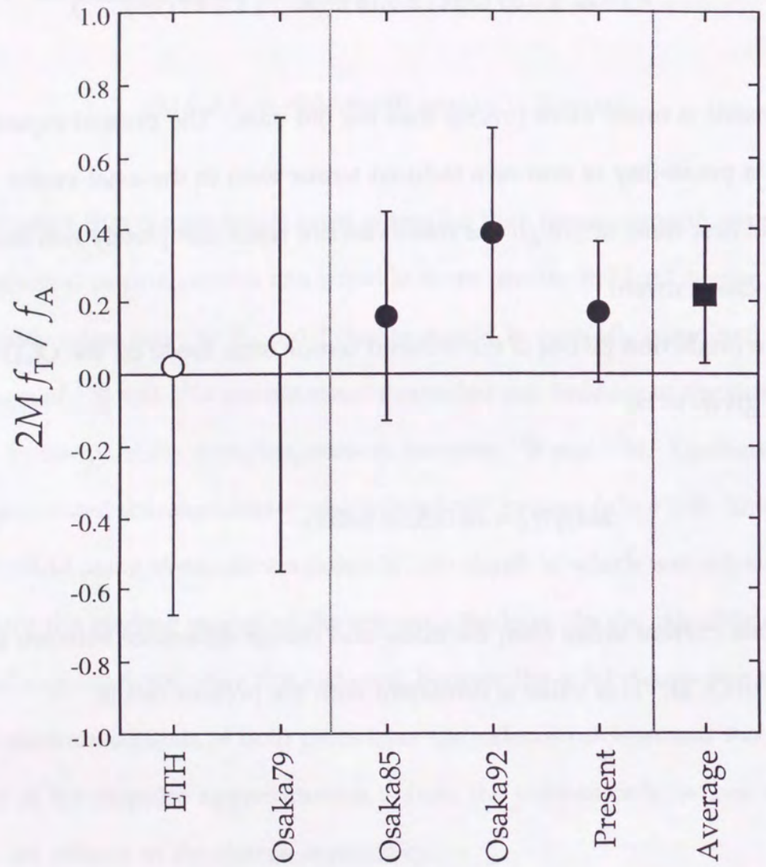

Figure 5.5 Results on the induced tensor term. The data of Osaka85 and Osaka92 were reanalyzed, and were averaged together with the present data. In these analyses, a possible asymmetry of the axial charge Δy is included.

5.3.2 Weak magnetism term

The test of the CVC (Conserved vector current) hypothesis have been done in two ways. As is described in Sec. 2.4, the shape factor in the β-ray energy spectrum has been measured by several methods [WU77][KA77][CA90][FU96]. Also, the measurement of γ-decay width of M1 transition from the analog state (15.11 MeV) gives information about the weak magnetism term.

The present experiment can test the CVC hypothesis. Suppose the induced tensor term is exactly zero, since the induced tensor term is very small, a few % relative to the weak magnetism a. The difference between the alignment correlation coefficients is then written as

$$\alpha_- - \alpha_+ = \frac{4}{3}a. \tag{5.21}$$

Using the alignment correlation coefficients obtained by the simple analysis, the weak magnetism term was extracted to be

$$a_{\text{pre.}} = 0.206 \pm 0.011\ \%/\text{MeV}. \tag{5.22}$$

The result on the present experiment is shown in Figure 5.6 and listed in Table 5.9, together with other experiments. All the data are consistent with the theoretical prediction

$$a_{\text{theo}} = 0.213\ \%/\text{MeV}, \tag{5.23}$$

which was given by Koshigiri et al. [KO86]. This implies the strong support of the

CVC hypothesis. However, it should be noted that the nucleon mass and the anomalous magnetic moments of the proton and neutron in the free space were used in this calculation. These quantities, as well as the axial-vector coupling constant, are expected to be modified by the in-medium effect, since the decaying nucleons strongly interact with surrounding nucleons. In the weak magnetism term,

$$a = -\frac{1}{2M}\frac{f_V}{f_A}\left(\mu_p - \mu_n + 1 + \frac{\int l}{\int \sigma}\right), \tag{5.24}$$

if we simply replace the nucleon mass, anomalous magnetic moments and the axial-vector coupling constant in the main term with the renormalized values, since the contribution from the orbital angular momentum is small (~4.5 %),

$$a_{\mathrm{eff}} = 0.243\ \%/\mathrm{MeV} \tag{5.25}$$

was obtained. Here,

$$\frac{f_A^*}{f_A^{\mathrm{free}}} - 1 = -5\%, \tag{5.26}$$

$$\frac{(\mu_p - \mu_n + 1)^*}{(\mu_p - \mu_n + 1)^{\mathrm{free}}} - 1 = 7\%, \tag{5.27}$$

$$\frac{M^*}{M^{\mathrm{free}}} - 1 = -(1.5 \sim 3)\%, \tag{5.28}$$

were used in the derivation [WI74][MI90][YA85]. This is 14 % larger than $a_{\mathrm{theo}} = 0.213$

%/MeV. Furthermore, when asymmetry $\Delta y = 0.10 \pm 0.05$ in the axial charge is taken into account, this deviation becomes larger than $a_{\mathrm{pre.}}$. This implies the violation of the CVC hypothesis at 20 % level. Although this derivation is rather simple and may contain a deficiency from the viewpoint of the precise theoretical treatment, the renormalization effect should be at least taken into account in the weak magnetism term. Further theoretical studies are necessary.

Shape factor	a (%/MeV)
Wu et al.	0.16 ± 0.05
Kaina et al.	0.20 ± 0.02
Camp	0.23 ± 0.08
Fukuda et al.	0.19 ± 0.08
M1 transition	0.214 ± 0.001
Alignment correlation	
ETH	0.21 ± 0.04
Osaka79	0.21 ± 0.03
Osaka85	0.207 ± 0.016
Osaka92	0.194 ± 0.016
Present	0.206 ± 0.011
ave.	0.206 ± 0.013

Table 5.9 Summary of the experiments of the weak magnetism term. The results from the spectral shape factor, analog M1 transition and alignment correlation terms are listed.

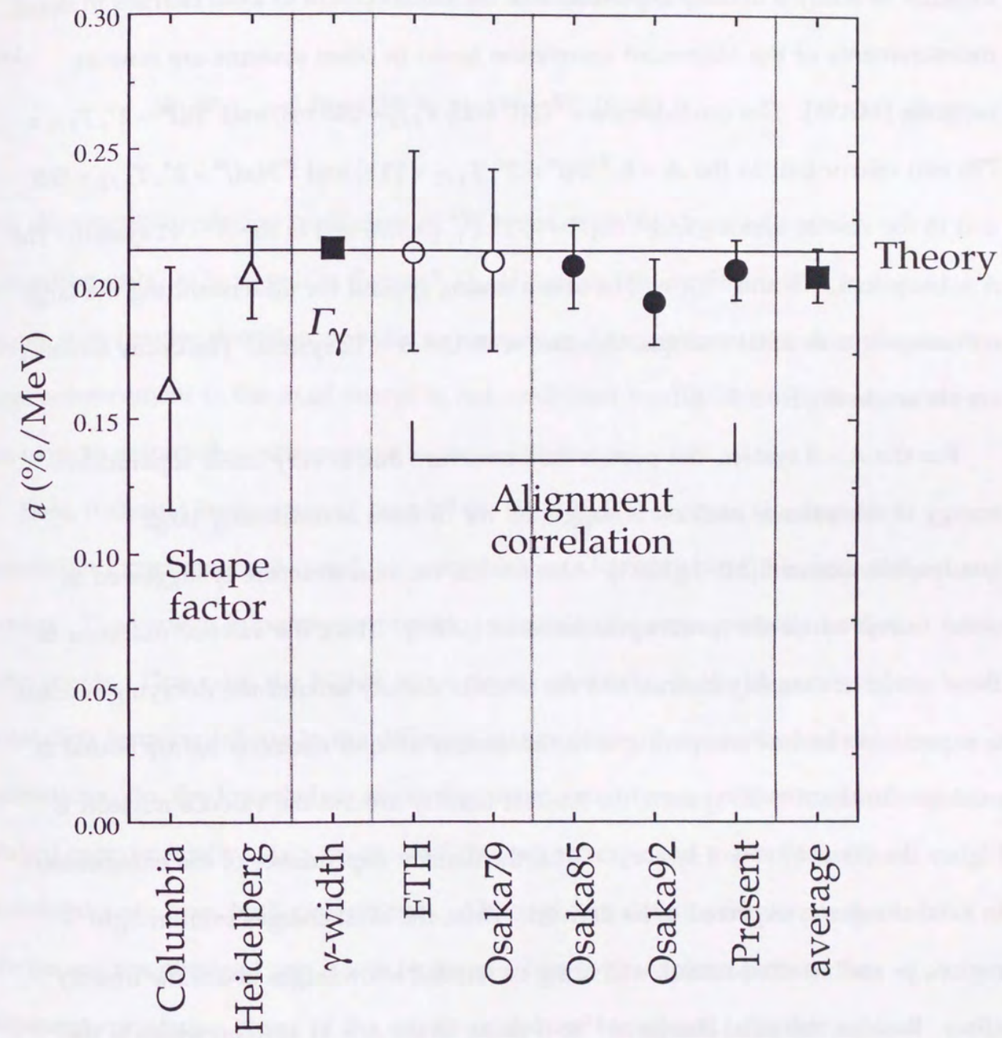

Figure 5.6 Results on the weak magnetism term. The data of the alignment correlation terms of Osaka85 and Osaka92 were reanalyzed, and were averaged together with the present result. Theoretical value was given by Koshigiri et al. [KO86].

5.4 Results on other nuclei

In order to study a density dependence of the enhancement in axial charges in detail, measurements of the alignment correlation terms in other systems are now in progress [MA96]. The candidates are ^{8}Li($I^{\pi} = 2^{+}$, $T_{1/2}$ = 840 ms) and ^{8}B($I^{\pi} = 2^{+}$, $T_{1/2}$ = 770 ms) mirror pair in the A = 8, ^{20}F($I^{\pi} = 2^{+}$, $T_{1/2}$ = 11 s) and ^{20}Na($I^{\pi} = 2^{+}$, $T_{1/2}$ = 560 ms) in the A = 20 system, and ^{41}Sc($I^{\pi} = 7/2^{+}$, $T_{1/2}$ = 596 ms) in the A = 41 system. The A = 13 system, ^{13}B and ^{13}O, will be also a testing ground for understanding the large enhancements in axial charges, together with the A = 12 system. The decay schemes are shown in Figure 5.7 - 5.10.

For the A = 8 system, the proton halo structure due to very small separation energy of the valence nucleon is suggested for ^{8}B from anomalously large quadrupole moment [MI92][KI93]. Also for ^{8}Li, the skin structure is suggested in order to reproduce the quadrupole moment [MI93]. Thus, the valence nucleons in these nuclei are weakly bound, and the nuclear density around the decaying nucleon is expected to be low comparing with the density around nucleons tightly bound in nucleus. In the A = 20 system, the nuclear density around the valence nucleon is higher than that of A = 8 system. Thus, the density dependence of the enhancement in axial charges is expected to be derived. Thus, the axial charges even in light region, p- and sd-shell nuclei, will bring us fruitful knowledges about the density effect. Besides, the axial charge of ^{41}Sc β-decay in the A = 41 system, which is the doubly closed shell +1 nucleon nucleus, will provide us with a clear knowledge about the single nucleon in the nucleus.

The preliminary results for ^{8}Li and ^{20}F are shown in Figure 5.11 and 5.12, respectively. The details of the experiments are described in the appendixes. By the simple analysis, the alignment correlation coefficients were determined to be

$$(B_2/B_0)_{-} = -0.29 \pm 0.04\ \%/\mathrm{MeV} \text{ for } ^{8}\mathrm{Li}\ [\mathrm{MI95}][\mathrm{YA96}], \tag{5.29}$$

and

$$(B_2/B_0)_{-} = -0.40 \pm 0.19\ \%/\mathrm{MeV} \text{ for } ^{20}\mathrm{F}\ [\mathrm{KI96}]. \tag{5.30}$$

The alignment correlation coefficient of ^{8}Li is not explained by the impulse calculation only, as is shown in Figure 5.11. However, the mesonic effect in the axial charge is in reverse direction in order to reproduce the experimental value. So, the large enhancement in the axial charge is not confirmed for ^{8}Li. For ^{20}F, the error is too large to extract the enhancement in the axial charge.

Here, it should be mentioned that for the A =8 and 20 systems, the angular correlation experiments, β-α and β-γ, were performed to search for the second class current. The present experiments provide essentially the same quantity as those experiments. However, the higher order matrix elements in the alignment correlation term contribute in the different manner from those of the angular correlations. So, the knowledges about the higher order terms are expected to be studied experimentally. As a result, axial charges are expected to be obtained unambiguously from both experiments. Although the definite results on the axial charges are not obtained yet, it will be given when the measurements on the alignment correlation terms of the mirror nuclei are completed. Further experimental studies are now in progress.

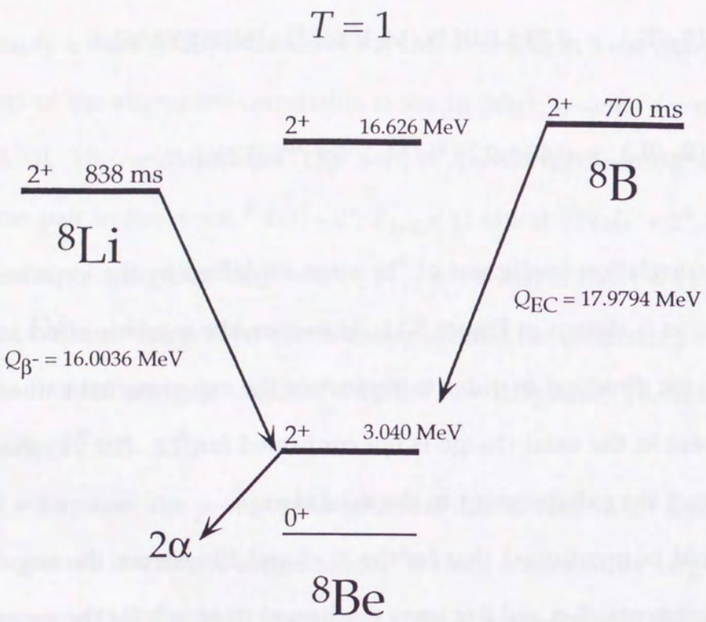

Figure 5.7 Decay scheme of the $A = 8$ system.

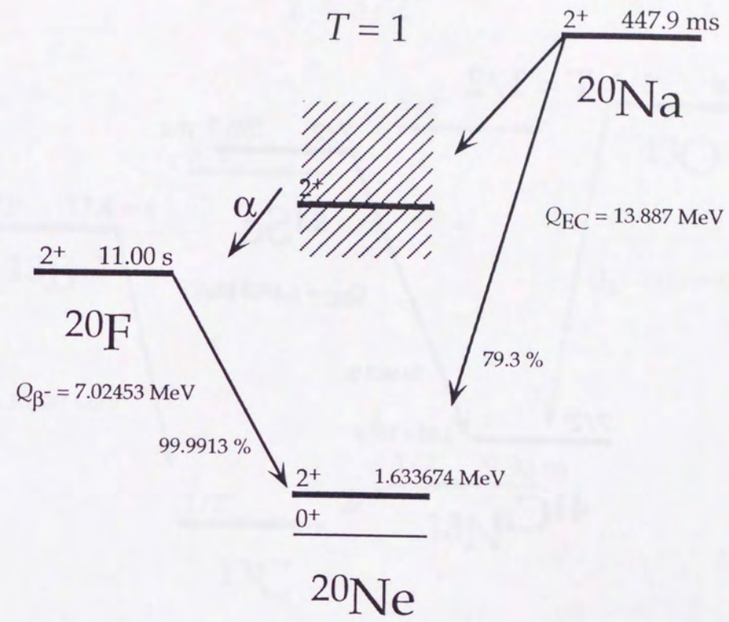

Figure 5.8 Decay scheme of the $A = 20$ system.

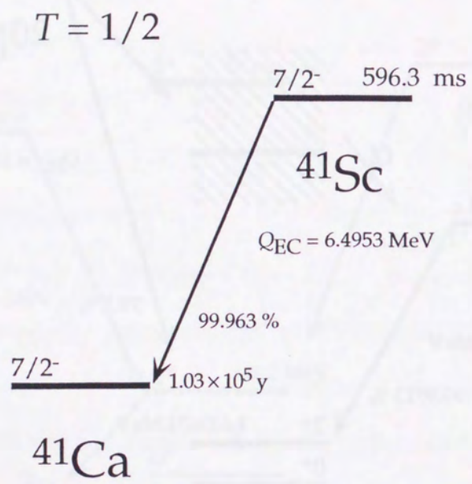

Figure 5.9 Decay scheme of the $A = 41$ system.

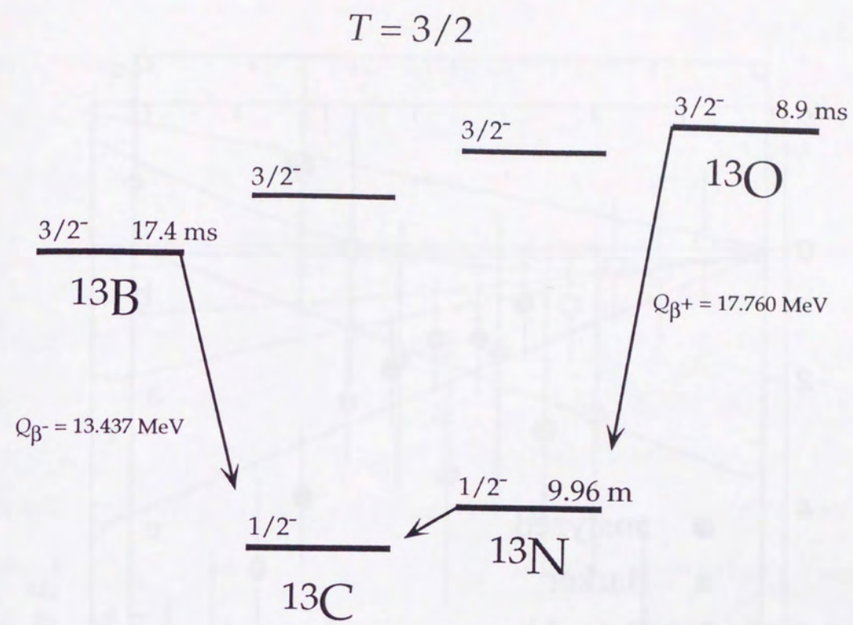

Figure 5.10 Decay scheme of the A =13 system.

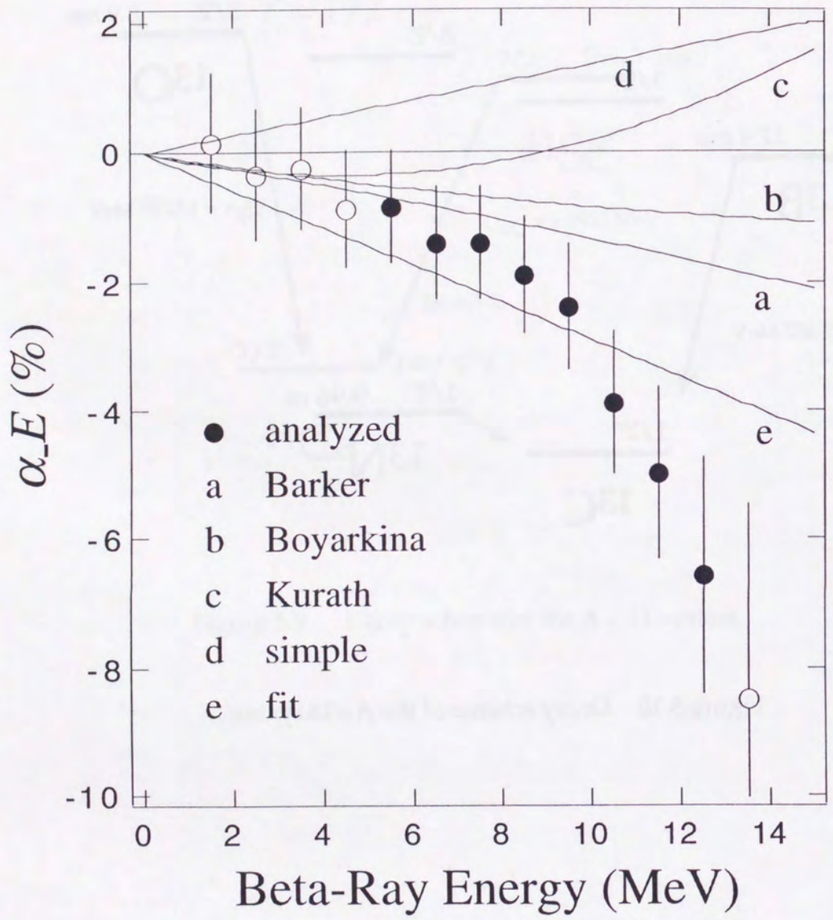

Figure 5.11 Alignment correlation term of ^{8}Li. The fitting line by the simple analysis is shown, where the analyzed data is shown by the closed circles. Several theoretical calculations [TR75][KO94] are also shown. None of them can explain the present result well.

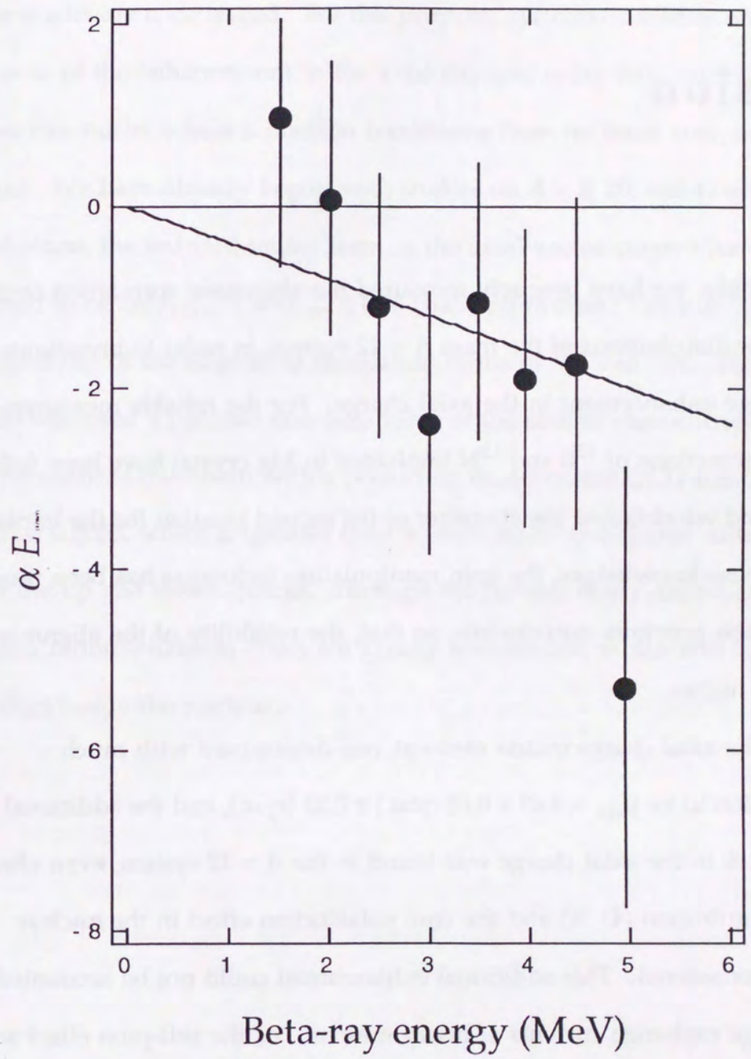

Figure 5.12 Alignment correlation term of ^{20}F. The fitting line by the simple analysis is shown.

Chapter 6

Conclusion

In the present study, we have precisely measured the alignment correlation terms in the β-ray angular distributions of the mass A = 12 system, in order to investigate anomalously large enhancement in the axial charge. For the reliable measurement, the hyperfine interactions of ^{12}B and ^{12}N implanted in Mg crystal have been fully studied again, and we obtained the character of the second location for the implanted nuclei. Using these knowledges, the spin manipulation technique has been much improved from the previous experiments, so that, the reliability of the alignment creation became higher.

As a result, the axial charge matrix element was determined with much improved precision to be $y_{ave.}$ = 4.69 ± 0.05 (stat.) ± 0.22 (syst.), and the additional enhancement 16 % in the axial charge was found in the A = 12 system, even after the the soft-pion contribution (41 %) and the core polarization effect in the nuclear structure were considered. This additional enhancement could not be accounted for by the short-range exchange currents of heavy mesons, i.e., the soft-pion effect and the short-range exchange explained ~40 % again. Therefore, we need to assume that the additional enhancement arise from the in-medium renormalization effect. The nucleon mass renormalization was extracted to be 8 ± 4 % in the A = 12 system. This renormalization factor is fairly consistent with those derived from the analyses of the magnetic moments of mirror nuclei. Thus, the in-medium renormalization effect may have been found in the axial charge. In order to make much clear the

renormalization effect inside the nucleus, more experimental and theoretical studies for other nuclei are encouraged. For this purpose, systematic studies on a density dependence of the enhancement in the axial charges, using halo nuclei, and also using heavier nuclei where a nucleon transforms from its inner core, are also important. We have already begun such studies on A = 8, 20, and 41 systems.

In addition, the induced tensor term in the axial-vector current has been determined to be $2Mf_T/f_A{}^{exp}$ = +0.22 ± 0.05 (stat.) ± 0.18 (syst.^{exp}) ± 0.05 (syst.^{theo}) from the full analysis of the alignment correlation terms of ^{12}B and ^{12}N. The present study has disclosed a possible non-zero value of the second class current for the first time. The result is consistent with a prediction based on the QCD sum rule, $2Mf_T/f_A$ = +0.0152 ± 0.0053, which originates from a small mass- and charge difference between the up and down quarks. Through the present study, investigations on the in-medium renormalization effect are greatly encouraged, which will lead to the quark effect inside the nucleus.

Chapter 7

Appendixes

7.1 Preparation of the target

The production targets used for the experiment were enriched ^{11}B (99 % concentration) and enriched ^{10}B (90 % concentration) for ^{12}B and ^{12}N, respectively. These materials were evaporated on a Mo ribbon (3.2 × 430 × 0.15 mm), using an electron bombarder, as shown in Figure 7.1. Before evaporation, the surfaces of the backing ribbons were cleaned up under the ultrasonic wave in water, methyl alcohol, acetone, and trichloroethylene. This evaporation process took about 10 hours at a vacuum of ~10^{-6} torr. To keep thickness uniform, the target ribbons were rotated during evaporation. Three target ribbons were produced at a time. The thickness of the target was typically 300 μg/cm^2 for ^{11}B and ^{10}B. The thickness was monitored by the change of colors of the target thin layer and it was measured by the increased weight of Al foil. If necessary, this evaporation process was repeated twice to get sufficiently thick target. The heater current was 8 A, and the acceleration voltage was 6 kV.

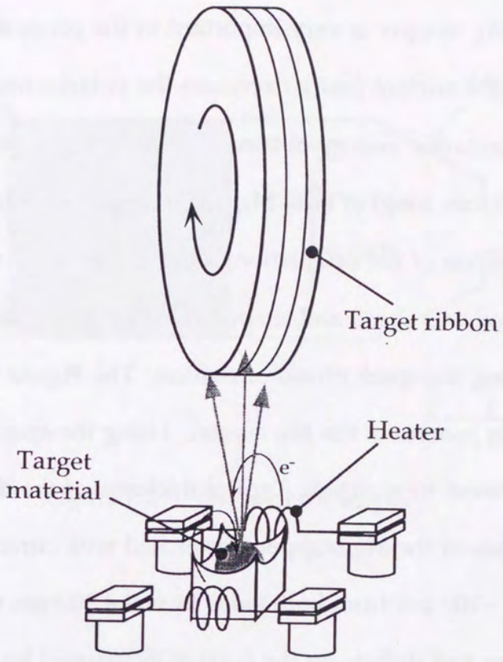

Figure 7.1 Schematic view of target evaporation.

7.2 Preparation of the stopper

The preparation of the Mg stopper is very important in the present experiment. A small contamination on the surface easily decreases the polarization to be observed, because of the low implantation energy obtained in the recoiled nucleus.

A rod (20 m mϕ × 100 mm long) of bulk Mg single crystal was shaped for the stopper. After determination of the orientation of the crystalline c-axis by the X-ray diffraction pattern, the rod was sliced and shaped (12 × 16 mm^2, 500 μm thickness) as shown in Figure 7.2, using the spark erosion machine. The Figure 7.3 shows a schematic view of cutting process of the Mg crystal. Using the spark slicer, the damages on the surface were minimized. Typical thickness of the damage is ~100 μm. After shaping, the surface of the Mg stopper was etched with citric acid (10 % concentration) by about ~100 μm from both sides to make 300-μm thick sample, in order to remove damages and defects on the surface introduced by the machining. The residuals on the surface were blown away by the dry N_2 gas flow. The X-ray diffraction pattern was checked again, in order to confirm the orientation of the c-axis and the structure near the surface, as shown in Figure 7.4. The Mg stopper was mounted on an Al backing plate by Ag paste, which was cooled by the water flow to prevent heat up the sample by the irradiation from the target and the eddy current from rf fields.

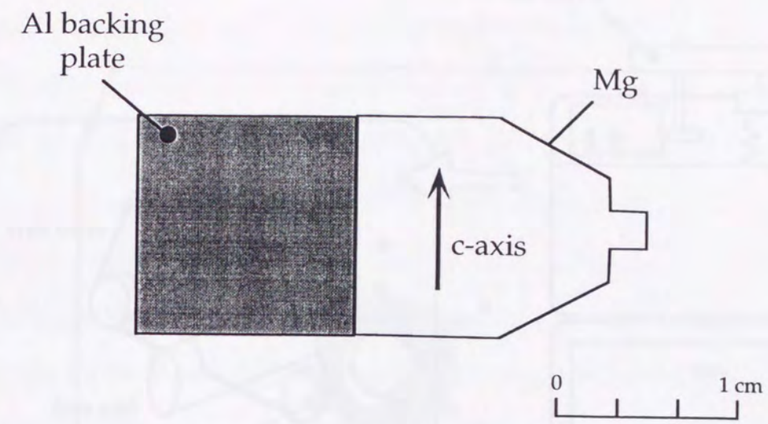

Figure 7.2 Shape of the stopper.

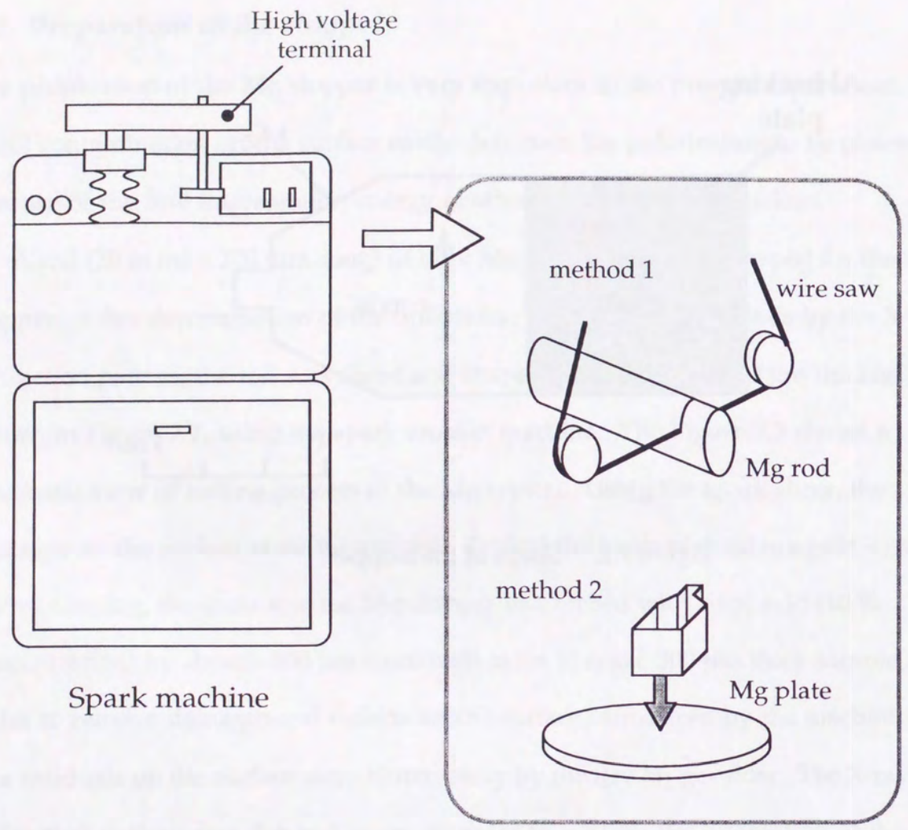

Figure 7.3 Schematic view of cutting Mg crystal by the spark slicer.

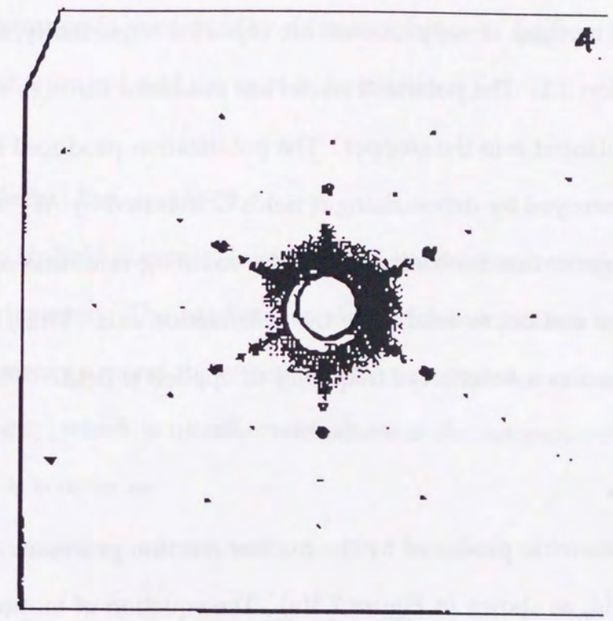

c // X-ray

Figure 7.4 X-ray diffraction pattern of Mg crystal.

7.3 β-NMR method

The conventional β-NMR method is briefly mentioned for comparison of the present experimental method. Four processes are repeated sequentially, as is described in the section 3.1. The polarized nuclei are produced through the nuclear reaction, and are implanted into the stopper. The polarization produced by the nuclear reaction is destroyed by depolarizing rf fields or inverted by AFP rf fields. The change of the polarization is observed from the counting-rate ratio of the counters placed above and below relative to the polarization axis. Thus, NMR resonances are obtained as a function of frequency of applied rf field.

7.3.1 Depolarization

The polarized spin ensemble produced by the nuclear reaction processes around the external magnetic field, as shown in Figure 7.5(a). The equation of motion for this precession is written as

$$\frac{d\vec{\mu}}{dt} = \gamma\vec{\mu} \times \vec{H}_0, \tag{7.1}$$

where μ is the magnetic moment and γ is the gyromagnetic ratio. When a H_1 field is applied perpendicular to the direction of the external field H_0, the spin ensemble processes around the effective field H_{eff} in the rotating frame of the H_1 field, as shown in Figure 7.5(b). If the frequency ω of the H_1 field satisfies the condition,

$$\omega = \gamma H_0, \tag{7.2}$$

then the spin ensemble processes around the H_1 field. Thus, the initial polarization

parallel to the H_0 field is destroyed by the resonant H_1 field, as shown in Figure 7.5(c). In the experiment, the frequency of the H_1 field is modulated several times around the resonance frequency. The difference between magnetic substate populations are averaged and the spin is depolarized.

7.3.2 Adiabatic Fast Passage (AFP)

When a strong H_1 field is swept slowly around the resonance frequency, the polarization is inverted. The adiabatic condition for this process is that the precession frequency around the effective field must be large enough, compared with the sweep velocity, which is usually most severe at the resonance frequency. This AFP condition is written as

$$(\gamma H_1)^2 >> \frac{d\omega}{dt}. \tag{7.3}$$

In order to invert the polarization effectively, the amplitude of the applied H_1 field is modulated, as shown in Figure 7.6. Thus, the initial polarization parallel to the external field H_0 follows the change of the direction of the effective field and finally becomes anti-parallel to the external field by above mentioned handling. In crystals, the implanted nucleus has the magnetic interaction with the surrounding host nuclei, and the spin is dynamically fluctuated by the magnetic field caused by the nuclear dipole-dipole interaction. So, for AFP, the applied field must be strong enough compared with this disturbing field,

$$\gamma H_1 >> 2\pi D, \tag{7.4}$$

where D is corresponding to the dipolar broadening. In the present experiment, however, D is negligibly small and the line width of the resonances is mainly determined by the distribution of the electric field gradient Δq which is a static component. To invert the polarization completely, the frequency modulation of the applied field H_1 must be much larger than resonance width.

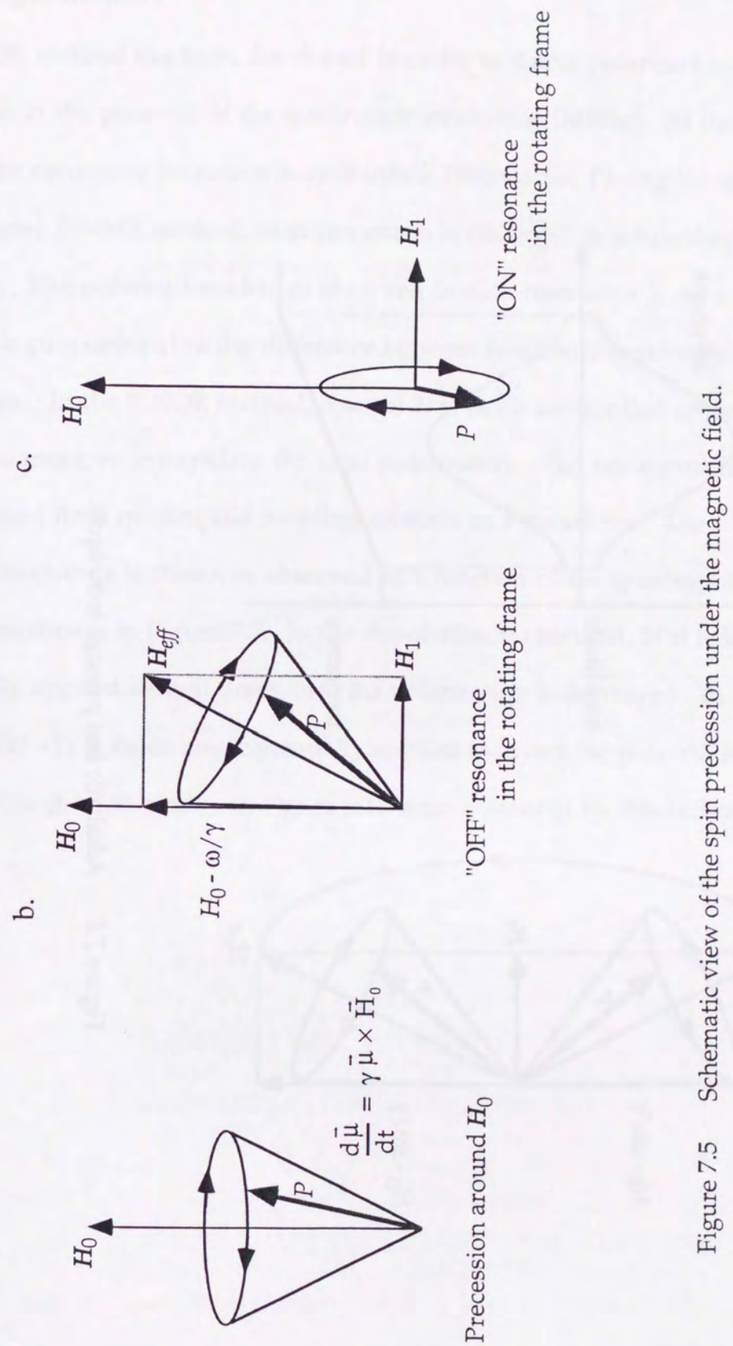

Figure 7.5 Schematic view of the spin precession under the magnetic field.

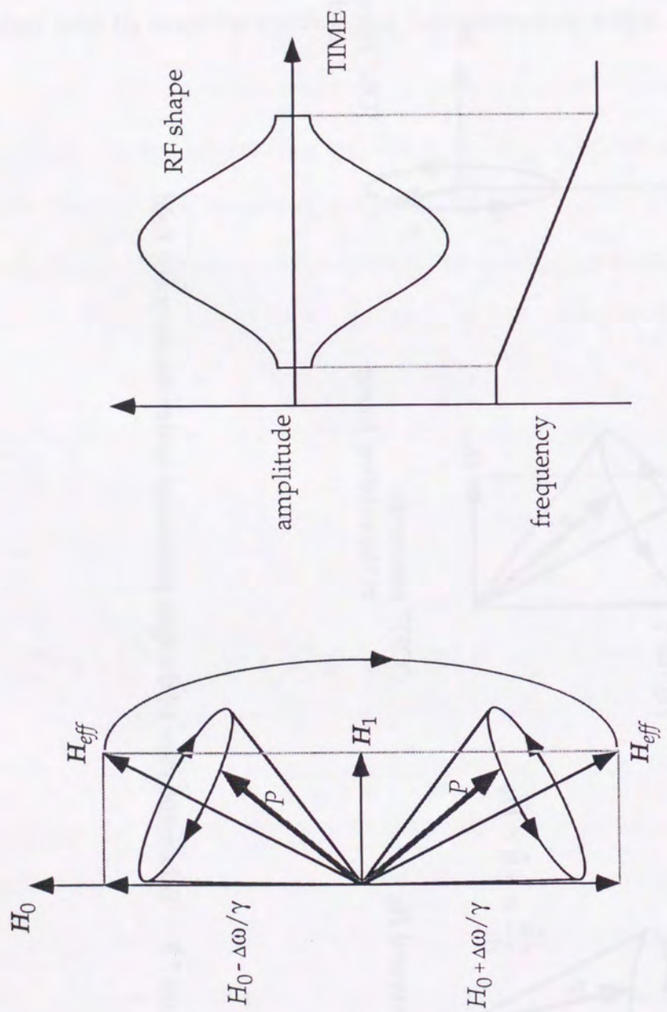

Figure 7.6 Adiabatic fast passage technique.

7.4 β-NQR method

The β-NQR method has been developed in order to detect polarization-change much effectively, in the presence of the quadrupole interaction [MI93c]. As described in Sec. 3.3, the resonance frequency is split into $2I$ frequencies, I being the spin. In the conventional β-NMR method, each resonance is observed as a function of frequency. The polarization-change observed in each resonance is very small, since the effect is proportional to the difference between neighboring substate populations. In the β-NQR method, a set of $2I$ rf fields are applied sequentially on these resonances, to manipulate the total polarization. The resonance frequencies are calculated for a quadrupole coupling constant as a parameter. The polarization-change is therefore observed as a function of the quadrupole coupling constant, as shown in Figure 7.7. In the depolarization method, $2I$ rf fields are sequentially applied several times, and the polarization is destroyed. In the AFP method, $I(2I+1)$ rf fields are sequentially applied to invert the polarization, as shown in Figure 7.8. β-NQR spectra in Figure 3.12 were measured by this technique.

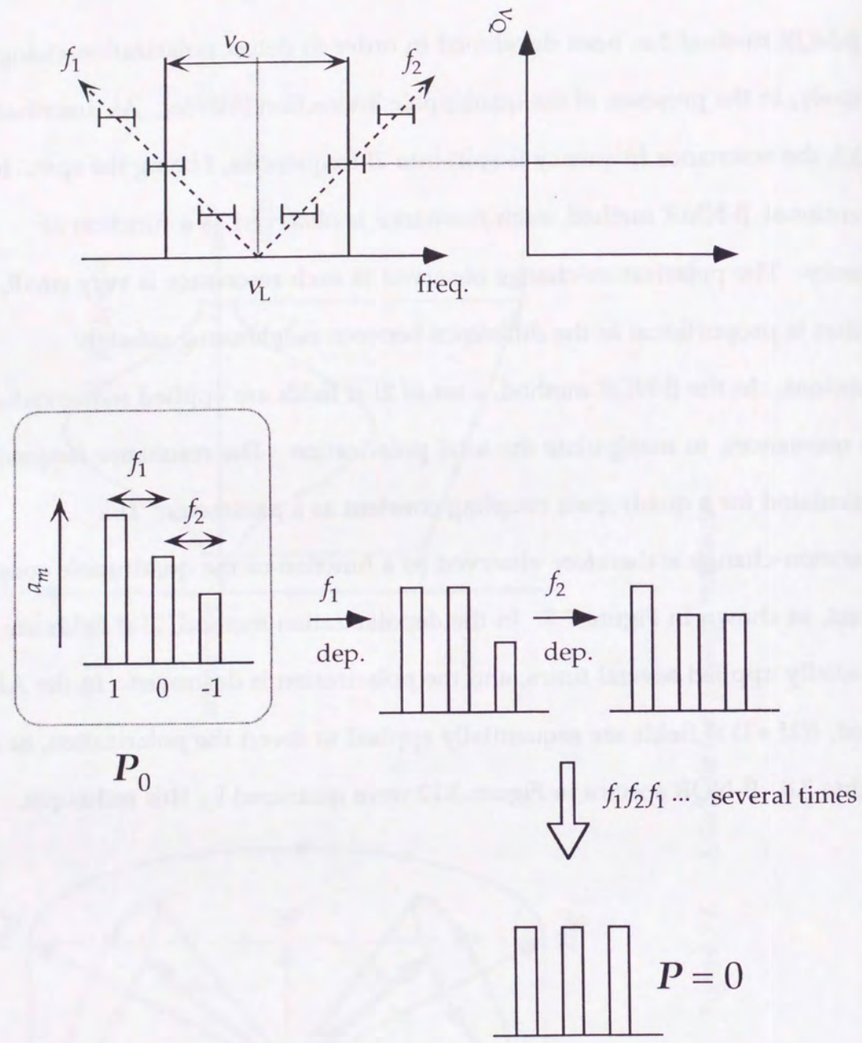

Figure 7.7 β-NQR method (depolarization).
The β-NQR spectrum (upper figure) is observed as a function of the coupling frequency by applying the frequencies f_1 and f_2 several times (lower figure).

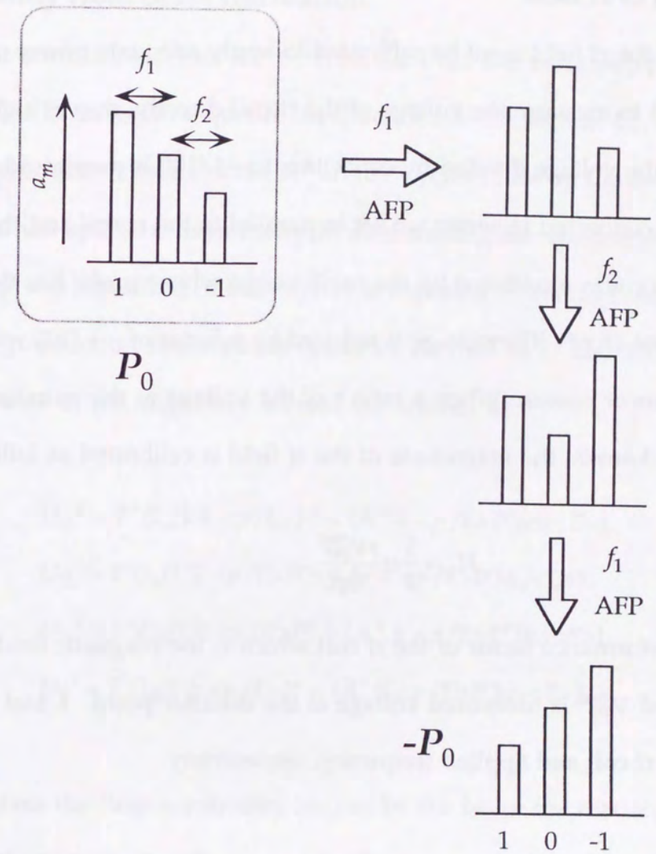

Figure 7.8 β-NQR method (AFP).
The polarization is inverted by applying the frequencies sequentially, f_1 - f_2 - f_1.

7.5 Calibration of rf field

The magnitude of the rf field must be calibrated to apply adequate power of the H_1 field. It is difficult to measure the voltage of the rf coil directly, due to high voltage. For this purpose, the voltage divided by capacitors to ~1/100 is monitored. Ten capacitors of 1 pF connected in series are set in parallel to the rf coil and the voltage at the first capacitor was monitored by the oscilloscope whose probe has the input capacitance of about 13 pF. The voltage is reduced by a factor of ~ 1/100 which is calibrated at the lower power. When a ratio r of the voltage at the monitor point to the direct point is known, the magnitude of the rf field is calibrated as follows

$$H_1 = \frac{1}{4}\alpha\frac{rV_{\mathrm{PP}}^{\mathrm{test}}}{2\pi fL}, \tag{7.5}$$

where α is the performance factor of the rf coil which is the magnetic field strength at one ampere, and $V_{\mathrm{PP}}^{\mathrm{test}}$ is measured voltage at the monitor point. L and f are the inductance of the rf coil and applied frequency, respectively.

7.6 Uncertainty from beam fluctuation

The alignment correlation terms are determined from the asymmetry between the A^+ and A^- cycles in the main sequence, as described in the section 4.3, so that the difference of production between the A^+ and A^- cycles cause by the beam fluctuation could give a small spurious asymmetry in determining the alignment correlation terms, although the repetition of both cycles is expected to average out the difference.

When the production rates of both cycles are defined as T^+ and T^-, respectively, the counting rates in the alignment section are written as

$$U_{\mathrm{II}}^{+} = T^{+}G_{\mathrm{u}}\{1 \mp \langle p/E\rangle \boldsymbol{P}^{+} + (\boldsymbol{A}^{+} \mp \langle p/E\rangle \boldsymbol{P}^{+})\alpha_{\mp}\langle E\rangle\}, \tag{7.6}$$

$$U_{\mathrm{II}}^{-} = T^{-}G_{\mathrm{u}}\{1 \mp \langle p/E\rangle \boldsymbol{P}^{-} + (\boldsymbol{A}^{-} \mp \langle p/E\rangle \boldsymbol{P}^{-})\alpha_{\mp}\langle E\rangle\}, \tag{7.7}$$

$$D_{\mathrm{II}}^{+} = T^{+}G_{\mathrm{d}}\{1 \pm \langle p/E\rangle \boldsymbol{P}^{+} + (\boldsymbol{A}^{+} \pm \langle p/E\rangle \boldsymbol{P}^{+})\alpha_{\mp}\langle E\rangle\}, \tag{7.8}$$

$$D_{\mathrm{II}}^{-} = T^{-}G_{\mathrm{d}}\{1 \pm \langle p/E\rangle \boldsymbol{P}^{-} + (\boldsymbol{A}^{-} \pm \langle p/E\rangle \boldsymbol{P}^{-})\alpha_{\mp}\langle E\rangle\}, \tag{7.9}$$

where T^+/T^- gives the time asymmetry caused by the beam fluctuation, and $G_{\mathrm{u}}/G_{\mathrm{d}}$ is the geometrical asymmetry. $\langle E\rangle$ represents the average value of energy. From above equations, the time asymmetry is extracted to be

$$R_{\mathrm{II}}^{2} \equiv \frac{U_{\mathrm{II}}^{+}}{U_{\mathrm{II}}^{-}}\frac{D_{\mathrm{II}}^{+}}{D_{\mathrm{II}}^{-}} = \left(\frac{T^{+}}{T^{-}}\right)^{2}(1 + 2\Delta A\alpha_{\mp}\langle E\rangle), \tag{7.10}$$

where the first order quantity from the residual polarization $\boldsymbol{P}^{\pm}$ are canceled, and the second order $O(\boldsymbol{P}^2)$ can be neglected. Similarly, the counting rates in the polarization section are written as

$$U_I^+ = T^+G_u\{1 \mp P_I^+ + A_I^+\alpha_\mp <E>\}, \tag{7.11}$$

$$U_I^- = T^-G_u\{1 \mp P_I^- + A_I^-\alpha_\mp <E>\}, \tag{7.12}$$

$$D_I^+ = T^+G_d\{1 \pm P_I^+ + A_I^+\alpha_\mp <E>\}, \tag{7.13}$$

$$D_I^- = T^-G_d\{1 \pm P_I^- + A_I^-\alpha_\mp <E>\}, \tag{7.14}$$

where the definition $P_I^\pm = <p/E>P^\pm(1 + \alpha_\mp <E>)$ was used, and $A_I^\pm$ are the alignments in the polarization section, which are about a half of $A^\pm$ in the alignment section with opposite signs, as shown in Figure 7.9. From the eq. (7.11) - (7.14), the time asymmetry is extracted as follows

$$R_I^2 \equiv \frac{U_I^+}{U_I^-}\frac{D_I^+}{D_I^-}\Bigg/\frac{1-P_I^{+2}}{1-P_I^{-2}} = \left(\frac{T^+}{T^-}\right)^2\left\{1-2\left(\frac{A_I^-}{1-P_I^{-2}}-\frac{A_I^+}{1-P_I^{+2}}\right)\alpha_\mp <E>\right\}, \tag{7.15}$$

where

$$\frac{A_I^-}{1-P_I^{-2}}-\frac{A_I^+}{1-P_I^{+2}} \approx A_I^- - A_I^+ \approx P_I^- + P_I^+. \tag{7.16}$$

Here, the ratio k is introduced as

$$k \equiv 2\frac{P_I^- + P_I^+}{\Delta A} \approx 1. \tag{7.17}$$

Thus, the eq. (7.15) is written as

$$R_I^2 = \left(\frac{T^+}{T^-}\right)^2 (1 - k\Delta A\alpha_\mp <E>). \tag{7.18}$$

Using the eq. (7.10) and (7.18), the time asymmetry is finally written as

$$\frac{T^+}{T^-} = (R_I^2 \times R_{II}^k)^{\frac{1}{2+k}}. \tag{7.19}$$

Similarly, the time asymmetry is derived from counting section II and III, as follows

$$\frac{T^+}{T^-} = (R_{III}^2 \times R_{II}^{k'})^{\frac{1}{2+k'}}, \tag{7.20}$$

with

$$R_{III}^2 \equiv \frac{U_{III}^+}{U_{III}^-}\frac{D_{III}^+}{D_{III}^-}\Bigg/\frac{1-P_{III}^{+2}}{1-P_{III}^{-2}}, \tag{7.21}$$

$$k' \equiv 2\frac{P_{III}^- + P_{III}^+}{\Delta A}. \tag{7.22}$$

In the present experiment, the time asymmetries were calculated to be 0.021 ± 0.006 % and -0.063 ± 0.040 % for ^{12}B and ^{12}N, respectively. Therefore, the correction to the alignment terms are -0.103 ± 0.031 % and 0.121 ± 0.076 % for ^{12}B and ^{12}N, respectively, dividing the time asymmetries by the degree of alignments. These corrections should be included in the analysis of the alignment correlation terms. In the present analysis, however, this effect was included in the systematic error without correction. The effect of the T^+/T^- was evaluated from the change of the

alignment correlation coefficients determined by the linear fitting, when the time asymmetries are introduced.

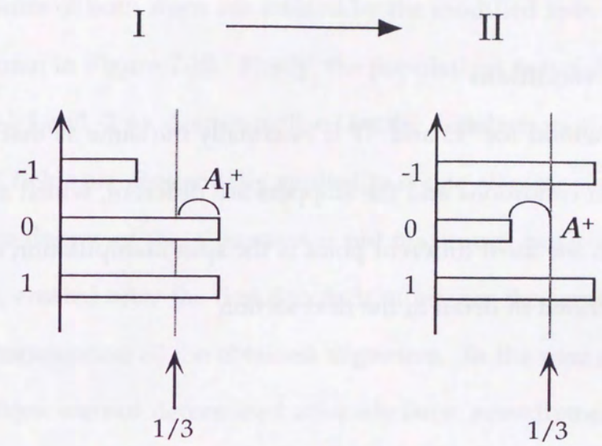

Figure 7.9 Alignments in the polarization and alignment section.

7.7 Experimental details of ^{8}Li and ^{20}F

7.7.1 Experimental conditions

The experimental method for ^{8}Li and ^{20}F is essentially the same as that for ^{12}B and ^{12}N. The production conditions and the stoppers are different, which are listed in Table 7.1. However, the most different point is the spin manipulation of the spin I = 2 cases. This is described in detail in the next section.

	^{8}Li	^{20}F
I^{π}	2^{+}	2^{+}
$T_{1/2}$	838 ms	11.00 s
E_{β} (max.)	12.964 MeV	5.39086 MeV
Reaction	^{7}Li(d, p)^{8}Li	^{19}F(d, p)^{20}F
Beam energy	3.5 MeV	3.5 MeV
Beam intensity (typ.)	5 μA	10 μA
Recoil angle	10° ~ 40°	25° ~ 40°
Recoil energy (typ.)	1.7 MeV	1 MeV
β-ray yield (typ.)	1.5×10^{3} cps	8×10^{3} cps
Stopper	Zn	MgF_2
Magnetic field	600 Oe	2300 Oe
eqQ/h	~ 33.5 kHz	~ -5.77 MHz

Table 7.1 Experimental conditions for ^{8}Li and ^{20}F.

7.7.2 Spin manipulation for I = 2 nuclei

The spin alignments of both signs are created by the modified spin manipulation technique, as shown in Figure 7.10. Firstly, the populations between magnetic substates m = 1 ↔ 2 and -2 ↔ -1 are equalized by the depolarization technique. In the next step, four rf fields are sequentially applied to create alignments. With this manipulation, the degree of the alignment is not maximum, but populations in both alignment cycles, created after the first depolarizations, are the same which has the advantage in determination of the obtained alignment. In the case of I = 2, the substate populations are not determined uniquely from measurement of up and down asymmetry even after the equalization of 2 sets of substate populations. In this manipulation, the difference between positive and negative alignment can be calculated as

$$\Delta A = -\frac{18(3\eta-2)}{10\eta-1}P_{\mathrm{I}} - \frac{3(5-6\eta)}{10\eta-1}(P_{\mathrm{II}}^{+}+P_{\mathrm{II}}^{-}), \tag{7.23}$$

where η is the average degree of achievement of the AFP rf fields. P_{I} is the polarization in the counting section I, and $P_{\mathrm{II}}^{\pm}$ are the residual polarizations in the alignment section. Similarly, the alignment is calculated from the polarizations in the counting section II and III, as

$$\Delta A = \frac{-54\eta+36}{44\eta-35}P_{\mathrm{III}} + \frac{3}{44\eta-35}(P_{\mathrm{II}}^{+}+P_{\mathrm{II}}^{-}). \tag{7.24}$$

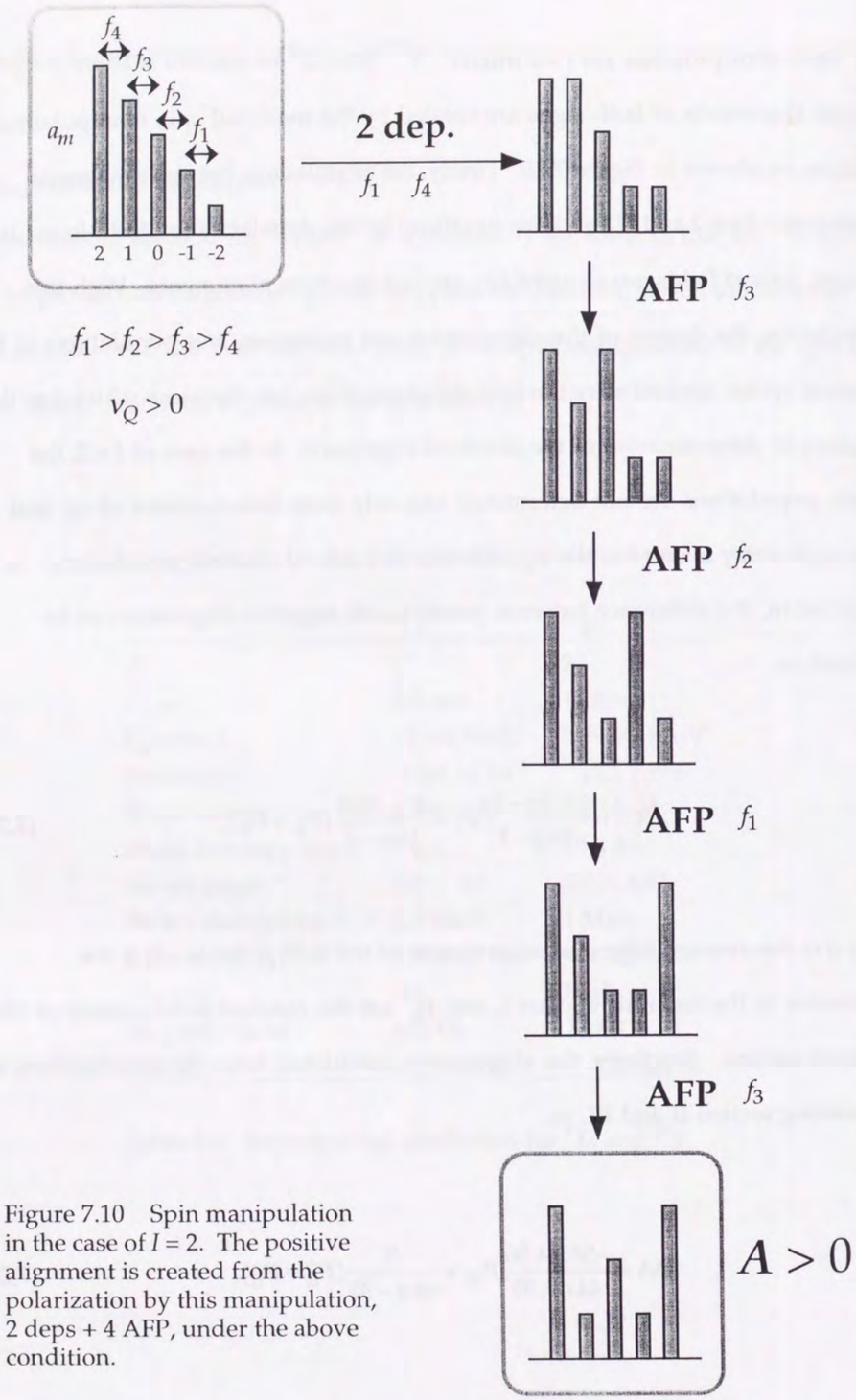

Figure 7.10 Spin manipulation in the case of $I = 2$. The positive alignment is created from the polarization by this manipulation, 2 deps + 4 AFP, under the above condition.

References

[AD83] E.G. Adelberger et al., Phys Rev. C27 (1983) 2833.

[AR94] M. Arneodo, Phys. Rep. 240 (1994) 301.

[BA81] G. Bardin et al., Phys. Lett. B104 (1981) 320.

[BR78a] H. Brandle et al., Phys. Rev. Lett. 40 (1978) 306.

[BR78b] H. Brandle et al., Phys. Rev. Lett., 41 (1978) 299.

[BR95] L. De Braeckeleer et al., Phys. Rev. C51 (1995) 2778.

[CA75] F.P. Calaprice et al., Phys. Rev. Lett. 35 (1975) 1566.

[CA90] J.B. Camp, Phys. Rev. C41 (1990) 1719.

[CH71] M. Chemtob and M. Rho, Nucl. Phys. A163 (1971) 1.

[CH73] B.T. Chertok et al., Phys. Rev. C8 (1973) 23.

[DE83] U. Deutschmann et al., Nucl. Phys. A411 (1983) 337.

[DU78] N. Dupuis-Rolin et al., Phys. Lett. 79B (1978) 359.

[EN68] P.M. Endt, Nucl. phys. 114 (1968) 48 and 69.

[FE58] R.P. Feynman and M. Gell-Mann, Phys. Rev. 109 (1958) 193.

[FU95] M. Fukuda et al., Proc. 4th Int. Symp. on Weak and Electromagnetic Interactions in Nuclei, Osaka, 1995, 369.

[FU96] M. Fukuda et al., Proc. of Int. Symp. on Non Nucleonic Degrees of Freedom Detected in Nucleus, Osaka, 1996, World Scientific, p136.

[GA83] C.A. Gagliardi et al., Phys. Rev. C28 (1983) 2423.

[GE57] S.S. Gershtein and J.B. Zeldovich, JETP (Sov. Phys.) 2 (1957) 576.

[HA85] L.A. Hamel et al., Z. Phys. A321 (1985) 439.

[HO73] J. Hockert et al., Nucl. Phys. A217 (1973) 14.

[KA77] W. Kaina et al., Phys. Lett. 70B (1977) 411.

[KI90] A. Kitagawa et al., Hyp. Int. 60 (1990) 869.

[KI92] M. Kirchbach, D.O. Riska, and K. Tsushima, Nucl. Phys. A542 (1992) 616.

[KI92] A. Kitagawa, Doctor Thesis, Osaka University.

[KI93] H. Kitagawa and H. Sagawa, Phys. Lett. B299 (1993) 1.

[KI96] K. Minamisono et al., Proc. of Int. Symp. on Non Nucleonic Degrees of Freedom Detected in Nucleus, Osaka, 1996, World Scientific, p381.

[KO81] K. Koshigiri, H. Ohtsubo, and M. Morita, Prog. Theor. Phys. 66 (1981) 358.

[KO86] K. Koshigiri et al., J. Phys. Soc. Japan, 55 Suppl. (1986) 1014.

[KO89] K. Koshigiri, K. Kubodera, H. Ohtsubo, and M. Morita, Proc. Int. Conf. on Nuclear Weak Process and Nuclear Structure, Osaka, World Scientific (1989) 52.

[KO94] private communication with K. Koshigiri.

[KO95a] K. Koshigiri, R. Morita and M. Morita, Proc. 4th Int. Symp. on Weak and Electromagnetic Interactions in Nuclei, Osaka, World Scientific (1995) 361.

[KO95b] K. Koshigiri, R. Morita and M. Morita, Nucl. Phys. A588 (1995) 165.

[KO97] private communication with K. Koshigiri and M. Morita.

[KU73] K. Kubodera, J. Delorme and M. Rho, Nucl. Phys. B66 (1973) 253.

[KU78] K. Kubodera, J. Delorme and M. Rho, Phys. Rev. Lett. 40 (1978) 755.

[KU91] K. Kubodera and M. Rho, Phys. Rev. Lett. 67 (1991) 3479.

[LE78] Lebrun et al., Phys. Rev. Lett. 40 (1978) 302.

[MA79] Y. Masuda, T. Minamisono, Y. Nojiri, and K. Sugimoto, Phys. Rev. Letters 43 (1979) 1083.

[MA85] K. Matauta, Doctor Thesis, Osaka University.

[MA90] H.Mach et al., Phys. Rev. C41 (1990) 226.

[MA96] K. Matsuta at al., Proc. of Int. Symp. on Non Nucleonic Degrees of Freedom Detected in Nucleus, Osaka, 1996, World Scientific, p215.

[MC80] R.D. McKeown, G.T. Garvey, and C.A. Gagliardi, Phys. Rev. C22 (1980) 738.

[MI83] T. Minamisono et al., Phys. Lett. 130B (1983) 1.

[MI86] T. Minamisono, K. Matsuta, Y. Nojiri, and K. Takeyama, J. Phys. Soc. Japan 55 (1986) Suppl. 382.

[MI90] T. Minamisono et al., Nucl. Phys. A516 (1990) 365.

[MI92] T. Minamisono et al., Phys. Rev. Lett. 69 (1992) 2058.

[MI93a] T. Minamisono, A. Kitagawa, K. Matsuta and Y. Nojiri, Hyp. Int. 78 (1993) 77.

[MI93b] T. Minamisono et al., Nucl. Phys. A559 (1993) 239.

[MI93c] T. Minamisono et al., Hyp. Int. 80 (1993) 1315.

[MI93] T.Minamisono et al., Hyp. Int. 78 (1993) 159.

[MI95] T. Minamisono et al., Proc. 4th Int. Symp. on Weak and Electromagnetic Interactions in Nuclei, Osaka, 1995, 365.

[MI96] T. Minamisono et al., Proc. of Int. Symp. on Non Nucleonic Degrees of Freedom Detected in Nucleus, Osaka, 1996, World Scientific, p190.

[MI96a] M. Mihara et al., Proc. of Int. Symp. on Non Nucleonic Degrees of Freedom Detected in Nucleus, Osaka, 1996, World Scientific, p224.

[MI98a] T. Minamisono, T. Ohtsubo, S. Takada, S. Fukuda, T. Izumikawa, M. Tanigaki, T. Miyake, T. Yamaguchi, N. Nakamura, H. Tanji, K. Matsuta, M. Fukuda, and Y. Nojiri, Phys. Lett., in print.

[MI98b] T. Minamisono, K. Matsuta, T. Yamaguchi, K. Minamisono, T. Ikeda, Y. Muramoto, M. Fukuda, Y. Nojiri, A. Kitagawa, K. Koshigiri, and M. Morita, to appear in Phys. Rev. Lett.

[MO76] M. Morita et al., Prog. Theor. Phys. Suppl. 60 (1976) 1.

[MO78] M. Morita et al., Phys. Lett. 73B (1978) 17.

[OH93] T. Ohtsubo et al., Hyp. Int 78 (1993) 185.

[OH93] T. Ohtsubo et al., Hyp. Int. 80 (1993) 1051.

[PA75] L. Palffy et al., Phys. Rev. Lett. 34 (1975) 212.

[PA96] Particle Data Group, Phys. Rev. D54 (1996) 1.

[RH81] M. Rho and G.E. Brown, Comments Parts. Nucl. Phys. 10 (1981) 201.

[RI72] D.O. Riska and G.E. Brown, Phys. Lett. 38B (1972) 193.

[RO88] R.D. Rosa et al., Phys. Rev. C37 (1988) 2722.

[SA79] H. Sagawa, T. Suzuki, H. Hyuga and A. Arima, Nucl. Phys. A322 (1979) 361.

[SH96] H. Shiomi, Nucl. Phys. A603 (1996) 281.

[SU75] K. Sugimoto, I. Tanihata, and J. Goring, Phys. Rev. Lett. 34 (1975) 1533.

[SU78] K. Sugimoto, T. Minamisono, Y. Nojiri, and Y. Masuda, Proc. Int. Conf. on Nuclear Structure (Tokyo, 1977); J. Phys. Soc. Japan 44 (1978) Suppl. 801.

[TA77] I. Tanihata et al., Phys. Lett. 67B (1977) 392.

[TO92] I.S. Towner, Nucl. Phys. A542 (1992) 631.

[TO95] I.S. Towner et al., Proc. of Int. Conf. on Exotic Nuclei and Atomic Masses, Arles, France, 1995.

[TR75] R.E. Tribble and G.T. Garvey, Phys. Rev. C12 (1975) 967.

[TR78] R.E. Tribble and D.P. May, Phys. Rev. C18 (1978) 2704.

[WA82] E.K.Warburton et al., Phys. Rev. C26 (1982) 1186.

[WA88] E.K. Warburton et al., Ann. Phys. 187 (1988) 471.

[WA91] E.K. Warburton, Phys. Rev. Lett. 66 (1991) 1823.

[WA92] E. K. Warburton and I.S. Towner, Phys. Lett. B294 (1992) 1.

[WA94a] E.K. Warburton, I.S. Towner, and B.A. Brown, Phys. Rev. C49 (1994) 824.

[WA94b] E.K. Warburton and I.S. Towner, Phys. Rep. 243 (1994) 103.

[WE58] S. Weinberg, Phys. Rev. 112 (1958) 1375.

[WI70] D.H. Wilkinson, Phys. Lett. 31B (1970) 447.

[WI74] D.H. Wilkinson, Nucl. Phys. A225 (1974) 365.

[WU77] C.S. Wu et al., Phys. Rev. Lett. 39 (1977) 72.

[YA85] T. Yamazaki, Phys. Lett. 160B (1985) 227.

[YA96] T. Yamaguchi et al., Proc. 10th Int. Conf. on Hyperfine Interactions, Leuven, 1996, 336.

[YA96] T. Yamaguchi et al., Proc. of Int. Symp. on Non Nucleonic Degrees of Freedom Detected in Nucleus, Osaka, 1996, World Scientific, p385.